A STUDY OF CHARM BARYONS CONTAINING A LAMBDA BARYON IN THE FINAL STATE

A Dissertation

Submitted to the Graduate School
of the University of Notre Dame
in Partial Fulfillment of the Requirements
for the Degree of

Doctor of Philosophy

by

Joseph Alexander Swiatek

Neal M. Cason, Director

Department of Physics
Notre Dame, Indiana
April, 1995

A STUDY OF CHARM BARYONS

CONTAINING A LAMBDA BARYON IN THE FINAL STATE

Abstract

by

Joseph Alexander Swiatek

A study of the charm baryons Λ_c^+ and Ξ_c^+ decaying into the respective final states $\Lambda^0\pi^+\pi^-\pi^+$ and $\Lambda^0 K^-\pi^+\pi^+$ is described, and measurements of the relative branching ratios $B(\Lambda_c^+ \to \Lambda^0\pi^+\pi^-\pi^+)/B(\Lambda_c^+ \to pK^-\pi^+)$ and $B(\Lambda_c^+ \to p\overline{K^{*0}}(892))/B(\Lambda_c^+ \to pK^-\pi^+)$ are presented. The data samples were obtained in high-energy photoproduction experiment E-687 at the Fermilab Wide Band Laboratory during the 1990-91 fixed target running period with a mean tagged photon energy of $\approx$ 200 GeV. The $B(\Lambda_c^+ \to \Lambda^0\pi^+\pi^-\pi^+)/B(\Lambda_c^+ \to pK^-\pi^+)$ measurement was based on samples of 123 ± 20 observed $\Lambda_c^+ \to \Lambda^0\pi^+\pi^-\pi^+$ decays and 522 ± 38 observed $\Lambda_c^+ \to pK^-\pi^+$ decays. The relative branching ratio $B(\Lambda_c^+ \to \Lambda^0\pi^+\pi^-\pi^+)/B(\Lambda_c^+ \to pK^-\pi^+)$ is measured to be $1.16 \pm 0.27\ ^{+0.16}_{-0.18}$ where the first error is statistical error and the second group of errors is systematic error. The $B(\Lambda_c^+ \to p\overline{K^{*0}}(892))/B(\Lambda_c^+ \to pK^-\pi^+)$ measurement was based on observed samples of 76 ± 12 $\overline{K^{*0}}(892)$ candidates and 436 ± 31 $pK^-\pi^+$ candidates, and is determined to be $0.39 \pm 0.07 \pm 0.07$.

To my family,

Father Joseph
Mother Mary Ann
Brother Daniel
and
Grandmothers Helen and Mary

TABLE OF CONTENTS

LIST OF FIGURES

LIST OF TABLES

ACKNOWLEDGEMENTS

If someone had told me when I was in grade school that I would someday earn a PhD in High Energy Physics from Notre Dame I would not have believed it. So many people have made this possible. I consider myself lucky to have been a part of such a successful experiment as E-687 as a graduate student; thanks to all the collaborators who made it go.

I first would like to thank my research director Neal Cason for his patience, understanding, analysis expertise, and affability, all of which were indispensable in completing this thesis. Bill Shephard's knowledge and attention to detail served me well both in the physics analysis and in the writing of the manuscript, and for that I thank him. John LoSecco always provided useful insights regarding physics issues, as did Mitch Wayne, who also listened to my various concerns. Thanks also to Jim Bishop for maintaining the computer system, and to Randy Ruchti, for his infectious enthusiasm. Fellow students Danilo Pušeljić, Chris Kennedy, and Wu Zeyuan played major roles in helping me with the learning curve of the experiment, and they have my gratitude, as do fellow travelers Doran Stienike, Syd Taegar, and Tony Lin who provided the camaraderie which helped sustain me in this endeavor.

I would like to thank Joel Butler, Jim Wiss, John Cumalat for their commitment to excellence in all areas of E-687, and for their encouragement regarding my research topic. I was fortunate to have such role models. Fellow baryon men Luca Cinquini and Harry Cheung were instrumental in many phases of my analysis, and I thank them for their help and willingness to communicate their fine ideas. Special thanks

to Rob Gardner, whose truly excellent thesis served as the ideal for my own, and who assisted me a great deal at the end.

Finally, I thank my friends who kept in touch all these years during some most difficult times and who helped me so much in ways they probably don't even realize: Meg, Suzanne, Miguel, Joe, Gaylon, James, Dan, Jeff, Loren, Pilar, Jeff, and Jerry. Thanks also to my family: to my brother Dan, who just by talking and visiting always reminded me of who I was; and to my parents, for all their love and support. Special thanks to Lisa, because if she hadn't been around, I don't know how I would have managed. And to the Irish, for one of the greatest days I have ever witnessed, October 15, 1988: ND 31, Miami 30.

CHAPTER 1

Introduction

1.1 The Quark Model and Charm

The existence of truly fundamental particles known as quarks which were constituents of hadrons was proposed in the early 1960's by Gell-Mann [Gel 64] and Zweig. According to this early quark model the quarks came in three flavors each of fractional charge: *up* and *down* which composed an isospin doublet, and *strange* an isosinglet. The existence of the *up* and *down* flavors was able to account for many hadrons known at that time including the proton, neutron, and other particles such as the π-mesons. The presence of "strange" particles such as K-mesons and Λ^0 baryons was accounted for by the *strange* quark, so named since these hadrons were pair-produced copiously on the time scale of the strong interaction but unexpectedly decayed much more slowly.

One problem with the quark model was that certain quark combinations seemed to violate the Pauli exclusion principle, such as the Δ^{++} baryon resonance which contains three *up* quarks each of spin-1/2. This dilemma was resolved by assigning a new degree of freedom to each quark known as *color* of which there were three types; hadrons were constructed in such a manner that they were colorless and thus Fermi statistics were preserved. Color is interpreted as the "charge" of the strong interaction [Gro 73].

Another problem with the quark model was that free quarks were not observed experimentally; however, what ultimately lent greater credence to this model in the early 1970's had nothing to do with theories or experimental evidence regarding quark confinement but with the discovery of a new particle thought to contain a different quark[1]. Glashow, Iliopoulous, and Maiani in 1970 [Gla 70] had proposed the existence of a fourth quark, *charm*, to explain the experimental absence of flavor-changing neutral currents such as the decay $K^0 \rightarrow \mu^+\mu^-$; it was therefore a great triumph for their theory and for the quark model itself when the J/ψ meson was discovered simultaneouly at SLAC and Brookhaven in 1974, and was interpreted as the ground state of a "hidden"-charm $c\overline{c}$ system. Subsequent experiments revealed the existence of particles containing "open" charm such as the charm baryon Λ_c^+ (udc) and charm mesons D^0 $(c\overline{u})$, D^+ $(c\overline{d})$, and D_s^+ $(c\overline{s})$[2]. In the last 15-20 years a substantial body of evidence regarding *charm* began accumulating and continues to grow today: new particles are being discovered, additional decay modes are being observed, and precise measurements of decay rates and lifetimes of charm particles are being performed which aid in the understanding of their dynamics and structure.

1.2 Weak Decays of Charm Particles

Charm particles decay via the strong, electromagnetic, or weak interactions. Since the charm quantum number is conserved in the strong and electromagnetic processes, such decays can only occur provided that the mass of the charm particle is greater than that of the lowest-energy charm hadrons. Often this is not the case, yet large numbers of charm decays are nevertheless observed. The weak interaction accounts for this abundance and it is the timescale of this interaction (10^{-13} seconds) which

[1] A series of deep-inelastic scattering experiments at SLAC in the 1960's had first suggested evidence of structure (quarks) within protons.

[2] Charge conjugate states are implied throughout this work unless otherwise explicitly noted.

enables these particles to be observed experimentally.

Processes for weak decays of charm hadrons include W-emission (the spectator model), W-exchange, and W-annihilation. Feynman diagrams for each of these interactions are shown in Figure 1.1. The spectator model provides a simple estimate of the charm lifetime because the mechanism involved is similar to that of the weak decay of the muon. The lifetime is estimated as:

$$\tau(c) = \tau(\mu) \times B(c \rightarrow qe\nu) \times (\frac{m_\mu}{m_c})^5 \quad , \tag{1.1}$$

so that this model predicts charm hadron lifetimes on the order of 10^{-12} seconds in accord with experimental measurements. The problem is that it predicts universal lifetimes for the charm baryons and mesons, and experiments have shown that this is not the case. Therefore, effects due to W-exchange, annihilation, and other complicated phenomena must be taken into account to provide more complete representations of the decay schemes. For example, it is straightforward to understand (albeit on a naive level) the lifetime difference between the Λ_c^+ and the Ξ_c^+ if one constructs quark diagrams for each of these decays: the Λ_c^+ can decay via W-exchange while the Ξ_c^+ cannot. The decay rate of the former is therefore enhanced with respect to the latter and its lifetime is reduced.

The charm quark decays weakly to a strange quark by coupling to a W^+ particle. However, experiments have shown that charm quarks can also decay to down quarks but at rates markedly suppressed with respect to the $c \rightarrow s$ decays. The model for these interactions is based on the Cabibbo theory of weak decays [Cab 64] which stipulates that the d and s quarks exist in mixed states d', s', and upon measurement the states collapse yielding the eigenvalues d and s. The mixed states are related to

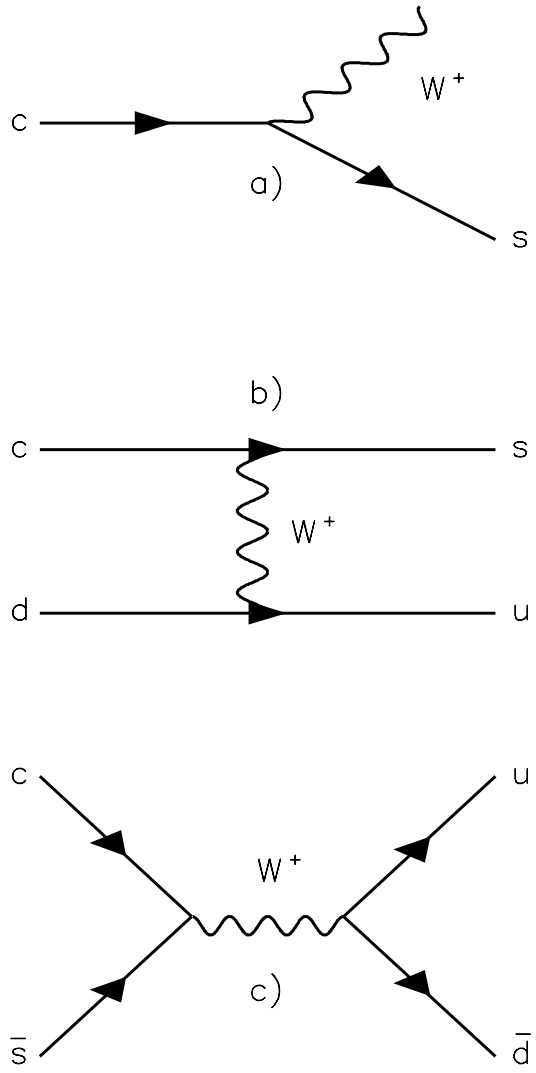

Figure 1.1. Charm decay processes: a) W-emission, b) W-exchange, and c) annihilation.

the mass states according to the following expression:

$$\begin{pmatrix} d' \\ s' \end{pmatrix} = \begin{pmatrix} \cos\theta_c & \sin\theta_c \\ -\sin\theta_c & \cos\theta_c \end{pmatrix} \begin{pmatrix} d \\ s \end{pmatrix} \tag{1.2}$$

In this representation the transition exists as $c \rightarrow s'$ so that the Cabibbo-favored $c \rightarrow s$ decay rate is weighted by the factor $\cos^2\theta_c$ while its Cabibbo-suppressed counterpart $c \rightarrow d$ is weighted by $\sin^2\theta_c$ where $\theta_c \approx 13$ degrees. This model was expanded to include six quarks in 1973 by Kobayashi and Maskawa [Kob 73].

1.3 Charm Baryons and Specific States of Interest: Lambda States

Charm-baryon physics is still a relatively new endeavor when one considers that a significant portion of the spin-1/2 baryons remains undiscovered. The baryon spin-1/2 and spin-3/2 multiplets are depicted in Figure 1.2; only recently has the majority of the first group of spin-1/2 charm baryons been observed experimentally. The Σ_c isospin triplet is sufficiently massive that these baryons decay strongly to $\Lambda_c^+\pi$, while the others decay weakly into varieties of final states. The two charm baryons which this thesis considers are the Λ_c^+ and the Ξ_c^+ . The Cabibbo-favored weak decays of each of these baryons involve flavor changes ΔC=1 and ΔS=-1.

Charm decays are signified by a preponderance of strange ($s = -1$) particles in the final states; for the Λ_c^+ these exist primarily as lambdas or kaons. The question is which types of decays are more frequent: those involving strangeness associated with the baryon or with the K-meson? One might conjecture that the former should be preferred (udc becomes uds), but the only way to investigate this hypothesis would be to calculate the *total* decay rates $\Lambda_c^+ \rightarrow \Lambda^0 X$ and $\Lambda_c \rightarrow pKX$. To do this, one must measure as many *relative decay rates* as possible and sum them; it is in this sense that the relative branching ratio $B(\Lambda_c^+ \rightarrow \Lambda^0\pi^+\pi^-\pi^+)/B(\Lambda_c^+ \rightarrow pK^-\pi^+)$ is of

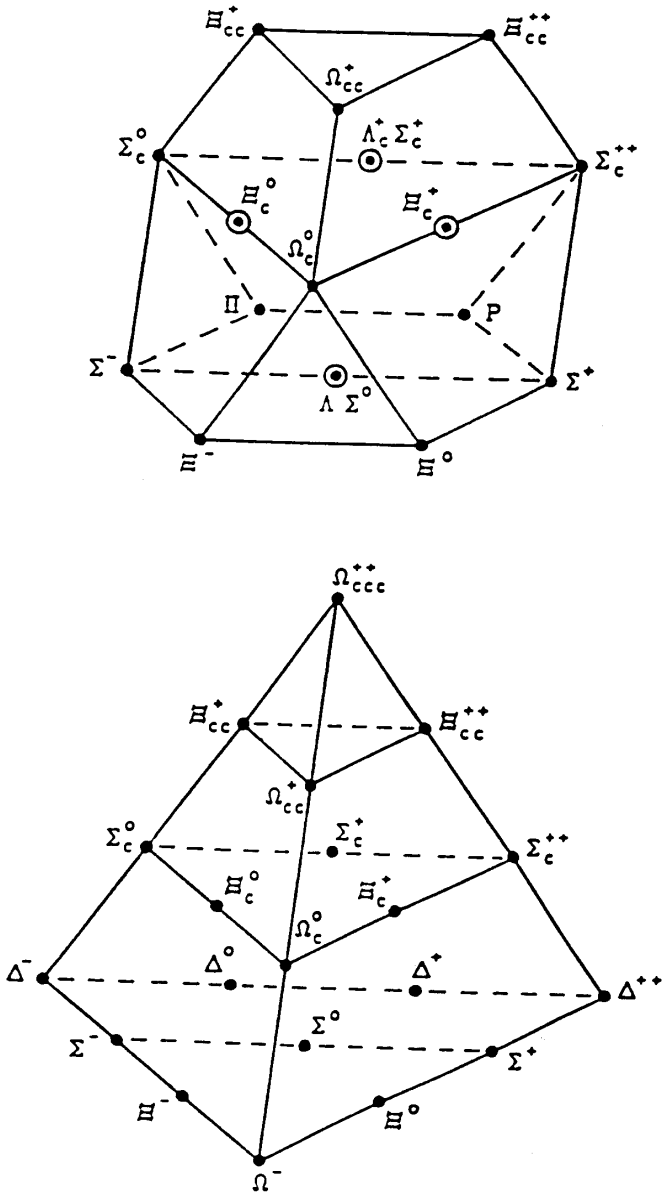

Figure 1.2. Baryon families predicted by the standard model: $J = 1/2^+$ multiplet (top), and $J = 3/2^+$ multiplet (bottom).

interest. (Also, experimental evidence for the $\Lambda_c^+ \rightarrow \Lambda^0\pi^+\pi^-\pi^+$ state is fairly recent so that most of its properties remain unknown.) Both decays are Cabibbo-allowed and the corresponding quark diagrams are shown in Figure 1.3. One might expect such an individual branching ratio measurement to indicate a globally preferred decay mechanism regarding baryon-meson strangeness correlation, but this is not the case: such individual relative branching ratio (RBR) results cannot be extrapolated to apply to inclusive lambda and proton/kaon decays of the Λ_c^+ . Also, no theoretical models exist which can predict these relative decay rates because the associated final-state interactions are too complex [Big 95].

Regarding the charm baryon Ξ_c^+ , the most natural decay for this baryon would seem to produce a final-state Ξ baryon (baryon-strangeness correlation) while one might expect transitions involving final-state Λ^0 and K^- to be more unlikely. Again, such expectations based on simple quark diagrams are difficult to substantiate so that one cannot investigate such decays in the context of theoretical predictions. However, a measurement of the RBR $B(\Xi_c^+ \rightarrow \Lambda^0 K^-\pi^+\pi^+)/B(\Xi_c^+ \rightarrow \Xi^-\pi^+\pi^+)$ would be interesting in and of itself because it has never been performed, and because the state in the denominator is a good candidate for observation as will be explained in Section 1.4. Even conclusive confirmation of the $\Xi_c^+ \rightarrow \Lambda^0 K^-\pi^+\pi^+$ state would be a major step forward. The Cabibbo-favored decay diagrams for each of these modes are shown in Figure 1.4. Indeed, final states of both charm baryons Λ_c^+ and Ξ_c^+ which contain lambdas represent frontier physics which is always interesting and exciting.

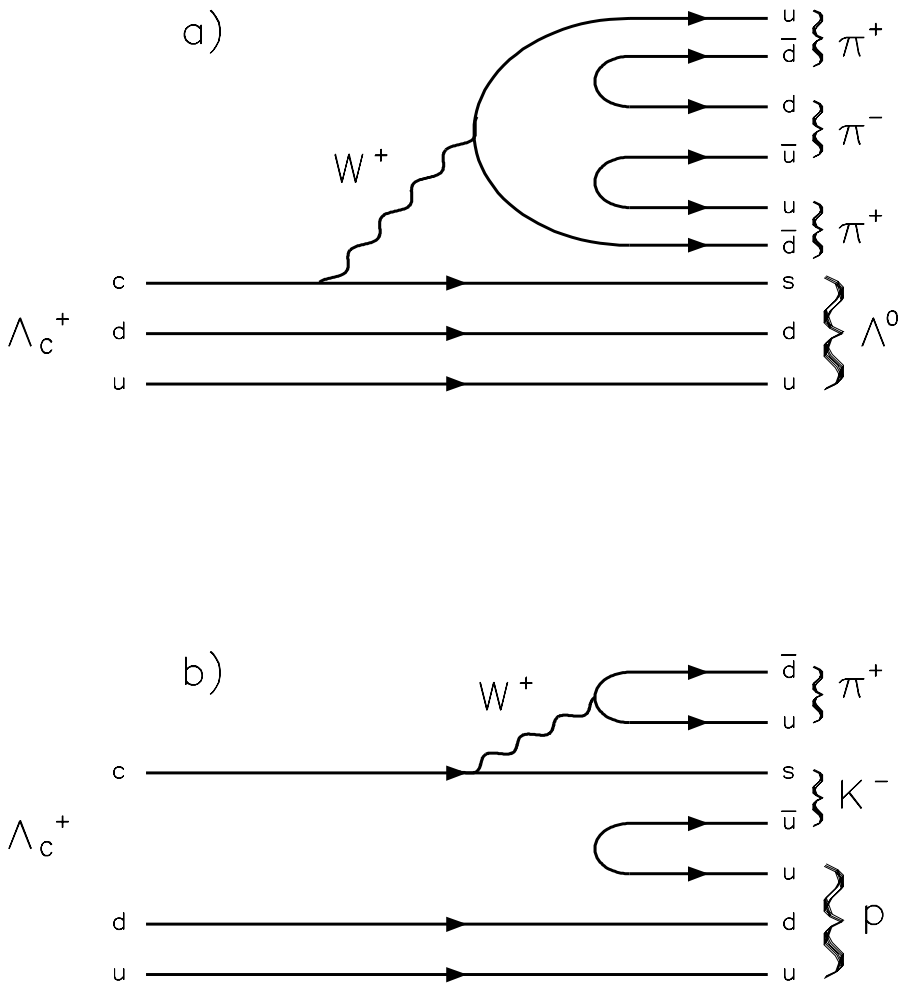

Figure 1.3. Examples of non-resonant spectator decay of a) $\Lambda_c^+ \to \Lambda^0\pi^+\pi^-\pi^+$, and b) $\Lambda_c^+ \to pK^-\pi^+$.

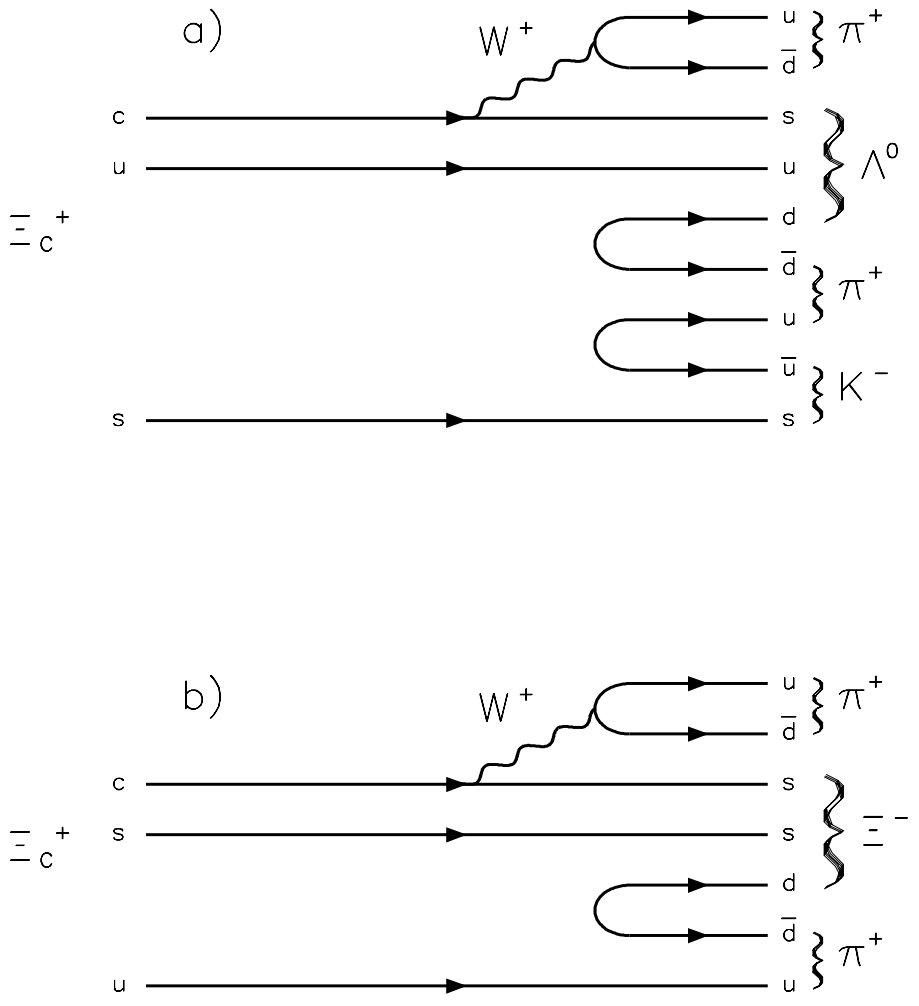

Figure 1.4. Examples of non-resonant spectator decay of a) $\Xi_c^+ \to \Lambda^0 K^- \pi^+ \pi^+$, and b) $\Xi_c^+ \to \Xi^- \pi^+ \pi^+$.

Table 1.1. $B(\Lambda_c^+ \to \Lambda^0\pi^+\pi^-\pi^+)/B(\Lambda_c^+ \to pK^-\pi^+)$

Value	Experiment (Year)	Technology	Fitted Events
$.65 \pm .11 \pm .12$	CLEO (91)	e^+e^-	289
$.82 \pm .29 \pm .27$	E691 (90)	γBe	44
$.94 \pm .41 \pm .13$	ACCMOR(NA32)(90)	π^-	10
$.61 \pm .16 \pm .04$	ARGUS (88)	e^+e^-	105
$.66 \pm .15$	World Avg.	—	—

1.4 Review of Current Literature

Although statistics for the $\Lambda_c^+ \to pK^-\pi^+$ and $\Xi_c^+ \to \Xi^-\pi^+\pi^+$ channels (the benchmark states involved in the branching ratio formalism) have accumulated in recent years, the $\Lambda_c^+ \to \Lambda^0\pi^+\pi^-\pi^+$ and $\Xi_c^+ \to \Lambda^0K^-\pi^+\pi^+$ modes have remained somewhat elusive. This is in no small part due to the problems which the neutral Λ^0 poses concerning the reconstruction of final states. One cannot directly observe the long-lived lambda as a track because it harbors no charge, hence it presents difficulties in determining vertex positions and thus observing particles. To date, only a handful of experiments have observed these specific charm baryon decays.

Four experiments have claimed to observe the $\Lambda_c^+ \to \Lambda^0\pi^+\pi^-\pi^+$ decay and have measured a branching ratio with respect to $pK^-\pi^+$; the results which include the respective $\Lambda_c^+ \to \Lambda^0\pi^+\pi^-\pi^+$ yields are summarized in Table 1.1 [Alb 88] [Anj 90] [Ave 91] [Bar 90]. Shown in Figure 1.5 are the signals each of these experiments has observed in the $\Lambda_c^+ \to \Lambda^0\pi^+\pi^-\pi^+$ channel, and one can see that some of them are either statistics-limited or background-dominated. An excellent opportunity exists for E-687 to measure $B(\Lambda_c^+ \to \Lambda^0\pi^+\pi^-\pi^+)/B(\Lambda_c^+ \to pK^-\pi^+)$ with a relatively small experimental error and to contribute significantly to the world average.

The $\Xi_c^+ \to \Lambda^0K^-\pi^+\pi^+$ decay presents an even greater challenge because of its

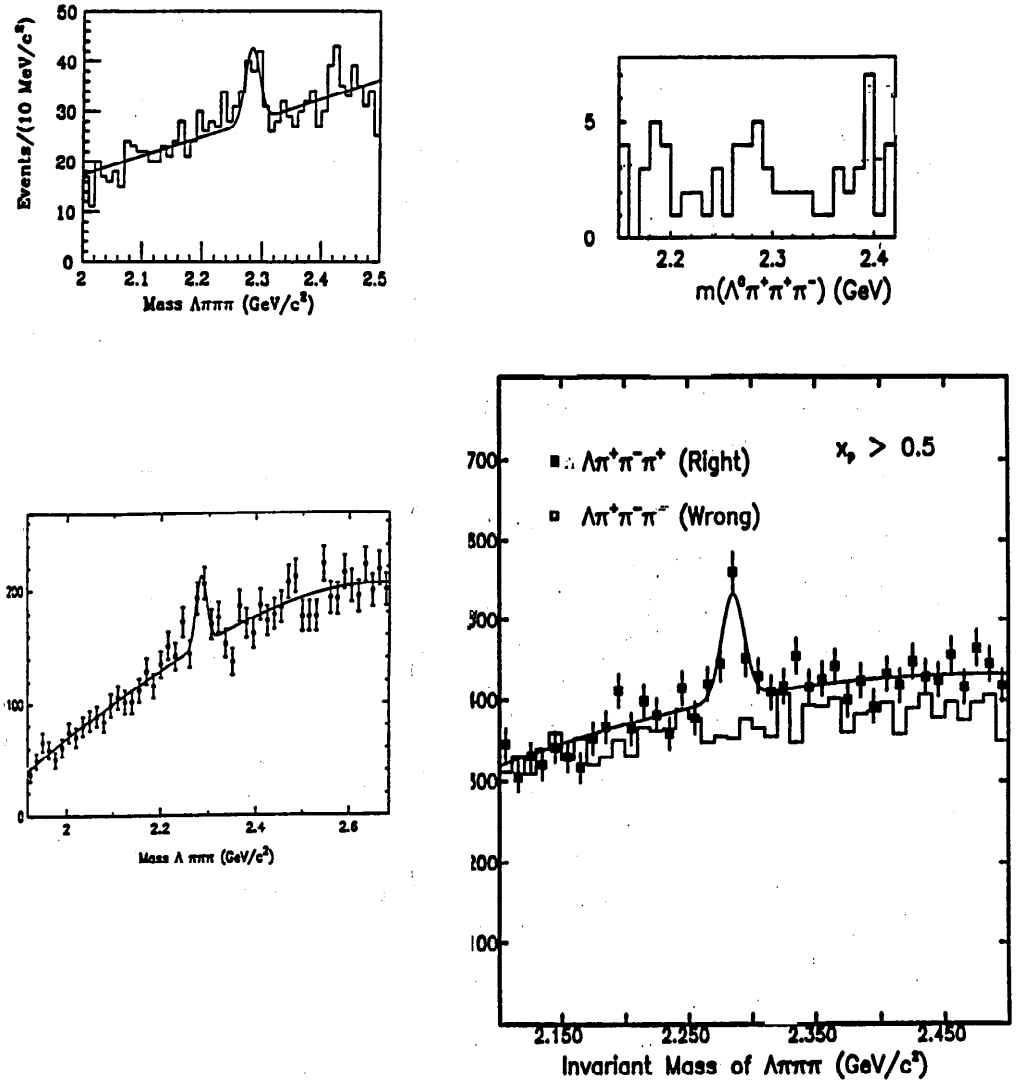

Figure 1.5. The four experiments to measure $B(\Lambda_c^+ \to \Lambda^0\pi^+\pi^-\pi^+)/B(\Lambda_c^+ \to pK^-\pi^+)$ have their $\Lambda_c^+ \to \Lambda^0\pi^+\pi^-\pi^+$ signals displayed here. Clockwise, from top left: E691 (44 events), NA32 (10 events), CLEO (289 events), and ARGUS (105 events).

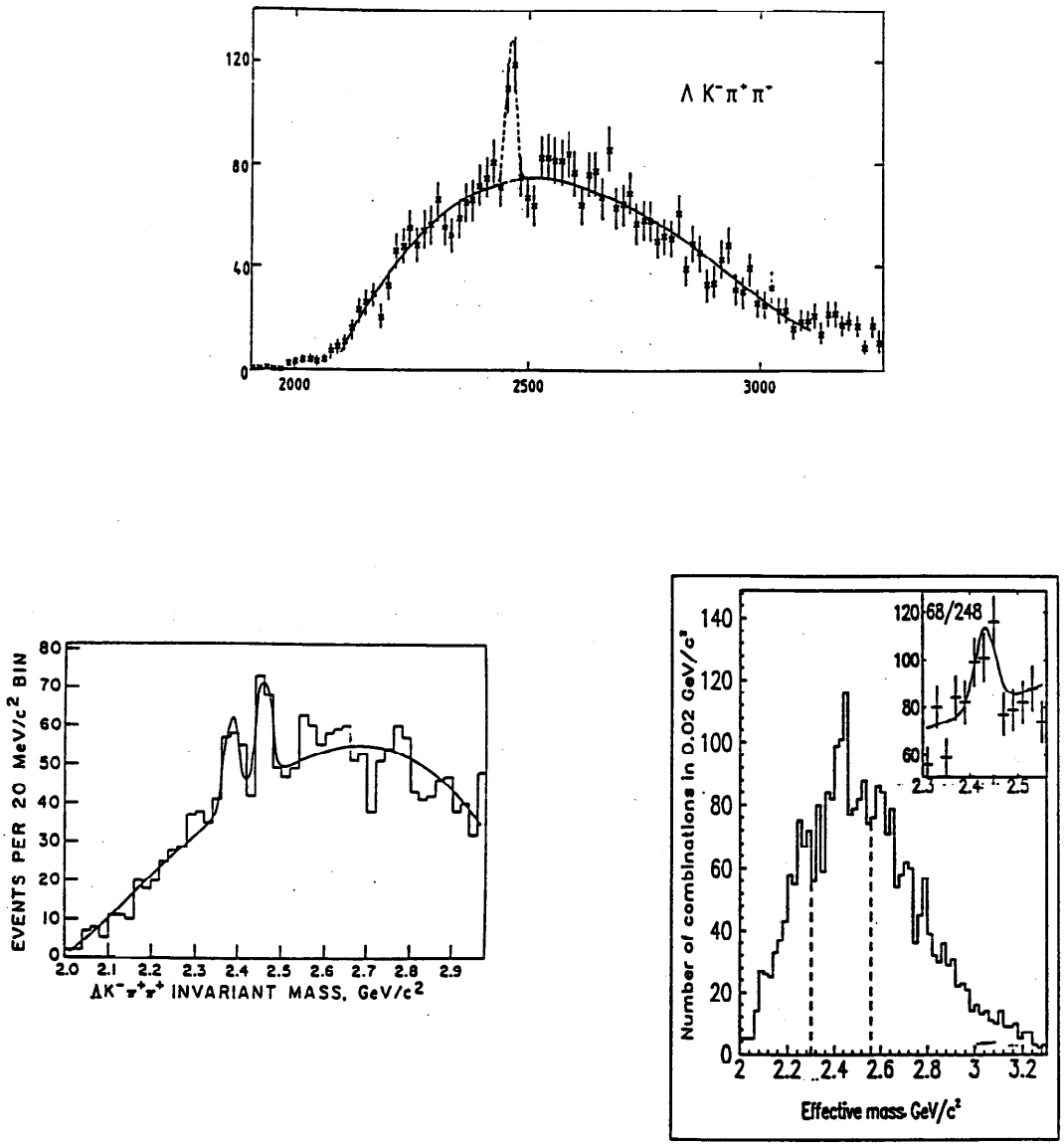

Figure 1.6. Only three experiments claim to have seen the $\Xi_c^+ \to \Lambda^0 K^- \pi^+ \pi^+$ state: WA62 (top, 82 events), E400 (lower left, 82 events), and BIS-2 (lower right, 68 events). WA62 and E400 measured the mass to be 2460 ± 5 MeV/c^2 while BIS-2 measured the mass to be 2437 ± 15 MeV/c^2 .

small production cross section and attendant large combinatoric background, and it escaped detection even from CLEO. Three experiments assert that they possess tangible evidence for this state as shown in Figure 1.6 [Bia 83] [Cot 87] [Kek 92]. Each of these projects was a fixed-target experiment and two of them (WA62 and E400) measured the Ξ_c^+ lifetime. To date, no one has measured a relative branching ratio of this baryon with respect to the $\Xi_c^+ \to \Xi^-\pi^+\pi^+$ state, a state which has recently been observed by various experiments [PDG 94] and may be an easier candidate for study than the state involving a lambda. The charge of the Ξ^- baryon coupled with its long lifetime enables it to produce a visible track which significantly aids in the formation of a secondary vertex. The E-687 collaboration recently measured the lifetime of the Ξ_c^+ decaying to the all-charged and very clean final state $\Xi^-\pi^+\pi^+$ [Fra 93a], and since this state has been observed, an opportunity might exist to observe the $\Xi_c^+ \to \Lambda^0 K^-\pi^+\pi^+$ mode and to measure the relative branching ratio $B(\Xi_c^+ \to \Lambda^0 K^-\pi^+\pi^+)/B(\Xi_c^+ \to \Xi^-\pi^+\pi^+)$.

1.5 Scope of the Thesis

To summarize, the goal of this thesis is two-fold: to measure the relative branching fraction $B(\Lambda_c^+ \to \Lambda^0\pi^+\pi^-\pi^+)/B(\Lambda_c^+ \to pK^-\pi^+)$ whereby the high statistics will contribute significantly to the world average, and to observe the $\Xi_c^+ \to \Lambda^0 K^-\pi^+\pi^+$ decay mode and thereby be the first to measure its decay rate relative to the $\Xi_c^+ \to \Xi^-\pi^+\pi^+$ state. We restrict the final-state topologies involving lambdas to contain three additional charged tracks in order to provide for well-defined secondary vertices.

The data were collected at the fixed-target, high-energy photoproduction experiment E-687 at Fermilab.[3] The experiment is described in Chapter 2. In Chapter

[3] Fermi National Accelerator Laboratory, Batavia, Illinois.

3, the data reconstruction and processing methods are discussed. The analysis techniques used to extract the charm baryon signals are presented in Chapter 4, and the branching-ratio analysis is described in Chapter 5. The results are summarized and concluding remarks are given in Chapter 6.

CHAPTER 2

The E-687 Apparatus

Fermi National Accelerator Laboratory (FNAL) experiment E-687 was commissioned in the summer of 1987 and ran intermittently through the winter of 1992. It was designed to study heavy quark (charm) production and decay resulting from the interaction of high-energy photons with matter. The apparatus consisted of the beam line, which created the high-energy photons and projected them toward the target, and the detector, which identified the products of the photon-nucleon interactions. The detection was accomplished by means of a large-acceptance, high-resolution multiparticle spectrometer which was situated downstream of the target.

2.1 Photon Beam

The tertiary bremsstrahlung photon beam results from a complicated but clever process designed to produce a beam free of contamination from charged particles and neutral hadrons. It is derived from protons which are supplied by an ionized hydrogen gas and then accelerated to 800 GeV in five stages in the Fermilab accelerator complex. The first part of this complex is a Cockcroft-Walton electrostatic accelerator which accepts negatively charged hydrogen ions and accelerates them to 0.75 MeV. These particles are fed into the linear accelerator (LINAC) and further accelerated to 200 MeV over a distance of 150 meters, where they then pass through a carbon foil. Here the ions are stripped of their two electrons, leaving the proton nuclei to be sent into the

Booster, a rapid cycling synchrotron 150 meters in diameter which accelerates them to 8 GeV. At this point the protons feed into the main ring in bunches. This apparatus is also a synchrotron accelerator with a radius of 1 kilometer, and it accelerates the protons to 150 GeV utilizing 1000 magnets of the conventional type. Finally, yet another synchrotron of radius 1 km energizes the protons to 800 GeV. This last synchrotron is the famous Tevatron, which employs 1000 superconducting magnets to attain the high magnetic fields needed for the high-energy protons. At this point, the protons are extracted from the Tevatron ring and transported to the switchyard, where they are distributed to three experimental beamlines: Meson, Neutrino, and Proton. The Wide Band beam line was a subsidiary of the Proton beam line, and utilized the proton beam to form the photon beam. The construction of the photon beam and the determination of its energy are described in the following subsections.

2.1.1 Photon Beam Construction

The goal of producing a high-energy contaminant-free photon beam was accomplished by means of the Wide Band beamline, which received approximately 2×10^{12} protons per 20 second spill (a schematic is shown in Figure 2.1). A complete description of this apparatus is given elsewhere [Fra 93b]. The process which produced the beam occurred in several steps. The protons from the Tevatron first interacted with a beryllium/deuterium target which represented one interaction length of material, producing charged particles ($\pi^+, \pi^-, K^+, K^-, p$, and $\overline{p}$) and neutral particles (π^0, γ, n, K^0). The charged particles were not desired in the process of forming the photon beam and were therefore swept aside by means of a set of sweeping magnets, while the neutral particles continued down the beam pipe unaffected. At this point, a photon beam existed which was free of charged-particle contamination, but contained long-lived neutral hadrons which needed to be discarded; at this point, the beam was

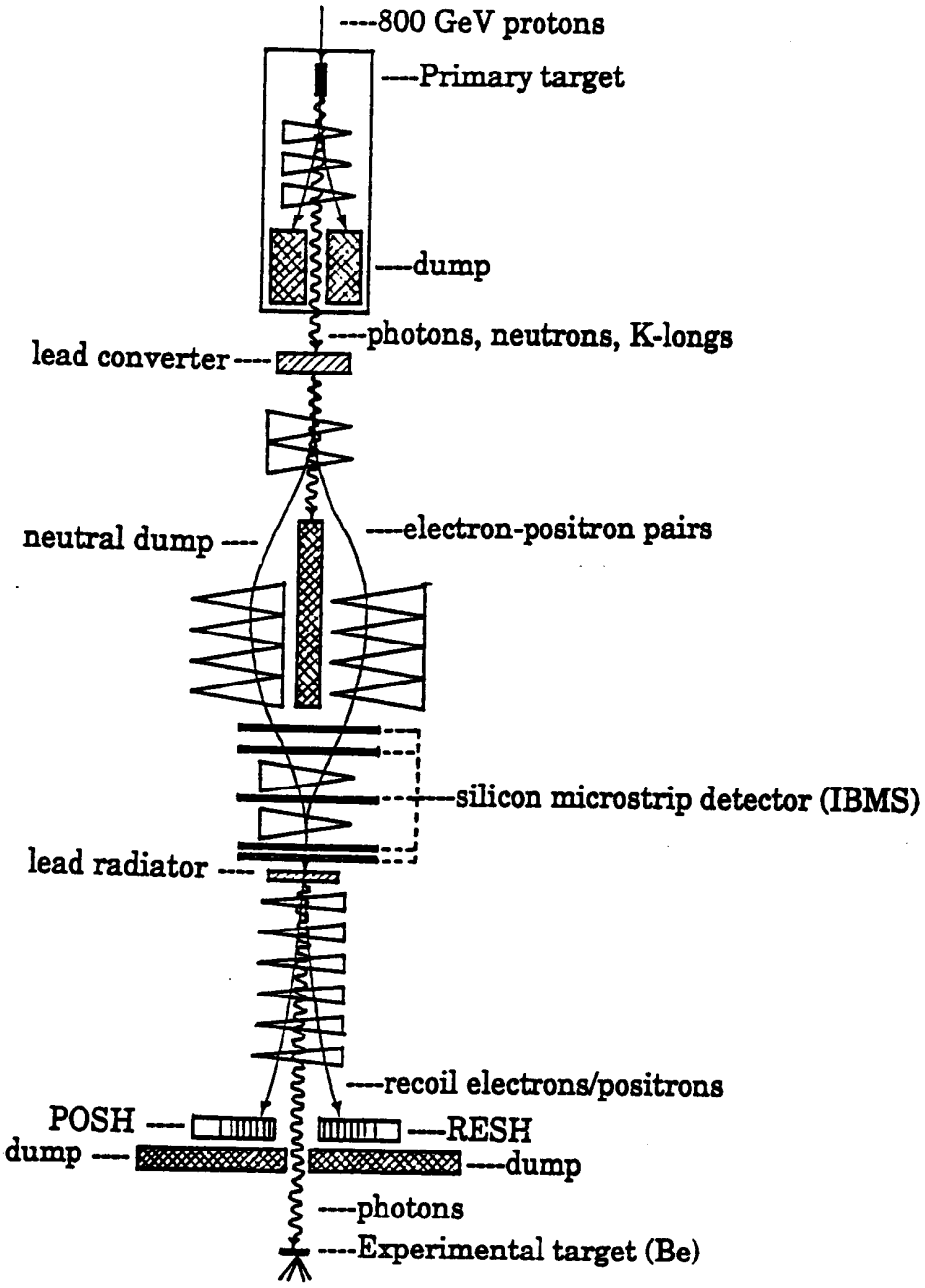

Figure 2.1. The E-687 beam line layout

comprised of approximately 50% photons, 50% neutrons, and a trace of K_L^0. The unwanted neutrals were purged from the beam by means of a "converter", which is a lead foil one radiation length thick through which the neutral beam passed. The incident photons were converted to e^+e^- pairs which were then detoured around a dumpsite (the "neutral dump") by a set of dipole and quadrupole magnets. The neutrons and K_L^0 along with any photons which passed through the lead foil and did not convert to e^+e^- pairs were absorbed in the dump. The beams of electrons and positrons recombined after bypassing the dump and continued down the beamline. At this point, an almost-pure beam of e^+ and e^- existed which was used in the final stage of this process to form the photon beam. The lepton beam possessed a broad range of momenta and angles, and the beam transport provided a large acceptance so that a high flux of particles could maintained. This system accepted e^+ and e^- with a mean momentum of 350 GeV and with a relatively large momentum spread of $\pm 15\%$: hence the name "Wide Band" beamline.

Finally, the contaminant-free beam of e^+ and e^- impinged upon a 20% radiation length lead foil and radiated photons by the bremsstrahlung process. An electromagnetic calorimeter received the recoil electrons which were diverted there by a string of dipole sweeping magnets, and the photons continued toward the target. For the most part this photon beam was free of neutral hadrons, although a small number (mainly neutrons) remained which was measured to correspond to less than 10^{-5} neutrons per photon. Table 2.1 summarizes properties of the Wide Band beamline. An upgrade to this beamline [Kas 88] was implemented after the 1987-88 run which involved a positron side of the charged particle transport system; the motivation was to double the photon yield. However, due to its higher background levels coming from π^+ and p it was not utilized to a significant extent.

Table 2.1. Wide Band beam properties

Quantity	Value
Horizontal spot size at production target	$\delta x = \pm 1$mm
Vertical spot size at production target	$\delta y = \pm 1$mm
Geometric horizontal angle accepted	$\delta\theta_x = \pm 1$mrad
Geometric vertical angle accepted	$\delta\theta_y = \pm 0.75$mrad
Geometric solid angle accepted	$\Delta\Omega = 6.0$ μsterad
Maximum momentum bite	$\frac{\Delta P}{P} \approx \pm 15\%$
Horizontal spot size at experimental target	$\delta x = \pm 1.25$cm
Vertical spot size at experimental target	$\delta y = \pm 0.75$cm
Horizontal divergence at experimental target	$\delta\theta_x = \pm 0.6$mrad
Vertical divergence at experimental target	$\delta\theta_y = \pm 0.5$mrad

2.1.2 Photon Beam Energy Determination

The Wide Band photon beam has a beam tagging system whose purpose is not only to measure the energy of the incident photon on an event-by-event basis, but also to require a minimum selectable electron energy in the second-level trigger. This is to ensure a sizeable flux of high-energy photons. The energy of the photon beam is determined by measuring the electron momentum before and after the radiator, and by measuring the energy of any non-interacting photons which are created by multiple bremsstrahlung. Three independent detectors accomplish this: the Incident Beam Magnetic Spectrometer (IBMS), the Radiated Electron Shower Hodoscope (RESH), and the Beam Gamma Monitor (BGM). The energy of the photon which interacts with the target (typically there is one interacting photon per event) is then

$$E_\gamma^{\rm int} = E_{\rm IBMS} - E_{\rm RESH} - E_{\rm BGM} \tag{2.1}$$

The estimate of the photon energy contains an uncertainty which arises from that of

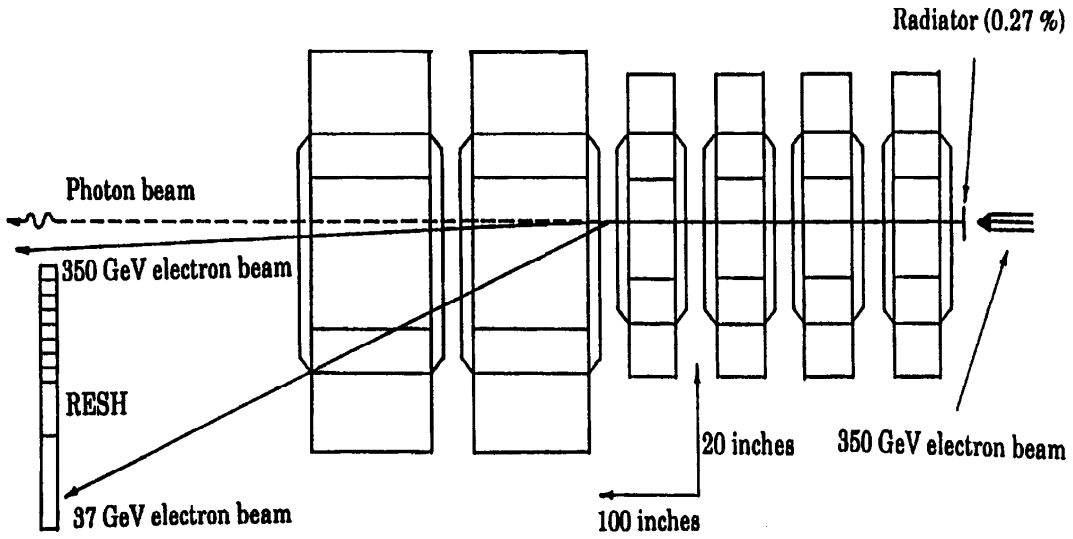

Figure 2.2. The Recoil Electron Shower Detector (RESH) layout

each of these terms, but the largest contributor was the ± 50 GeV momentum spread of the Wide Band electron beam. To aid in increasing the photon energy resolution the IBMS detector was installed for the 1990-91 run. It consisted of 5 silicon microstrip planes which measured the deflection angles of the e^+ and e^- as they passed through the beam transport system to the radiator. The silicon planes were 300 μm thick with a pitch of 300 μm and provided a 2.2% electron momentum resolution. This system was selected for its ability to maintain the high-intensity e^+e^- beam (more than 10^7 particles per second) and for its intrinsically fast time response.

The RESH detector was positioned 10.4 cm transverse to the beam pipe, and was located downstream of the sweeping magnets which deflected any charged particles which emerged from the radiator into a beam dump. The electrons which did not interact in the radiator did not deflect as much as those that did interact because

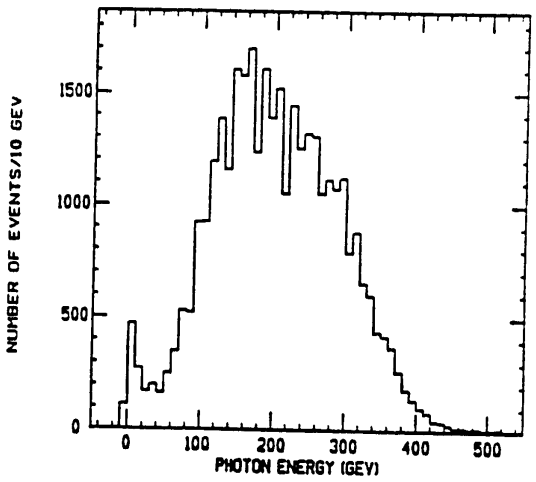

Figure 2.3. Tagged photon spectrum

they retained more of their original momenta, and this is why the RESH was offset from the beam line. This transverse offset yielded a minimum tagged electron energy loss of approximately 73 GeV.

A schematic of the RESH detector is shown in Figure 2.2. It consisted of 11 cells which were oriented transversely to the beam direction. The cells were either lead-lucite or lead-acrylic scintillator shower counters of 24 radiation-length depth, and were outfitted with RCA 8575 photomultiplier tubes and transistorized bases. The energy of the recoil electron was determined from the PMT pulse height and by the momentum determination from the deflection provided by the sweeping magnets and the transverse position of the cell which the recoil electron struck.

Finally, the energy of the non-interacting photons was measured by the BGM which was a shower counter located at the downstream end of the spectrometer. Lead and lucite comprised this counter which was 24 radiation lengths deep, and a single Amperex 58AVP photomultiplier tube provided the readout. The BCAL, or beam calorimeter, was used in the 1991 run to measure the energy of the non-

interacting photons, and was provided by experiment E-683. It was constructed of iron and scintillator, and consisted of two electromagnetic sections of 13 radiation lengths and 17 radiation lengths, respectively.

2.2 The E-687 Spectrometer

The E-687 Spectrometer [Fra 92] detected the decay products of the charm baryons and mesons. A schematic is shown in Figure 2.4. This detector was divided into two separate regions in order to maximize the geometrical acceptance. These regions were defined by the apertures of the two analysis magnets; acceptance angles of $\theta_x^{max} \pm 30$mrad and $\theta_y^{max} \pm 50$mrad defined the "inner" region, and $\theta_x^{max} \pm 100$mrad and $\theta_y^{max} \pm 150$mrad defined the "outer" region. This excellent apparatus provided charged particle tracking, charged particle identification, and energy determination of electromagnetic and hadronic showers. The hadronic calorimeter (HC) served principally as part of the second level trigger. Two electromagnetic calorimeters, two muon detectors, and three Čerenkov counters provided the charged particle identification, while the charged particle tracking was performed by a high resolution silicon microstrip system located just downstream of the target, and by a set of multi-wire proportional chambers (MWPCs) and two analysis magnets further downstream. The electromagnetic calorimeters also detected photons and therefore π^0's. Tables 2.2 and 2.3 display the locations and sizes of each of the detectors in the spectrometer.

A trigger was utilized in order to select desirable events which were characterized by hadronic decays as opposed to those originating from e^+e^- pair production which accounted for approximately 99% of all photon interactions occurring in the target. The trigger stamped each desirable photon interaction with a definite time interval, and during this period data were not taken because the good event was being processed.

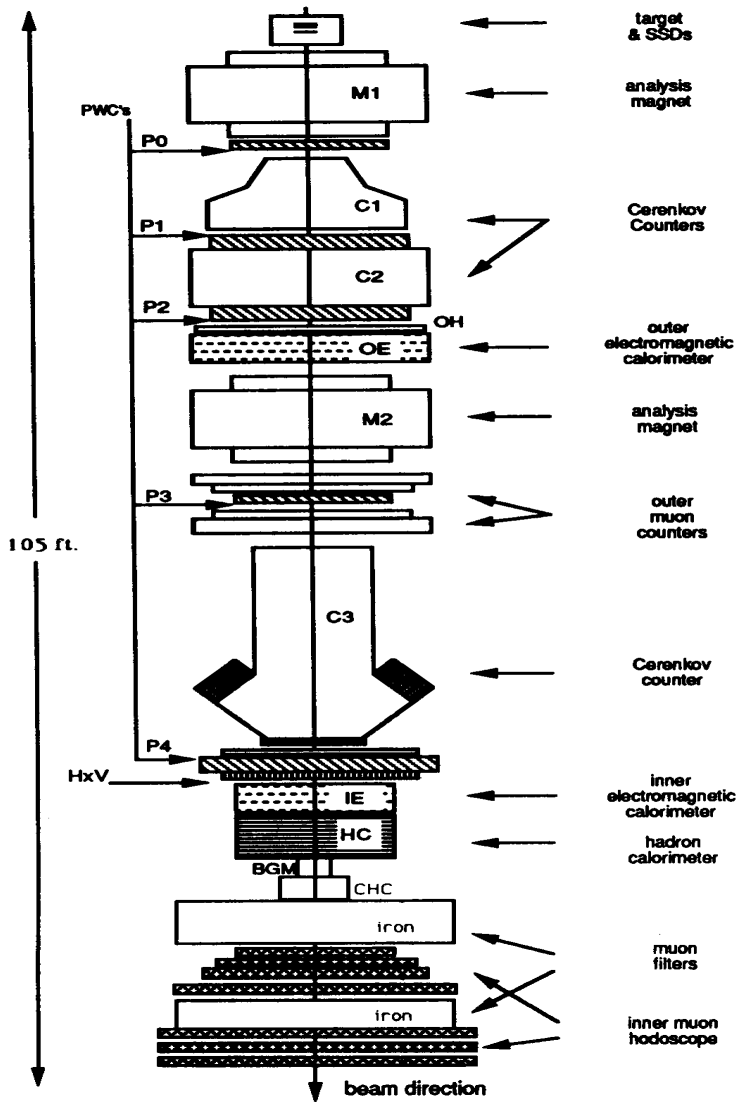

Figure 2.4. Schematic of the E-687 spectrometer

Table 2.2. Spectrometer components' dimensions and locations

Device	Z location[a] (cm)	Z length (cm)	Area (cm^2)
Be Target	-3.11	4.8	2.54×2.54
SSD-1	4.63	1.07	2.48×3.50
SSD-2	10.69	1.07	4.96×4.96
SSD-3	16.72	1.07	4.96×4.96
SSD-4	28.66	1.07	4.96×4.96
M1 Up. Shield hole	77.44	17.78	25.4×101.6
M1 Aperture	220.95	167.64	76.2×127.0
M1 Dwn. Shield hole	370.17	8.90	76.2×127.0
P0	405.08	17.78	76.2×127.0
C1	519.75	187.96	132.1×182.9
P1	644.26	17.78	152.4×228.6
C2	757.00	187.96	152.4×228.6
P2	878.47	17.78	152.4×228.6
OH	896.00	2.00	270.0×250.0
OH Aperture	896.00	2.00	48.6×83.2
OE	962.99	132.4	270.0×250.0
OE Aperture	962.99	132.4	48.6×83.2
M2 Up. Shield hole	1091.43	8.90	76.2×127.0
M2 Aperture	1238.11	167.64	76.2×127.0
M2 Dwn. Shield hole	1383.52	8.90	76.2×127.0
Outer μ Prop. X	1399.24	10.0	304.8×508.0
Outer μ Prop. X hole	1399.24	10.0	101.6×162.6
Outer μ Prop. Y	1416.94	10.0	304.8×508.0
Outer μ Prop. Y hole	1416.94	10.0	101.6×162.6
P3	1442.6	17.78	76.2×127.0

[a] Z position measured at the center of the device with respect to the Granite Block

Table 2.3. Spectrometer components' dimensions and locations (continued)

Device	Z location (cm)	Z length (cm)	Area (cm^2)
Outer μ Scint. Y	1474.56	15.0	304.8×487.7
Outer μ Scint. Y hole	1474.56	15.0	121.9×152.4
Outer μ Scint. X	1505.06	22.8	304.8×487.7
Outer μ Scint. X hole	1505.06	22.8	121.9×152.4
C3	1884.42	703.58	190.5×228.6
P4	2288.89	17.78	101.6×152.4
H$\times$V	2328.19	9.22	141.6×246.0
H$\times$V gap	2328.19	9.22	7.1×365.8
IE	2399.7	76.84	123.1×123.1
IE hole	2399.7	76.84	10.2×10.2
Hadron Calorimeter	2569.8	219.3	203.2×304.8
Hadron Calorimeter hole	2569.8	219.3	30.0(dia.)
Beam Gamma Monitor	2704.0	40.6	25.4×22.9
Central Hadr. Calorimeter	2778.0	101.6	45.7×45.7
Muon filter 1	2895.7	128.6	231.1×330.2
Inner μ Prop. X	2973.5	10.0	203.2×304.8
Inner μ Prop. Y	2993.2	10.0	203.2×304.8
Inner μ Scint. X	3012.5	15.3	213.4×304.8
Inner μ Scint. Y	3036.1	9.0	203.2×304.8
Muon filter 2	3079.7	63.0	231.1×330.2
Inner μ Prop. X	3139.0	10.0	203.2×304.8
Inner μ Prop. Y	3158.1	10.0	203.2×304.8
Inner μ Scint. Y	3178.3	9.0	203.2×304.8

2.2.1 *The Experimental Target*

For most of the run, a beryllium target of one shape and size or another was used to provide the photon-nucleon interactions. Typically, the target was constructed in the form of 5 blocks 4 mm thick, separated by thin gaps of air. The total length was about 4.5 cm, which corresponded to a radiation length of 11.5% and an interaction length of 10%. In addition to the beryllium target, two others were used for short periods of time: a silicon active target [Bel 92] and a scintillating fiber target [Mou 92]. Neither was used extensively in the data taking, but were instead utilized for testing purposes.

2.2.2 *Charged Particle Tracking*

Charged particle tracking in the region between the target and the first analysis magnet was performed by the silicon microstrip detector system (SSD) which was situated just after the experimental target. This amazing piece of equipment is largely responsible for the exploitation of the finite charm lifetime which is the main tool used in extracting charm signals. It achieves quite high positional accuracy which separates the primary (interaction) vertex from the secondary (decay) vertex. The SSD consisted of twelve microstrip planes grouped in four stations of three detectors each, and it measured the i, j, and k coordinates respectively: i at $-135°$, j at $-45°$ and k at $-90°$ with respect to the horizontal x-axis. A schematic of the SSD is displayed in Figure 2.5; 688 silicon strips with a pitch of 50 μm (25 μm in the first station) comprised this detector system. The innermost central region of the system has a resolution two times better than the outer one, and the smaller pitch of the first station also yields twice the positional accuracy of the others. Table 2.4 summarizes the SSD's geometry.

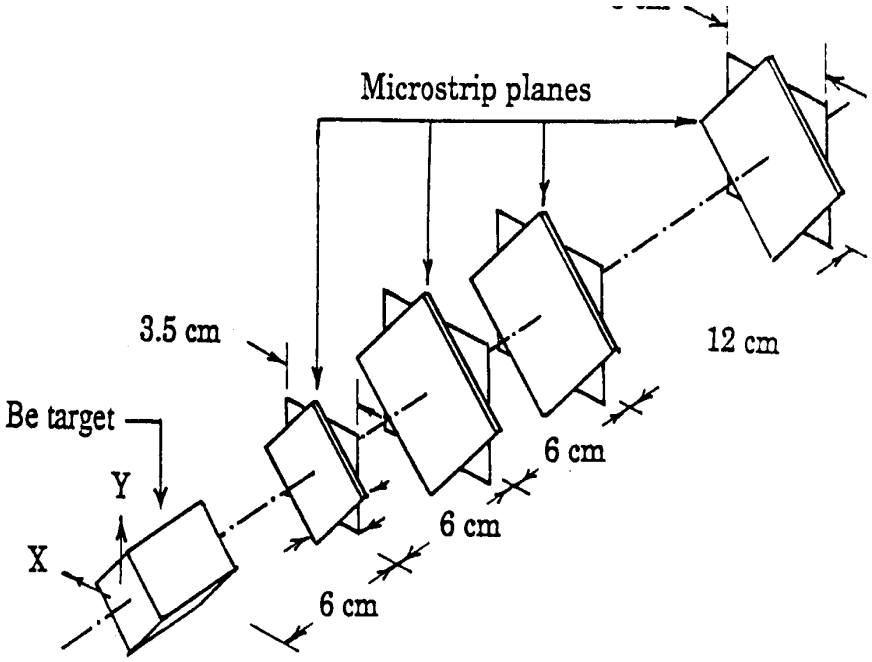

Figure 2.5. The layout of the silicon microstrip detector

Table 2.4. Properties of the silicon microstrip detector

Z-position[a]	I Station	II Station	II Station	IV Station
1^{st} detector	-0.5 cm	5.5 cm	11.5 cm	23.5
2^{nd} detector	0.0 cm	6.0 cm	12.0 cm	24.0
3^{rd} detector	0.5 cm	6.5 cm	12.5 cm	24.5
active area	2.5×3.5 cm^2	5×5 cm^2	5×5 cm^2	5×5 cm^2
High res.area	1×3.5 cm^2	2×5 cm^2	2×5 cm^2	2×5 cm^2
Strip Pitch	25.5μm	50.1μm	50.1μm	50.1μm
No. of channels	688×3	688×3	688×3	688×3

[a]Position measured relative to supporting granite block.

A front-end preamplifier, a remote-end amplifier, and a charge integrating FLASH ADC [Bel 86] [Inz 86] read out each strip, and the released charge information estimated the number of tracks involved in an event. The overall detection efficiency of each plane was measured to be better than 99%, and this estimate included broken electronics channels and/or non-functional strips. The position resolution was approximately 9 μm for very high momentum tracks which crossed the high-resolution regions of the twelve separate detectors.

A set of multi-wire proportional chambers located downstream of the first magnet performed the tracking. This system consisted of 20 signal planes grouped into 5 stations with 4 planes to a station; the stations were labeled P0, P1, P2, P3, and P4, upstream to downstream. The first three stations were located between the two analysis magnets, P0 being just downstream of M1. The fourth chamber P3 was located just downstream of M2 and P4 followed the last Čerenkov counter C3. Each station consisted of four views, each with a different orientation: X, Y, U, and V. The X-view (non-bend view) wires ran vertically, the Y-view (bend-view) horizontally, and the U and V view wires were situated at $\pm 11.3^{\circ}$ with respect to the Y-view. The U and V wires served as tie-breakers for ambiguous hits. Depending on the station, anode wire spacing was $2 - 3$mm. A 65% Argon/35% Ethane gas mixture was bubbled through ethyl alcohol at 0°C and then flowed to the chamber system, and the planes typically ran at voltages between 2.8 and 3.5 kV. Pre-amplifiers attached to the stations amplified and discriminated the signals from the PWC wires, and the resulting logic signals traveled to the counting room where they were read out by the LeCroy 4290 TDC system. Two identical large-aperture dipole magnets were used to measure the momentum of the charged particles. The magnets deflected the particles in opposite directions (along the Y-axis only), and the ratio of the kicks was chosen so that the particles returned to their original undeflected position near the downstream

Table 2.5. Analysis magnet specifications

Quantity	Value
Central field	14.0 KGauss
Maximum P_t kick	0.97 GeV/c
Field Uniformity	$\pm$2.5%
Steel yoke length	167.64 cm
Effective length	256.54 cm
Effective length/pole length	1.55
Total length	264.26 cm
Maximum current	2500 Amps
Voltage at max. current	160 Volts
Total power at max. current	400 kW
Total flow (50% glycol)	118 gpm
Pressure drop accross coils	150 psi
Conductor diameter	4.71 cm $\times$ 3.49 cm
Water passage diameter	1.55 cm
Total weight	272 Tons

end of the spectrometer. The first magnet, M1, was located 2.25 m downstream of the experimental target, and provided a 0.4 GeV/c transverse momentum kick in the positive-Y direction. The second magnet, M2, was located 12.40 m downstream of the target, and deflected the charged particle in the opposite direction with a kick value of 0.85 GeV/c. The steel yoke of the second magnet acted as the absorber for the outer muon detector located just behind it. Table 2.5 shows the characteristics of these magnets.

2.2.3 The Čerenkov System

Three multicell threshold counters comprised the E-687 conglomerate Čerenkov detector. The counters were labeled C1, C2, and C3, and were run in threshold mode at atmospheric pressure. The gases for the detectors were selected to provide a large range of momenta over which pions, kaons, and protons could be identified. A good

Table 2.6. Čerenkov system properties

Counter	Threshold (GeV/c)			No. of Cells	Gas
	Pion	Kaon	Proton		
C2	4.5	15.9	30.3	110	N_2O
C1	8.4	29.7	56.5	90	HeN_2
C3	17.4	61.5	117	100	He

Čerenkov system is crucial for distinguishing the light $\pi^{\pm}$ from the protons and kaons ("heavies") because both the $\pi^{\pm}$ and the heavies are present in charm signals. Tagging these particles in a specific fashion can be a powerful tool in isolating the true signals from the inevitable and often troublesome (especially for charm baryons) combinatoric background. Pions can be separated from heavies in the momentum range of 4.5 GeV/c, the C2 pion threshold, to 61.5 GeV/c, the C3 kaon threshold; unambiguous identification of protons from kaons occurs between 16 GeV/c and 56.5 GeV/c, and between 61.5 Gev/c and 117 GeV/c. Protons and kaons cannot be distinguished from each other from 56.5 GeV/c to 61.5 GeV/c, but can be differentiated from pions. The principal characteristics of these counters are given in Table 2.6.

Photomultiplier tubes of 2,3 and 5 inch diameters are used to instrument the counters, and these tubes detect the Čerenkov light which the medium radiates. Planar and/or focusing mirrors direct this light to the PMTs. There were low and high resolution regions within each of the detectors (in keeping with the expected density of the charged tracks) in order to alleviate the problem of track "confusion" resulting from overlapping light distributions. Figure 2.6 depicts plan views of the three Čerenkov counters.

The most upstream counter of the three was C1, located immediately downstream of the first analysis magnet M1 and between P0 and P1, the first and second PWC stations. It contained a helium-nitrogen gas mixture which provided an 8.4 GeV/c

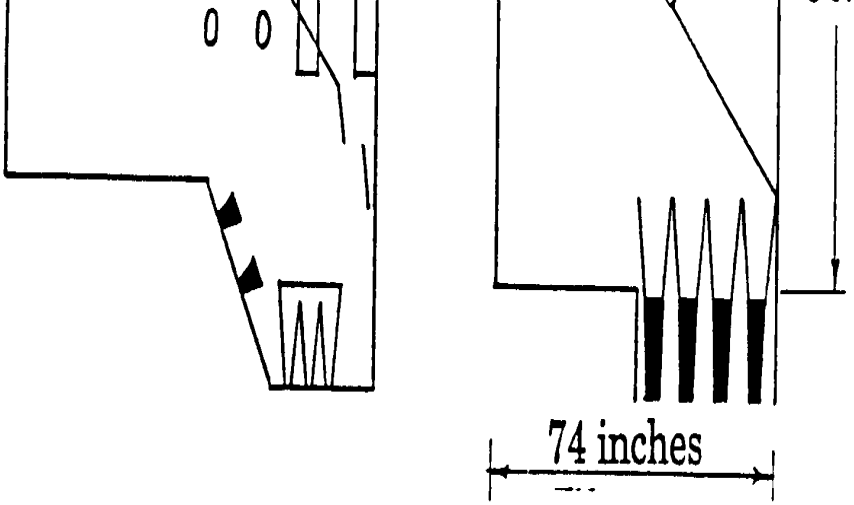

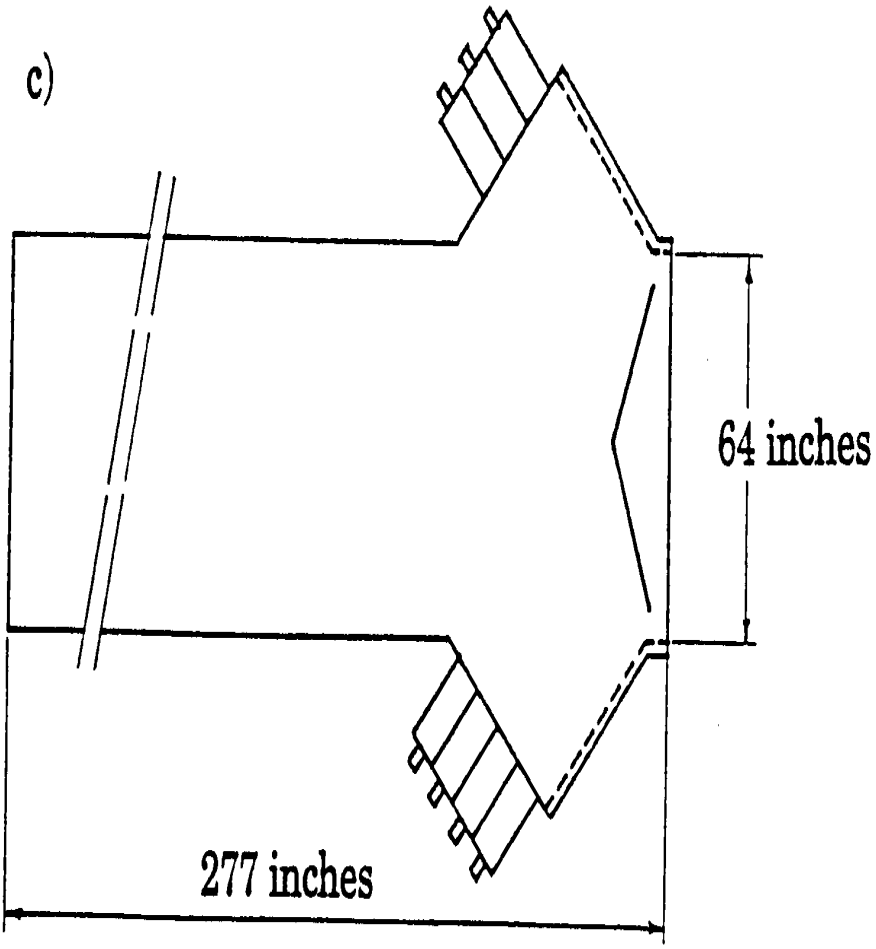

Figure 2.6. Plan views (schematics) of the three Čerenkov counters: a) C1; b) C2; c) C3.

pion threshold; the active transverse area of the counter measured 50 $\times$ 80 inches, and the total length of the volume of gas along the beam was 71 inches. It had 90 cells, and planar and focusing mirrors reflected the light to the photosensors. Usually, detected signals from each cell varied from 2.5 to 3.6 photoelectrons.

The second Čerenkov counter, C2, was located downstream of C1 and in between the second and third PWC stations, P1 and P2. It had 110 cells and an aperture of 90.5 $\times$ 100 inches along with a length of 74 inches along the beam direction. It possessed the lowest pion threshold of 4.5 GeV/c, and was constructed and maintained by Notre Dame. The inner high-resolution region cells were instrumented by Thorn EMI 9939A 2-in. photomultiplier tubes, and RCA 8854 5-in. phototubes were used in the outer detection region. The waveshifter p-terphenyl coated the faces of the phototubes in order to improve near ultraviolet light detection. Nitrous oxide gas was used, and two planar mirrors oriented at $\pm 45^{\circ}$ with respect to the beam direction reflected the Čerenkov light. Typical detected signal levels were between 5 and 15 photoelectrons per cell.

The final Čerenkov counter, C3, was located in between the third and fourth PWC stations (P2 and P3) downstream of the second analysis magnet M2. Having the highest pion threshold of 17.4 GeV/c, it was outfitted with 100 cells and 100 spherical glass focusing mirrors, each mirror corresponding to a given cell. It measured 277 inches along the beam line and had an aperture of 60 $\times$ 93.25 inches. Two and five inch photomultiplier tubes instrumented the inner and outer regions, respectively, and signal response varied from 3 to 17 photoelectrons.

A total of 300 channels with corresponding photomultiplier tubes and bases constituted the light gathering mechanism for the E-687 Čerenkov system. LeCroy Fastbus ADCs read the individual pulses and digitized them so they could be written to tape. Calibration was performed using muon and electron beams, and involved the average

photoelectron-equivalent response for each cell. Determination of the cell boundaries was also a part of the calibration, and these measurements compared favorably with the geometry obtained from a photosurvey.

2.2.4 The Muon System

Scintillator hodoscopes and proportional tubes comprised the muon system, which was divided into inner and outer region detectors. The inner muon (IM) segment was the most downstream component of the spectrometer; it was located beyond the inner electromagnetic calorimeter (IE), the hadronic calorimeter (HC), and several feet of steel absorber at the very end of the spectrometer. The outer muon (OM) detector was mounted at the back of M2, the second analysis magnet. This permitted the steel yoke of the magnet along with the OE material preceeding it to be used as an absorber.

2.2.5 Electromagnetic Calorimetry

Two lead-scintillator calorimeters detected photons and electrons in the experiment: the Inner Electromagnetic or IE calorimeter which covered the small-angle region of the spectrometer, and the Outer Electromagnetic or OE calorimeter which covered the wide-angle region. The IE sat downstream of P4, the last PWC station, and the OE sat just in front of the second magnet M2. Each was composed of one-inch and two-inch wide scintillation counters and lead strips positioned transverse to the beam. Pulse height information was gathered from a total of 1650 photomultiplier tubes and read out by LeCroy Fastbus ADCs where it was digitized for further processing.

2.2.6 Hadronic Calorimetry

Hadronic calorimetry was an extremely important part of experiment E-687 due to the fact that its main job was to reject the abundance of e^+e^- pairs which are produced when the high-energy photons interact with the target, and to keep events deemed hadronic which were likely to contain charm. It played an important role as part of the second level trigger. The hadron calorimeter actually consisted of two pieces of apparatus: the main hadron calorimeter (HC) which covered the region from 5 mrad to 30 mrad, and the central hadron calorimeter (CHC) which covered ± 5 mrad around the direction of the beam line. The HC was an iron gas sampling calorimeter with tower readout geometry. Twenty-eight iron plates totaling 8 interaction lengths were interleaved with gas/wire read out layers. The gas was a 50/50 mixture of Argon-Ethane, and contained anode pads which detected ionization from shower particles. The CHC detector was constructed of uranium scintillator of 6.4 interaction lengths and was read out by two photomultiplier tubes.

2.2.7 The E-687 Trigger

Since 99% of the particles produced in photoproduction experiments are e^+e^- pairs, a trigger must be employed which rejects these events if there is to be any hope of identifying charm signals from hadronic decays. E-687 utilized such a trigger which was organized in two levels: the first level trigger, or Master Gate (MG); and the second level trigger. The MG was a relatively simple trigger which required that a neutral particle produced an interaction in the target and that the spectrometer identified and accepted at least two charged particles which were decay products. The more complex second level trigger operated on signals which were produced during the duration of the MG and decided whether to keep the event or execute a clear cycle

so subsequent events could be processed. Its purpose was to keep the hadronic events by rejecting the e^+e^- pairs and to make certain that the photon which interacted in the target possessed a high enough energy.

The First Level Trigger (Master Gate)

The Master Gate functioned to reject events in which the photon beam contained charged particles, and to accept events where charged particles traveled through the spectrometer. The MG accomplished this task by employing sets of scintillation counters located at various points in the detector. These counters were divided into three categories, and covered the region of the geometric acceptance of the spectrometer. The categories were the veto counters, the experimental target counters, and the geometrical acceptance counters. The veto rejected events in which charged particles entered the target region from the direction of the photon beam, and it consisted in part of a simple scintillator paddle called A0 which was placed in the beamline just in front of the target. It was also composed of sets of larger counters, TM1, TM2, AM1, and AM2 which were situated at various points along the beam line to filter any charged particles which might be moving along the beam transport system. The experimental target counters were labeled TR1 and TR2 which were located upstream and downstream of the microstrip system, respectively, and which ensured that charged particles emanating from the target were captured by the microstrip system. Finally, charged particles in the inner region of the detector were found by sets of horizontal and vertical hodoscopes (H$\times$V) located just beyond P4, the last PWC station. An outer hodoscope (OH) was responsible for tagging charged particles in the outer region of the spectrometer, and it was located upstream of the outer electromagnetic calorimeter.

Signals from all these counters collectively required that no charged particle be

in the photon beam, that at least one charged particle emerged from the target and was caught by the microstrips, and that at least two charged particles were present in the remainder of the detector: either both were in the inner region, or one was in the inner region and one in the outer.

The Second Level Trigger

Specific physics requirements motivated the logic of the second level trigger, including hadronic energy above some threshold level, the presence of a muon in the spectrometer, or charged particle multiplicity. A logical .OR. of programmable trigger modules [Ste 87] composed the second level trigger. The electronics included partial triggers called buslines (up to 32 were available for use) whose signals were sent to the backplane of a CAMAC crate called the trigger generator crate. It contained pin logic modules, each of which occupied one slot and could produce one trigger. Any of the 32 buslines could be set to true or false, or any could be ignored. The main features of this trigger were: (1) $E_{Total} > 40$ GeV in the hadron calorimeter, (2) $E_{\gamma} > 110$ GeV as determined by the RESH, and (3) more than one hit outside the e^+e^- pair region in P0, the first PWC station. A successful second level trigger initiated a full readout and corresponding clear cycle. If the second level trigger was not satisfied within a processing time of 1.2 μs, a clear cycle of 1 μs was initiated. Each master gate which failed to produce a second level trigger generated a deadtime of 2.2 μs.

2.2.8 Data Acquisition

The E-687 data acquistion system [Pet 90] was able to record about 10,000 events per minute of 6 kilobytes each in size. The 30,000 channels of the DAQ were divided into five data streams, each ending with a LeCroy 1892 buffer memory located in a FASTBUS crate. The data were then transferred into ACP (Advanced Computer

Project) nodes, and subsequently written to four 8 mm exabyte drives. The data acquisition commenced when the second level trigger was satisfied; a 1.4 ms dead time was generated in order to prevent a pileup of events while the current events were being processed. The data were digitized and read into five memory buffers of 18 megabytes total memory to take advantage of the 20 sec/min beam cycle: while the beam was unavailable to the users, the current events were written from the buffers to the 8 mm tapes. The tape drives were only capable of processing 250 kilobytes per second. Over 500 million events which passed the second level trigger were written to 1000 tapes to be used to search for charm signals, and the first step in doing so was to reconstruct the raw events. This is discussed next.

CHAPTER 3

E-687 Data Reconstruction and Skims

Before charm signals could be explicitly searched for, it was necessary to process the 1000 raw data tapes obtained during the running periods. The processing is known as data reconstruction and involved analyzing the 500 million triggers by examining the pulse heights and hits from the different detectors in the spectrometer. The processing was divided into two stages: the data reconstruction and the skims. The former involved the formation of kinematic quantities of the events from the raw data and was carried out at Fermilab from Fall 1991 to Fall 1992. A farm system of IBM RS/6000s was employed for this gargantuan task, and the manpower involved a team of individuals working around the clock, submitting reconstruction jobs 24 hours a day, 7 days a week. Once the reconstruction was done, the skim, or data reduction was performed, and the resulting tapes were distributed to the various institutions involved in the experiment for further analysis.

3.1 Data Reconstruction

A set of programs collectively called PASS1 reconstructed the raw data. Charged particle trajectories and momenta were calculated; their identities were postulated; primary and secondary vertices were identified; neutral long-lived particles called "vees" (Λ^0 and K_s^0) were found; electromagnetic and hadronic showers and their energies were identified; and all the information associated with these quantities was

distilled and written to tape. Typically, one raw data tape produced two reconstructed data tapes, so it is evident that the sheer volume of data was impressive. The charm baryon branching ratio analysis in this thesis needed information from charged particles only (the neutral vees were reconstructed from charged particles), and utilized quantities such as trajectories, momenta, and Čerenkov identities. These are the subjects that will be discussed presently; a comprehensive description of the entire data reconstruction algorithm can be found in [Fra 92].

3.1.1 Tracking of Charged Particles

Two portions of the E-687 spectrometer were responsible for determining charged particle trajectories: the microstrip (SSD) system and the multi-wire proportional chamber (PWC) system. Information from each of the detectors was initially analyzed independent of its counterpart, and a subsequent portion of the analysis linked the fitted track segments to provide a complete description of the particle's trajectory through the spectrometer.

Microstrip Reconstruction

The microstrip tracking algorithm was based on projection finding in three separate views. This package, referred to as MICRORICO [Mor 88], was divided into three parts: analysis of the hits in the SSD, projection pattern recognition, and three-dimensional space track fitting.

First, an analysis of the valid hits in the SSD was performed on the basis of the amount of charge released in this system. The purpose was to resolve single and multiple track crossings in cases of adjacent hits, as well as to assign coordinate positions where tracks intersected the struck planes. The centroid of a strip was used as an intersection point in the case of an isolated hit. Two adjacent hits which

had total observed charge consistent with the crossing of a single minimum ionizing particle (MIP) produced an intersection point which possessed as its coordinate the centerline between the two strips.

Track projection finding was then performed along the three axes utilizing the aforementioned spatial coordinates. At least three hits per view were required, and hit sharing among tracks was allowed. Each projection also had to pass a loose χ^2/DOF test on a least squares fit to the hits in the SSD planes: $\chi^2/\mathrm{DOF} \leq 30$ for four-point tracks, and $\chi^2/\mathrm{DOF} \leq 20$ for three-point tracks. A soft arbitration was present in this procedure, namely, that hits in the last three stations could not be reused for a new track having only three hits, if these hits were already assigned to a track having hits in all four stations.

In the next stage, planar projections were formed into tracks if they matched in space and passed a test of the $\chi^2/\mathrm{DOF} \leq 8$. Three-dimensional tracks which shared one or two projections were then arbitrated according to their χ^2 values, and clusters of closely spaced tracks were formed into a single track where possible. Any hits not associated with a space track were used to search for wide angle tracks or highly multiple-Coulomb-scattered (MCS) tracks.

This algorithm produced a reconstruction efficiency of 96% as evaluated by a full Monte Carlo simulation of the microstrip system including "hot" strips, dead strips, and MCS effects. The relative percentage of spurious tracks was found to be approximately 2.7%.

Up to this point in the microstrip reconstruction algorithm MCS effects have been ignored since no knowledge of the track momentum was utilized during the track fitting. However, the silicon material which comprised the microstrips caused this type of scattering and it must be accounted for especially at later points in the

analysis. Including MCS effects, the resolution of a microstrip track was found to be:

$$\sigma_{\mathrm{x}} = 11\mu\mathrm{m}\sqrt{1+\left(\frac{17.5GeV}{p}\right)^2} \tag{3.1}$$

$$\sigma_{\mathrm{y}} = 7.7\mu\mathrm{m}\sqrt{1+\left(\frac{25.0GeV}{p}\right)^2} \quad . \tag{3.2}$$

Multiple Coulomb scattering effects are represented by the second term under the radical.

PWC Analysis

The main differences between the PWC tracking routines and the SSD tracking routines are that (1) the chambers were on either side of M2, the second analysis magnet, and (2) there were four views to each PWC station. The magnet deflected tracks in the y direction, so that deflections were seen in some of the track projections. The fact that there were four views to a station meant that hits which led to ambiguities in the x and y position could be resolved; four views were also needed because the wire chambers were less efficient and noisier than the SSD channels.

Hit information from twenty planes was used to form the tracks in the PWC system; the routines were designed to reconstruct tracks which left hits in 3, 4, or 5 stations. A candidate track was first required to have hits in P0, the first station. These hits were then matched with hits in P2, the third chamber, and confirming hits were searched for in P1 which was located between P0 and P2. Projections from the three views Y,U, and V were formed from PWC information only; the non-bend X-view projections were constructed by finding PWC hits which matched microstrip

track extensions. The tracks were formed by matching all four projections. After all the tracks were found which had components from the X-view microstrip track extensions, any hits in the X-view which went unused were utilized to make additional X projections. The matching procedure with the three other views was then repeated. If hits were found in P0, P1, and P2, the resulting segment was dubbed a "stub"; if confirming hits were then found in P3 and P4 the stub was upgraded to a "track".

All candidate tracks were subject to a least squares fit; the parameters were slopes and intercepts of the tracks in the X and Y views with respect to the bend center of M2. For 4 or 5 chamber tracks, another parameter was present: the change in slope in the Y-view between the track segments upstream and downstream of M2. A χ^2 per degree of freedom cut was applied to each candidate track, and candidate tracks were not allowed to have more than four missing hits among all planes nor more than two missing hits in any one station. Some tracks shared projections with others, and these were arbitrated on the basis of the χ^2. Higher order corrections to the linear least squares fits were administered due to finite magnet length and fringe fields outside the magnets. Also, additional routines were employed to recover tracks that might have had missing hits in any of the chambers; e.g., tracks with hits only in the first two PWC stations P0 and P1.

The overall efficency for PWC track reconstruction was found to be approximately 98% for tracks with momenta greater than 5 GeV/c, and a spurious track incidence of less than 1% was determined. Finally, since events with apparently high multiplicities usually resulted from electrical oscillations in the PWC system, the total number of reconstructed tracks per event was limited to 30 or less. This also saved processing time, which was of no small concern.

Linking of SSD and PWC Tracks

Linking the PWC tracks to the SSD tracks is one of the most important facets of the data analysis, for it determines the momenta of tracks which were recorded in the microstrip system and which passed through M1. The high resolution microstrip information is essential for determining precise primary and secondary vertex positions; the separation of these vertices is the main tool used in eliminating combinatoric background for charm signal extraction. Also, the fact that some PWC tracks do not link to SSD tracks may be significant. An example would be isolating the neutral vees and kink decays, for these particles typically travel several meters in the spectrometer because of their long lifetimes. They usually decay after having passed through the microstrips and leave tracks only in the PWC system. Another example of the importance of linking is that the rejection of unlinked SSD tracks serves to remove combinatoric background when searching for charm decays.

The linking of SSD and PWC tracks was accomplished by comparing the extrapolated positions of the respective tracks at the center of the first analysis magnet, M1. For the x and y views, the difference between the slopes and intercepts of the tracks was calculated. Candidate links with slope and intercept differences within a certain range were subjected to a global least squares fit using all the hits in both detector systems. If the candidate linked track was a 5-chamber track, the bend angles in each magnet were required to be consistent. The linking procedure permitted one microstrip track to link to a maximum of two PWC tracks, but a PWC track was only allowed to link to one microstrip track. This was principally to allow e^+e^- pairs which were formed in the target or the SSD system to link properly.

The linking efficiency as a function of momentum for 3 and 5-chamber tracks was determined by projecting all PWC tracks to the SSD vertex, and then by checking to

see if they were linked. For 3 and 5-chamber tracks, the respective linking efficiencies were measured to be 91.4% and 97.0% for track momentum greater than 50 GeV/c. At low momentum these efficiencies fall because MCS effects inside the microstrips cause track loss.

A special recovery program was constructed in order to further improve the linking efficiency. Missing microstrip tracks were searched for by tracing unlinked PWC tracks back to the target and endeavoring to match them with unused SSD hits. This increased the efficiency of 3-chamber tracks by 2.5% (to about 94%) and 5-chamber tracks by 1.5% (to over 98%).

3.1.2 Momentum Determination

Charged particle momentum was calculated according to the amount of deflection in the magnetic fields of the first and second analysis magnets. The momentum was determined by M1, M2, or both depending on the track topology. The momentum resolution was calculated to be [Wis 88b]

$$\frac{\sigma}{P} = 3.4\% \left(\frac{P}{100\,GeV/c} \right) \sqrt{1 + \left(\frac{17GeV}{P} \right)^2} \quad \text{for M1} \tag{3.3}$$

and

$$\frac{\sigma}{P} = 1.4\% \left(\frac{P}{100\,GeV/c} \right) \sqrt{1 + \left(\frac{23GeV}{P} \right)^2} \quad \text{for M2.} \tag{3.4}$$

As with the microstrip resolution, the second term under the radical indicates the MCS effects.

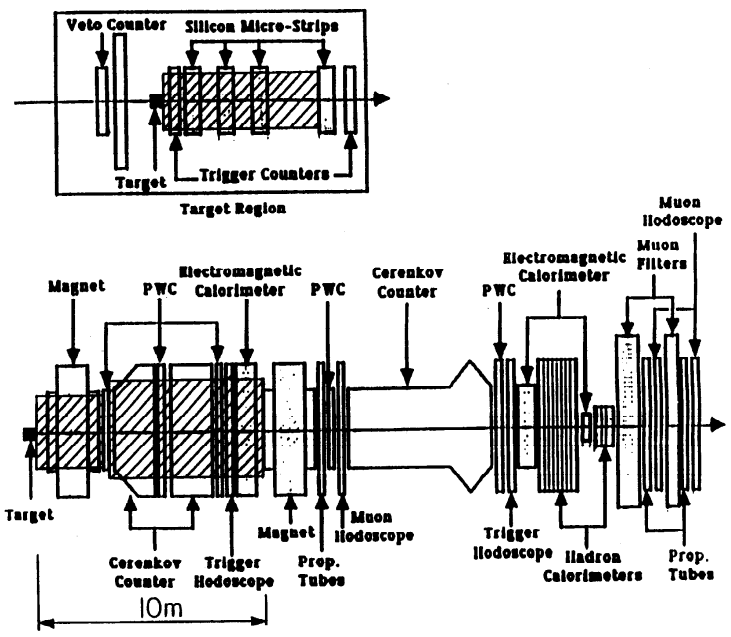

Figure 3.1. Schematic of the E-687 spectrometer. The upper portion of the figure represents the target region and the silicon microstrip detector. The hatched areas indicate regions in which neutral vees could be reconstructed.

3.1.3 Neutral Vee Finding

The term "neutral vee" refers to either the K_s^0 meson or the Λ^0 baryon. Each of these particles contains one strange quark and decays weakly to two charged particles.[1] The decay topology resembles the letter V. The lifetimes of these particles are on the order of 10^{-10} seconds, so that they may travel several meters in the lab frame before decaying. For the analysis presented here, the focus will be directed to the $\Lambda^0 \to p\pi^-$ decay (branching fraction 64.1%) because the charm baryon decays which this thesis examines involve this baryon. (The charge conjugate state, $\overline{\Lambda^0}$, is implied throughout this work.)

[1] Actually, these particles also decay into uncharged channels, e.g., $\Lambda^0 \to n\pi^0$ 36% of the time. The experiment did not reconstruct all-neutral vee decays.

The Λ^0 candidates were detected according to their decay coordinates in the spectrometer; Figure 3.1 indicates the detector regions where they could be reconstructed. The topologies for reconstructed Λ^0 events were defined in terms of the reconstructed track types of the daughter proton and pion:

- SSD: a Λ^0 decaying before the first microstrip plane, and comprised of two linked SSD-PWC tracks;
- MIC: Λ^0 decaying between the first and last microstrip planes, comprised of two unlinked PWC tracks extended into the SSD system utilizing unused hits from the microstrip tracking algorithm;
- TT: "Track-Track" Λ^0 (two 5-chamber, unlinked PWC tracks);
- TS: "Track-Stub" Λ^0 (one unlinked 5-chamber PWC track and one unlinked 3-chamber PWC track);
- SS: "Stub-Stub" Λ^0 (two unlinked stubs);
- RECON: "Reconstruction" Λ^0 (unused PWC hits for decays between P0 and P2);
- P23: "P23" Λ^0 (unused PWC hits for decays between P2 and P3) .

In all cases the momenta of the two tracks were compared, and the track with the greater momentum (the "fast" track) was assigned the proton mass, while the "slow" track was assigned the π^- mass. The invariant mass of the Λ^0 was calculated according to these hypotheses and loose mass windows further tightened the selection of Λ^0 candidates. A brief discussion of each of the vee categories follows.

Microstrip Region Λ^0

Two types of lambdas were reconstructed by the microstrip system: the SSD lambdas which consisted of fully reconstructed and linked tracks, and the MIC lambdas, which were composed of PWC tracks that extended into the microstrip system, but did not leave hits in every plane since these vees decayed after they passed the first microstrip plane.

Linked pairs of oppositely charged SSD-PWC tracks constituted the SSD vee category. The PWC track which corresponded to the microstrip track was not permitted to be linked to another microstrip track. The two track combinations were fitted to form a vertex which was required to be a certain normalized distance away from the primary vertex, and whose confidence level had to be greater than 1%.

The second group of microstrip region lambdas, MIC vees, was recovered through the use of unused SSD tracks since they decayed somewhere between the first and last microstrip planes. Unlinked PWC tracks were pointed back into the fourth station of microstrip planes and matching hits in this station were sought. If found, the track parameters were recalculated using this new information; the search was then continued by extending this "new" track into the third microstrip station, and so on. The candidate tracks were then tested for distance of closest approach. Since problems in the MIC vee routines were present, these vees were not used in the charm baryon analysis. The discussion here is for the sake of completeness.

Magnet Region Λ^0

This category of vees comprised the largest Λ^0 sample obtained in the experiment. It consisted of those lambdas which decayed in the vicinity of M1, the first analysis magnet, and which were composed of pairs of oppositely charged unlinked PWC tracks and/or stubs. Such two-track combinations (TT, TS, SS) were analyzed; in

each category the X-projections of the component tracks were intersected so that an estimate of the Z-coordinate of the vee could be obtained. Often the Z-decay was inside M1. Therefore, a magnetic tracing algorithm was employed which determined the Y-coordinate of the vee decay vertex, which would then in turn find a new Z-position. The process was repeated until a convergence condition was satisfied and combinations failing to meet the condition were rejected. Candidate lambdas containing stubs were subject to the additional constraint that the vee point back to the primary vertex.

Next, the Λ^0 candidate tracks were refitted [Wil 89] according to the constraints that the vee originated from a common vertex, decayed before P0, and pointed back to the primary vertex. If the fit was successful the vee momentum vector, the invariant $p\pi^-$ mass, and the mass error were calculated using the fit parameters; if not, track parameters from the magnetic tracing algorithm were used to determine these quantities. Vees which failed the fit were kept but were flagged with a fit-quality variable QDV=0, while vees which passed the fit were assigned QDV=5.

Reconstruction Λ^0

The highest momentum lambdas which decay downstream of P0 comprise this category of vees which includes the RECON and P23 vee types. Since the daughter tracks left no hits in P0 these vees were termed "reconstruction vees" for they had to be reconstructed from chamber hits rather than tracks. The topologies included three or four chamber vees which left hits in P1, P2, P3, or P4; or two chamber vees whose daughter tracks hit P2 and P3 (these are the P23 vees). Only hits left over from the principal track reconstruction scheme were utilized. The algorithm involved first aligning hits in the X-projection and then forming track candidates by pairing two good X-projections and matching them in the Y, U, and V views.

Čerenkov restrictions needed to be placed on the vee candidate tracks in order to expose good signals for certain vee categories, the details of which will be discussed in a following section on skims; mass plots of the lambdas will also be displayed there.

3.1.4 Particle Identification by the Čerenkov System

The E-687 Čerenkov system was designed to identify charged particles, and to distinguish electrons, protons, kaons, and pions from each other. The algorithm utilized the pulse height information of the 300 cells of C1, C2, and C3 and a set of parameters which specified counter thresholds, mean photoelectron cell yields, and counter geometries.

Counter thresholds were devised in order to provide good particle identification among the aforementioned particles over wide momentum ranges. Muons were not differentiated from pions because the two species' masses differ minimally. The Čerenkov detectors work in the following fashion. When a charged particle traverses the activating medium (gas, in this case) the medium will emit Čerenkov light if the speed of the particle exceeds the speed of light in that medium. The magnitude of the threshold velocity for this phenomenon to occur is given by

$$\beta_{th} = \frac{1}{n} \quad . \tag{3.5}$$

Using the relativistic relation $p = \gamma m \beta$ where p is the magnitude of the momentum of the particle and m is its mass, it is straightforward to obtain the expression for the threshold momentum of the particle that will produce Čerenkov light in terms of the

index of refraction of the medium:

$$p_{th} = \frac{m}{\sqrt{n^2 - 1}} \quad . \tag{3.6}$$

The Čerenkov analysis [Wis 88a] proceeded as follows. First, each cell in each of the three counters was examined in order to generate an on or off code for that cell. The pulse height from the cell in question was compared to a threshold (typically several picocoulombs above pedestal) to determine the on or off status. Each main spectrometer track was then projected through the three counters to find its corresponding light cells, which included the cell through which the track passed and any adjacent cells. The expected amount of light in a certain cell depended on track momentum, particle hypothesis, and the overlap of the Čerenkov cone with the cell area. An anticipated light yield based on photoelectron yield gathered from calibration studies was calculated for each of the relevant cells corresponding to the given track, and was done so for pion and electron hypotheses depending on the track momentum. Iterations were performed and the better hypothesis was selected. The counter was called "ON" if the observed pulse height was greater than the threshold for the track, and "OFF" if otherwise. Sometimes the counter could be called "CONFUSED", a nomenclature which referred to cases in which more than one track could contribute to the relevant cell(s).

At this point, the counter status (ON, OFF, or CONFUSED) was compared to its threshold and to the track momentum for a chosen particle hypothesis. The track momentum was assigned to one of seven momentum regions: four which came from electron, pion, kaon, and proton thresholds; and three owing to transition regions. Such regions exist because the response of the counter is characterized by gradual increases in light yield rather than toggle switch behavior. Monte Carlo studies have

Table 3.1. Values assigned to the Čerenkov ISTATP variable

ISTATP	Identification
0	Inconsistent information
1	$e^{\pm}$
2	$\pi^{\pm}$
3	$e^{\pm}$ or $\pi^{\pm}$
4	$K^{\pm}$
7	$e^{\pm}$,$\pi^{\pm}$ or $K^{\pm}$
8	$P^{\pm}$
12	$K^{\pm}$ or $P^{\pm}$
14	$\pi^{\pm}$, $K^{\pm}$ or $P^{\pm}$
15	$e^{\pm}$, $\pi^{\pm}$, $K^{\pm}$ or $P^{\pm}$

shown that these regions are small, extending from the given threshold to 1.08 times the threshold.

Next, a four bit status word was set for each counter, starting with the least significant bit. Each bit corresponded to a certain particle hypothesis, thus:

- Bit 1: Electron status
- Bit 2: Pion status
- Bit 3: Kaon status
- Bit 4: Proton status

The bit was on if the hypothesis was satisfied and off if not, and the resulting words from each of the three counters were logically AND-ed to create the Čerenkov identification variable, ISTATP. The values and interpretations of ISTATP are listed in Table 3.1. For example, "heavy" particles consistent with being protons or kaons might have ISTATP equal to 8 or 12. These Čerenkov codes will be employed in the charm baryon analysis.

3.2 *Vertexing*

Before discussing the data reduction skims appropriate to the charm baryon analysis a brief discourse concerning vertexing is in order, since one of the baryon skims (and all of the final-state analyses) utilized a candidate-driven vertexing algorithm.

The candidate-driven vertex analysis [Cul 91] commonly referred to as SUPERDVERT (or SDVERT) selects a specific final state to be studied and determines all particle combinations in an event which are consistent with that state. One selects the particles on the basis of kinematics, charge-strangeness correlation, and Čerenkov identification to form a new "track" consistent with emerging from the primary vertex; e.g., a charm baryon track. This method calculates the total momentum of the resultant combination, defines it as a new track, and attempts to build a primary vertex around this charm vector. It then fits each set of tracks to its respective vertex, and measures the quality of these fits according to probability distributions of the resulting χ^2/DOF values. If these confidence levels are within specified limits the fits are termed successful, and the algorithm then calculates the separation significance of the two vertices, L/σ_L , which is the distance L between them divided by the error in this distance. This characteristic of well-separated spatial decays of charm events provides the experimentalist with a powerful tool to isolate charm signals from combinatoric background.

3.3 *Charm and Non-charm Baryon Skims*

This analysis sought to identify charm baryon decays of different topologies and different final states. Some of the states included only charged tracks, while others involved the neutral Λ^0 baryon or the charged Ξ^- baryon. The idea behind a skim is to select events loosely and quickly from the morass of reconstructed data and direct

them into a collection of manageable size for in-depth analysis. The skim package consisted of a variety of subroutines designed to choose specific final states of different particles. Table 3.2 displays the lists of event selection strategies.

Since the decays considered in this thesis include the channels $\Lambda_c^+ \rightarrow pK^-\pi^+$, $\Lambda_c^+ \rightarrow \Lambda^0\pi^+\pi^-\pi^+$; the $\Xi_c^+ \rightarrow \Lambda^0 K^-\pi^+\pi^+$ and the $\Xi_c^+ \rightarrow \Xi^-\pi^+\pi^+$, three separate data skims were needed: the $pK^-\pi^+$ skim, the Λ^0 skim, and the Ξ^- skim, which corresponded to skimbits 16, 13, and 7 respectively.

3.3.1 The $\Lambda_c^+ \rightarrow pK^-\pi^+$ Skim

The $\Lambda_c^+ \rightarrow pK^-\pi^+$ skim selected combinations of three linked tracks in which each respective track possessed a Čerenkov identification consistent with being a proton, kaon, or pion. The candidate-driven vertexing algorithm refined the combinations by requiring the existence of primary and secondary vertices which passed loose quality cuts, and a relaxed significance of detachment (L/σ_L) cut. The details are as follows:

- ISTATP of the proton candidate track was 8 or 12;
- ISTATP of the kaon candidate track was 4, 12, or 7 (if $p_K > 60$ GeV/c) (This kaon identification is referred to as KP7);
- ISTATP of the pion candidate track was NOT equal to 1, 4, 8, or 12 (i.e., not electron definite and not heavy);
- The proton sign was equal to the pion sign; the proton and pion signs were opposite to the kaon sign;
- Confidence level of the primary vertex exceeded 1% ;
- Confidence level of the secondary vertex exceeded 0.01% ;

Table 3.2. List of Skimming Strategies

Skim Bit	Skim Goal
1	Semileptonic skim
2	1 % of all events
3	Prescaled Unbiased Data
4	e^+e^- pair trigger
5	Two vertex skim
6	
7	Ξ^-/Ω^- skim
8	K_s^0 skim
9	D meson skim
10	D meson skim (D^* flag set)
11	D meson skim (Golden Mode flag)
12	
13	Λ^0 skim
14	Kink ($\Sigma^\pm$) skim
15	Charm Baryon skim (Specific final states of Λ_c^+ and Ξ_c^+)
16	$\Lambda_c^+ \rightarrow pK^-\pi^+$ skim
17	Leptonic skim
18	μ skim for J/Ψ
19	Diffractive skim
20	
21	Topological skim 1
22	Topological skim 2
23	
24	
25	Kaon lepton skim
26	Kaon id skim
27	Kaon linking skim
28	ϕ^0 skim
29	prescaled bit 26
30	prescaled bit 27

- $L/\sigma_L > 1$;

and the invariant mass of the $pK^-\pi^+$ combination was required to be between 2.0 and 2.6 GeV. This skim selected about 6 million events for additional analysis.

3.3.2 Λ^0 Skim

Cleaner lambdas than those found by the vee reconstruction code were stripped for use in analyzing those charm baryon decays which contained a Λ^0 in the final state. This skim basically imposed Čerenkov identification cuts on the higher-momentum ("fast") charged daughter track of the lambda and simply accepted the Reconstruction vees and MIC vees as they were, imposing no additional cuts. Although the MIC vees were not used in the subsequent analysis, it was not known at the time of the skim that they contained problems and would later be excluded from consideration. The following Čerenkov cuts were placed on the "fast" track of the SSD and Magnet Region vees, along with some additional cuts for certain subcategories of the M1 vees:

- ISTATP = 8, 12, or 14 for $p < 20$ GeV/c ;
- ISTATP = 8 or 12 for 20 GeV/c $< p <$ 110 GeV/c ;
- ISTATP = 8, 12, 14, or 15 for $p > 110$ GeV/c ;
- DCA (Distance of Closest Approach) $<$ 5mm (Track-Track Λ^0 only) at the vee vertex;
- ISTATP $\neq$ 0 or 1 for the "slow" track for Track-Track vees which failed the fit;
- ISTATP $\neq$ 0 or 1 for the "slow" track for Stub-Stub vees whose stubs failed the refit;

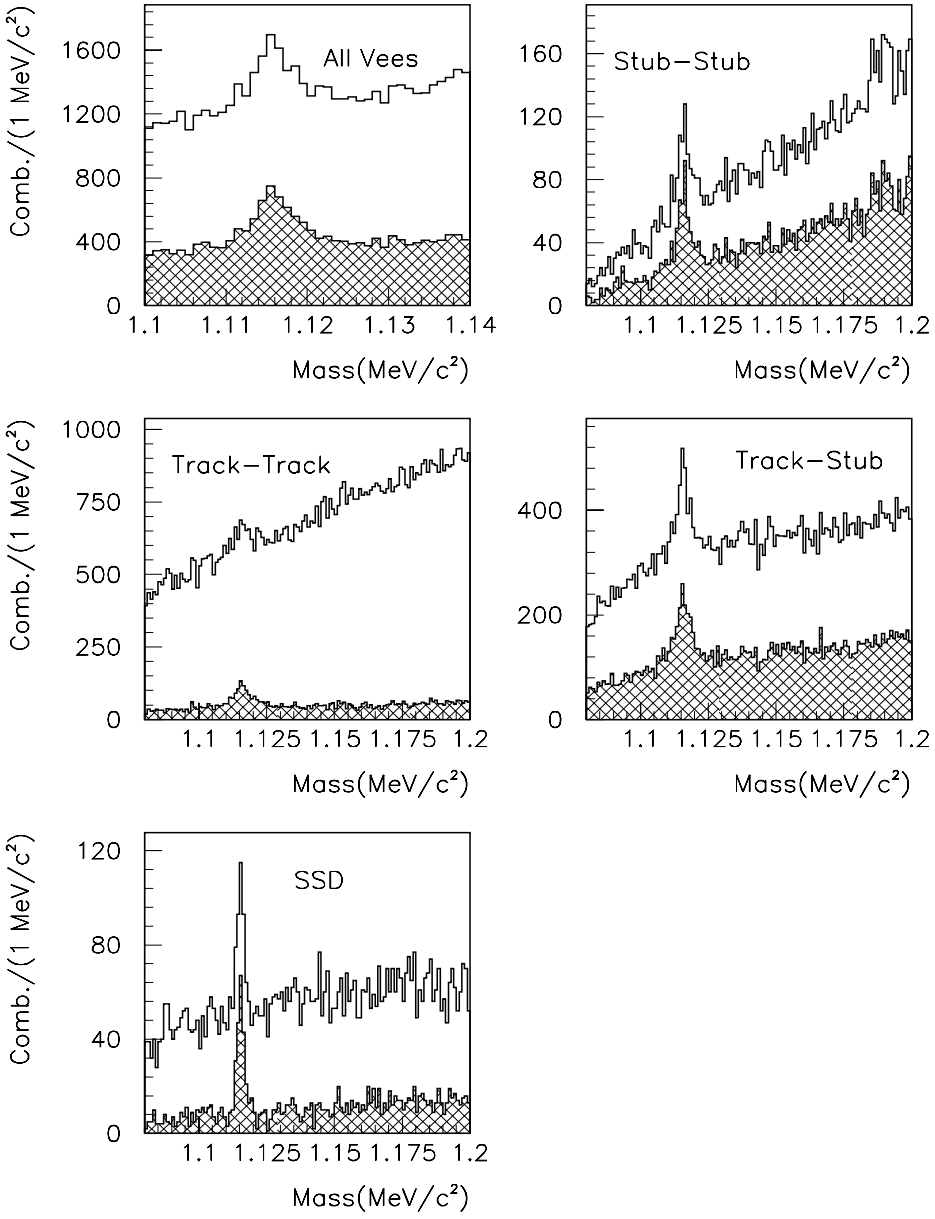

Figure 3.2. Invariant mass distributions of the raw lambdas overlaid on the skimmed lambdas for the SSD and M1 vee categories, as well as for the total lambda sample. The figure represents a small fraction of the 1990-91 data set, and displays the effectiveness of the lambda selection algorithm.

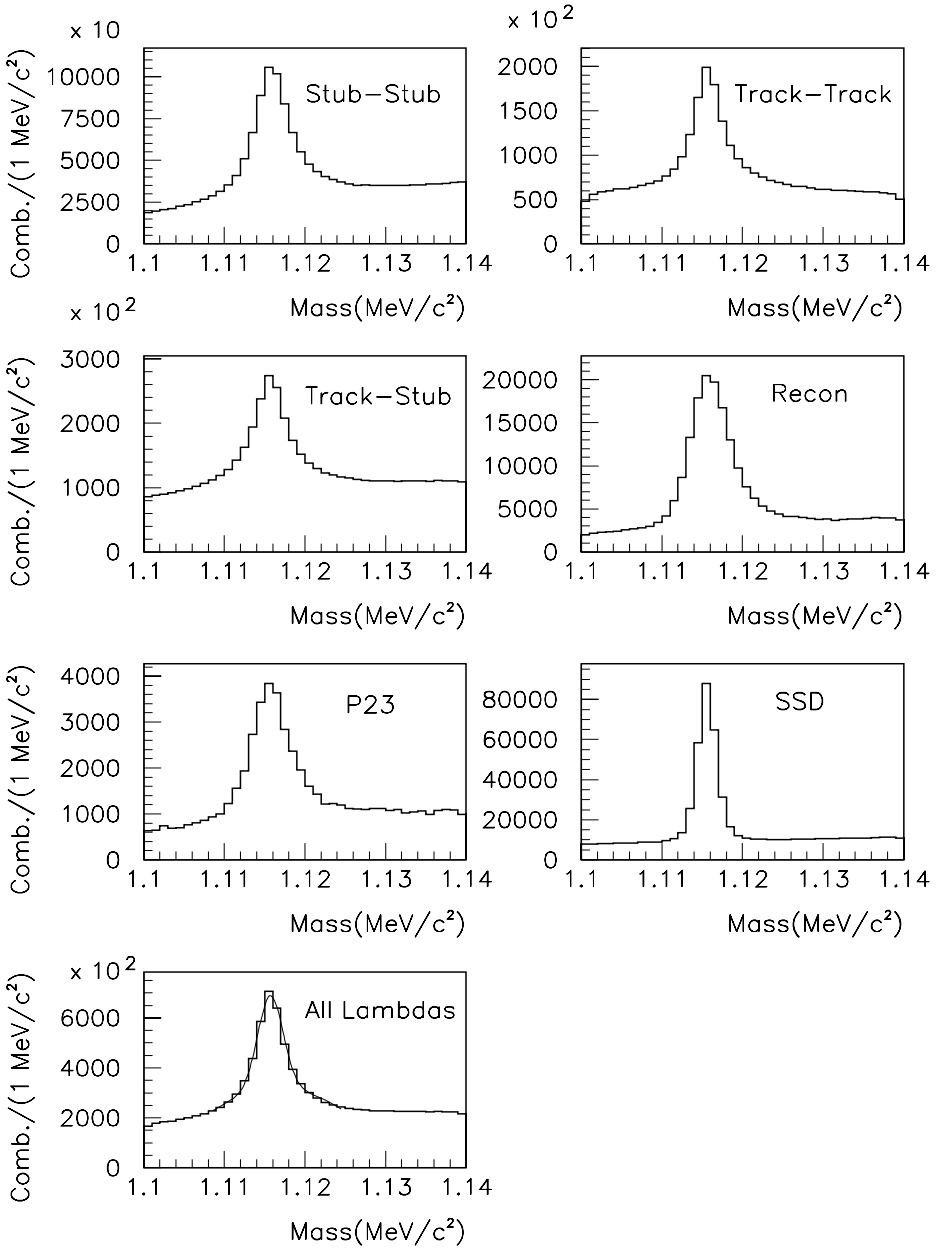

Figure 3.3. Invariant mass distributions of the skimmed lambdas from the entire 1990-91 data set.

and $1.10 < m_{p\pi^-} < 1.14$ GeV. The lambda skim selected approximately 11 million events to be further analyzed. Figure 3.2 illustrates the power of the lambda skim algorithm by comparing the invariant $p\pi^-$ masses before the skim cuts with those after the skim cuts. Lambdas from the entire 1990-91 data set are displayed in Figure 3.3 according to vee type, showing a total yield of over 3 million lambdas.

3.3.3 Ξ^-/Ω^- Skim

Although this skim reconstructed and selected both cascades and omegas, only the cascade aspect of it will be discussed here since the omegas were not used in this analysis. Having a mass of 1321.32 MeV/c^2 , the Ξ^- baryon possesses strangeness -2 (quark content is *ssd*) and decays weakly as $\Xi^- \rightarrow \Lambda^0\pi^-$ with branching fraction 100%. The E-687 experiment searched for the cascades in two ways. The first method utilized the candidate-driven vertexing approach described earlier (see Section 3.3.1) to find the cascades which decayed upstream of the microstrip system. These were dubbed "type one" cascades, and since they were not used in any of the E-687 analyses including this one, no further mention will be made of them. The second classification, the "type two" cascades, passed through the SSD detector and left charged tracks in this system before decaying, which greatly aided SDVERT in reconstructing all-charged final states containing these baryons. Therefore it is pertinent to discuss the algorithm which finds them.

First, a slightly modified version of the lambda skim code selected the lambdas to be used in finding the cascades; the only alterations included:

- An invariant mass cut of ± 15 MeV/c^2 around the nominal Λ^0 mass (± 8 MeV/c^2 for SSD vees).

- One-link vees were used in this skim whereas they were rejected in the lambda

skim. A "one-link" vee is one in which one of the vee's PWC daughter tracks linked to a microstrip track. These Λ^0 typically exhibited a small signal buried in a large background, but were responsible for reconstructing an amount of cascades which was not insignificant.

Once the good lambda candidate was selected, the "type two" routine found combinations of lambdas and charged unlinked PWC tracks [Dal 92]. The first step was to employ the intersection in the non-bend view of the vee and the unlinked track in order to determine the z-position of the Ξ^- decay vertex. The corresponding y decay position was found by tracing the track to this z coordinate; a new z was calculated using this information, and the process was iterated five times or until the z did not change by more than 0.3 cm. Once the z was determined, the algorithm endeavored to match unlinked SSD tracks (the hypothesized Ξ^- tracks) with the Ξ^- momentum vector which had been calculated using the momentum of the Λ^0 candidates and the momentum of the unlinked PWC tracks (the candidate π^-). A given microstrip track was traced to the y and z of the supposed Ξ^- decay, and two cuts were imposed to aid in finding a good match between the putative Ξ^- track and the reconstructed $\Lambda^0\pi^-$ momentum vector: (1) the DCA between the Ξ^- decay vertex as calculated from the candidate Λ^0 and the corresponding unlinked PWC track was required to be less than 1.2 cm, and (2) the differences in the x and y slopes predicted by the vee-track combination and the x and y slopes of the microstrip track were required to be less than 4 milliradians. Candidate cascades with a $\Lambda^0\pi^-$ invariant mass of less than 1.4 GeV/c^2 were skimmed. Figure 3.4 shows the 1990-91 type two cascade sample.

Once the skimming was completed, the in-depth analysis which attempted to expose the specific charm signals of interest was performed. This is discussed next.

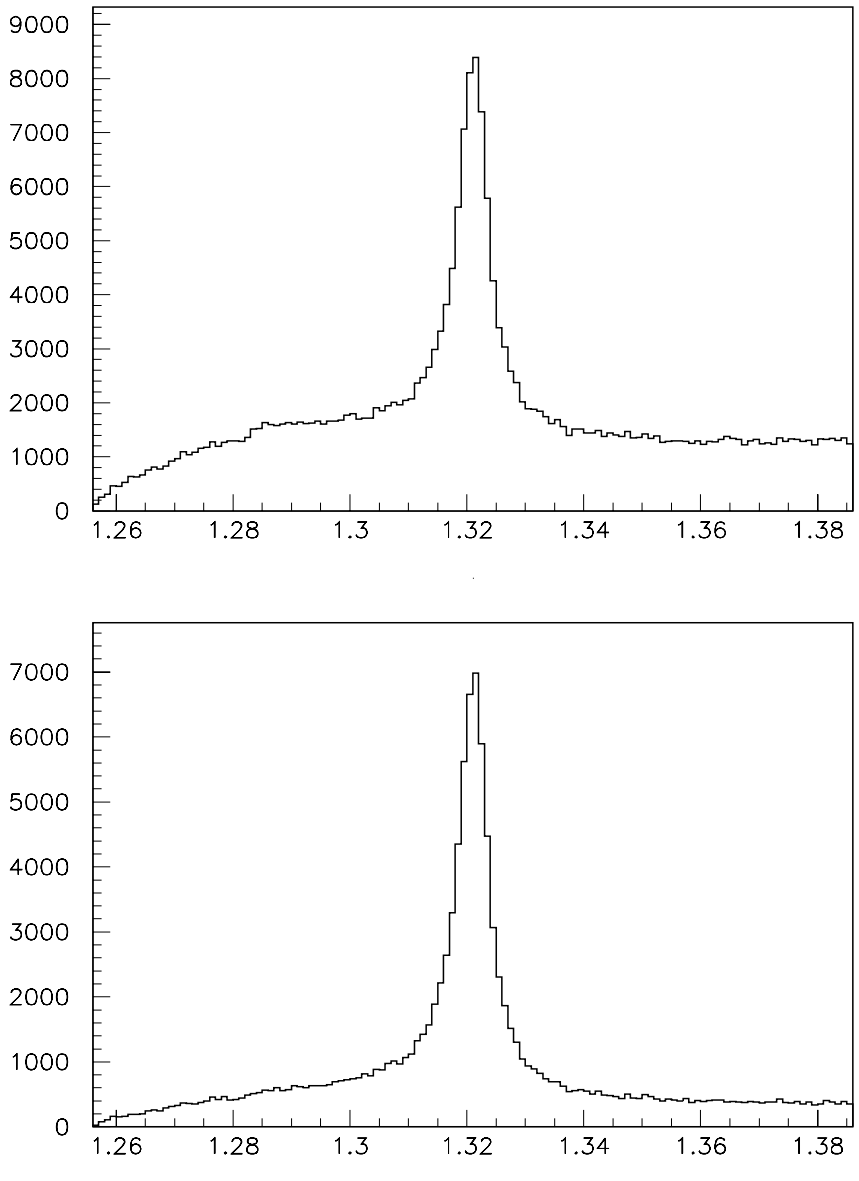

Figure 3.4. The E-687 1990-91 Ξ^- sample. The histograms display only those cascades which left tracks in the microstrip detector system; these "type two" cascades decayed downstream of the last SSD plane. The bottom plot shows the effect of tightening the constraint on the difference between x,y microstrip angles and x,y angles predicted by the vee-track combination.

CHAPTER 4

Search for the Charm Baryons

The goal of the branching ratio analysis is to measure the following relative decay rates: $B(\Lambda_c^+ \to \Lambda^0\pi^+\pi^-\pi^+)/B(\Lambda_c^+ \to pK^-\pi^+)$, and $B(\Xi_c^+ \to \Lambda^0 K^-\pi^+\pi^+)/B(\Xi_c^+ \to \Xi^-\pi^+\pi^+)$. The former has been measured and the latter has not. Indeed, only a few experiments have observed these specific charm baryon decays which involve lambdas due to the difficulties that this neutral vee poses when reconstructing final states. This chapter will be devoted to the presentation of the E-687 reconstructed signals of these states as well as to a discussion of the methodology employed.

Since the purpose of this chapter is to present the signals which E-687 has been able to produce, specific sets of cuts were chosen to achieve this end; these may or may not be the cuts which the subsequent branching ratio analysis utilizes. This is because one must perform careful systematic studies of the effects that the cuts have on the data and the Monte Carlo before choosing them to measure a branching ratio.

4.1 SUPERDVERT: A Reprise

The basic mechanics of exposing charm baryon signals have been discussed earlier in Section 3.3.1 of this work. To review, these are the formation of primary and secondary vertices and the imposition of an L/σ_L cut which, by requiring a significant vertex separation, typically removes a large fraction of the background. Čerenkov cuts

according to the ISTATP codes of the proton, kaon, and pion candidate tracks also play quite important roles in bringing out the signal, as do cuts on the quality or confidence levels (CL) of the primary vertex (labeled CLP) and the decay vertex (labeled CLD). The SUPERDVERT algorithm provides two more extremely useful tools for enhancing signal quality, and these are quite important for charm baryon work because charm baryons are more difficult to observe than charm mesons. The reasons include shorter lifetimes implying that isolating the decay vertex from the morass of charged particles which come from the primary is more arduous, and also the fact that charm baryons are produced at much lower rates than charm mesons, which means that one often looks for a small peak which rides a huge wave of combinatoric noise. These tools are the isolation cuts known as CL1 and CL2.

The CL1 cut refers to the situation in which one of the tracks from the decay vertex is consistent with originating from the primary vertex. The algorithm postulates that this is indeed the case and calculates a concomitant χ^2/DOF and confidence level according to this hypothesis. Since, if true, this situation is undesirable, one insists that CL1 be below a certain confidence level. The primary use of this cut applies to two body decay states because they usually possess a large amount of Q-value (defined as the energy released in a reaction) available to the daughters. This in turn implies that the daughter particles can emerge from the parent at significant angles, and that it is less likely that the daughter tracks will point to the primary vertex.

The CL2 cut attempts to isolate the charm vertex from all other tracks in the event which do not belong to the primary or secondary vertices. The CL2 algorithm works by taking each candidate track which does not originate from the primary or secondary vertex and combines it with the tracks which are assigned to the secondary vertex. The method then forms a new vertex, calculates a corresponding χ^2/DOF , and determines a confidence level that the additional track emerged from the charm

vertex. The scheme repeats the process for the other tracks in the event and assigns CL2 the largest confidence level computed. As with the CL1 cut, one insists that CL2 be less than a certain value. This cut serves to eliminate background in higher multiplicity decays where CL1 is less effective. One subjects the particular state of interest to the extraction tools discussed above to eliminate background and isolate signals. Each of the charm baryon decays will now be examined in some detail according to this candidate driven vertexing algorithm, commencing with the easiest state to reconstruct which is also the most abundant.

4.2 The $\Lambda_c^+ \to pK^-\pi^+$ Sample

Since this is the simplest state to analyze and is by far the most copious of the charm baryon decays, it will be discussed first. In order to reveal the $pK^-\pi^+$ signal, the skim cuts had to be tightened somewhat. This included improving the decay vertex quality, increasing the significance of detachment quantity L/σ_L , restricting the Čerenkov identities of the candidate tracks, and levying the CL1 and CL2 cuts on the vertices. All these conditions are listed in Table 4.1, and signals for various values of L/σ_L are shown in Figure 4.1. The condition mandating that combinations containing a proton of ISTATP twelve and a kaon of ISTATP twelve be excluded is justified in Figure 4.2; this subset of combinations exhibits some signal but the accompanying background dwarfs it. Also, such combinations are prone to be misidentified D_s^+ or D^+ decaying to $K^+K^-\pi^+$. The resulting $\Lambda_c^+ \to pK^-\pi^+$ yields are excellent and represent the largest fixed target sample in the world at this time. It is worthwhile to illustrate the power of the vertexing and isolation cuts because one can achieve excellent signal-to-noise in the $pK^-\pi^+$ channel by tightening CLD, CL1, and CL2 one at a time, or by tightening them in combination. Figure 4.3 displays this. The evidence of such clean signals furnishes one with the opportunity to hunt

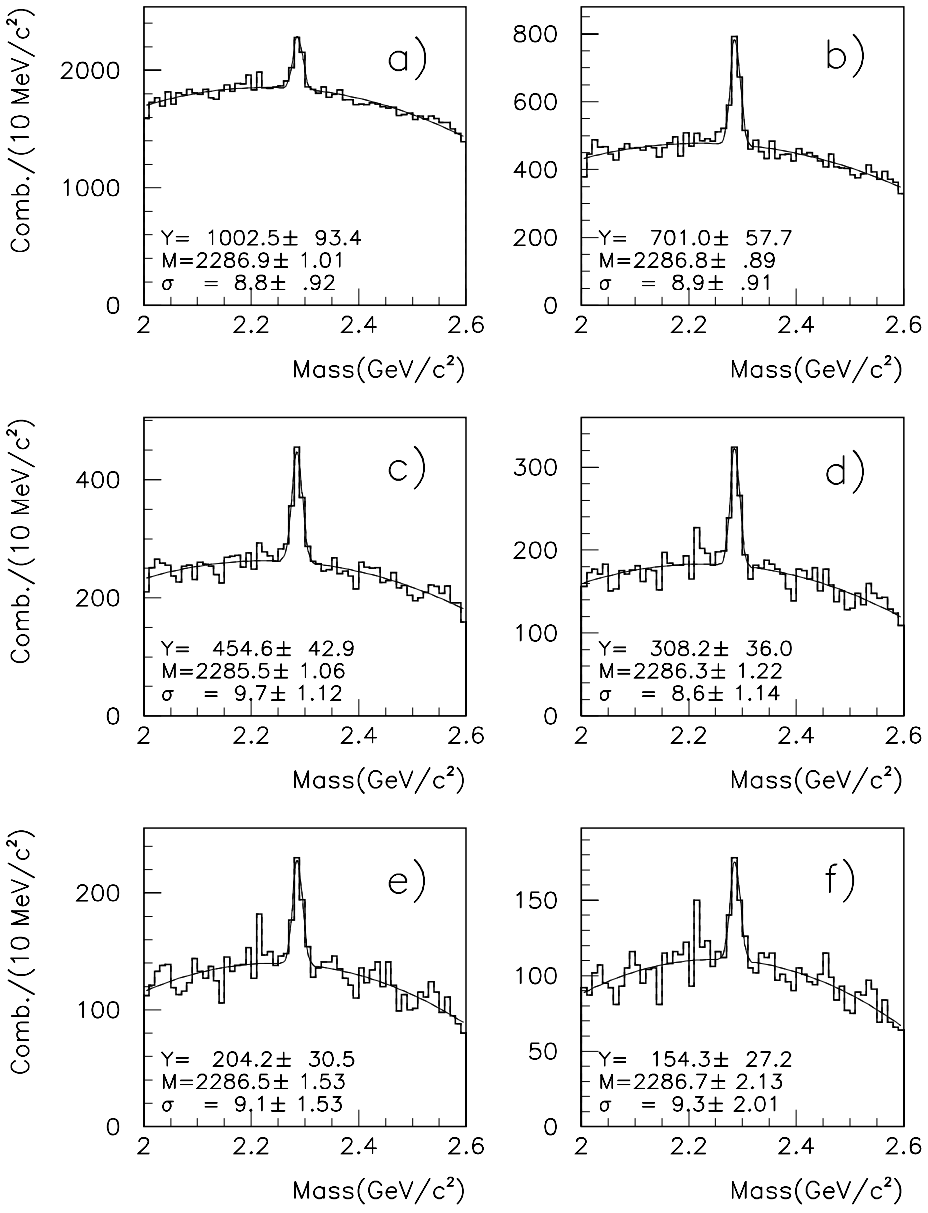

Figure 4.1. Invariant mass distributions of the $pK^-\pi^+$ channel for cuts described in the text and for various L/σ_L requirements: a) $L/\sigma_L > 3$, b) $L/\sigma_L > 5$, c) $L/\sigma_L > 7$, d) $L/\sigma_L > 9$, e) $L/\sigma_L > 11$, f) $L/\sigma_L > 13$.

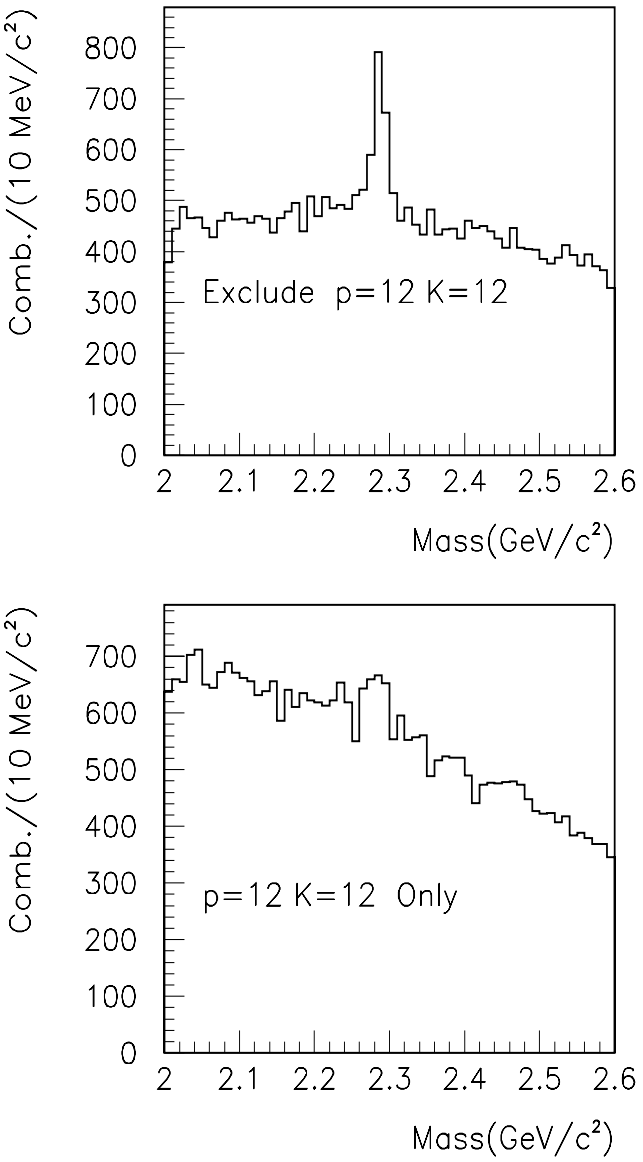

Figure 4.2. Invariant mass distributions of the $pK^-\pi^+$ channel for $L/\sigma_L > 5$ and with cuts described in the text for different Čerenkov combinations of the proton and kaon.

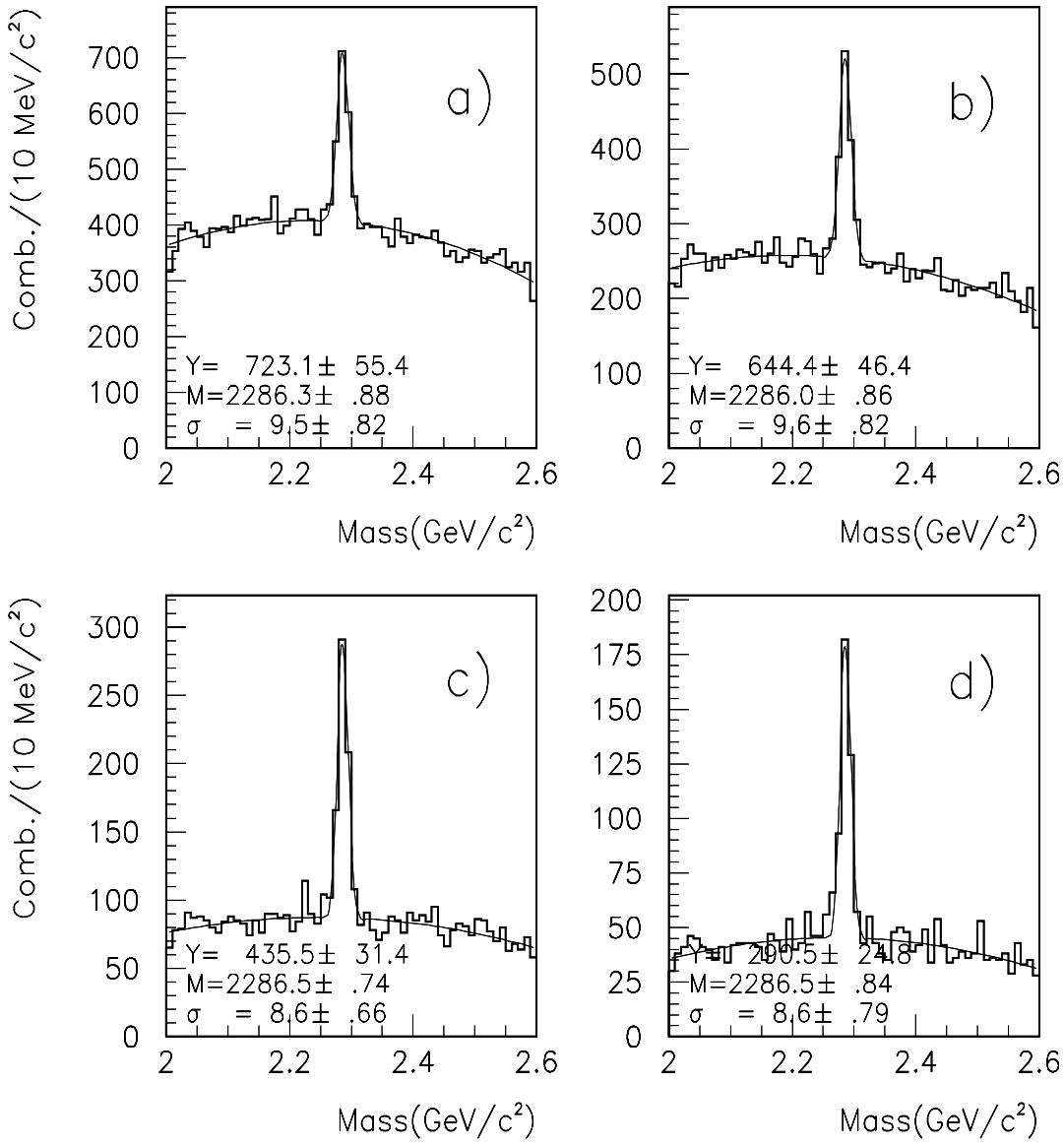

Figure 4.3. Invariant mass distributions of the $pK^-\pi^+$ channel for $L/\sigma_L > 6$ and various values of CLD, CL1, and CL2. One can achieve clean signals by utilizing these in combination: a) CLD > .01, b) CLD > .05, c) CLD > .05, CL2 < .0001, d) CLD > .05, CL2 < .0001, and CL1 < .3.

Table 4.1. Cuts used to obtain the $\Lambda_c^+ \to pK^-\pi^+$ signals

Requirement	Requirement Value
Linking between the PWC and SSD Candidate Tracks	Yes
Proton ID	ISTATP = 8 or 12
Kaon ID	KP7 ($\neq$ 12 if Proton = 12)
Pion ID	ISTATP $\neq 1, 4, 8, 12$
L/σ_L	$> 3, ..., > 13$
Confidence Level of the Primary Vertex	> 1 %
Confidence Level of the Charm Vertex	> 1 %
CL1	< 0.8
CL2	< 0.05

for resonance substructure in this particular final state; namely, the $p\overline{K^{*0}}(892)$, the $\Delta^{++}(1232)K^-$, and the $\Lambda^*(1520)\pi^+$. A narrow region around the $\Lambda_c^+ \to pK^-\pi^+$ mass peak of 2286.5 ± 8.5 MeV/c^2 was selected and utilized to look for evidence of these substates. Figure 4.4 manifests the invariant masses of the respective subchannels and reveals the $p\overline{K^{*0}}(892)$ as the only tangible contribution to the $pK^-\pi^+$ final state, while Figure 4.5 indicates that the $\overline{K^*}^0(892)$ peak does seem to come from the $\Lambda_c^+ \to p\overline{K^{*0}}(892)$ decay and not from background. The low and high sidebands encompassed $pK^-\pi^+$ mass regions from 2.223-2.240 GeV/c^2 and 2.333-2.350 GeV/c^2 , respectively. While the $\Delta^{++}(1232)$ and $\Lambda^*(1520)$ states will not be pursued further in this dissertation, a quick and simple examination proves interesting. The presence of the $p\overline{K^{*0}}(892)$ state indicates a possible W-exchange contribution to the $pK^-\pi^+$ final state, but the other available W-exchange mechanisms $\Lambda_c^+ \to \Delta^{++}(1232)K^-$ and $\Lambda_c^+ \to \Lambda^*(1520)\pi^+$ seem to be suppressed.

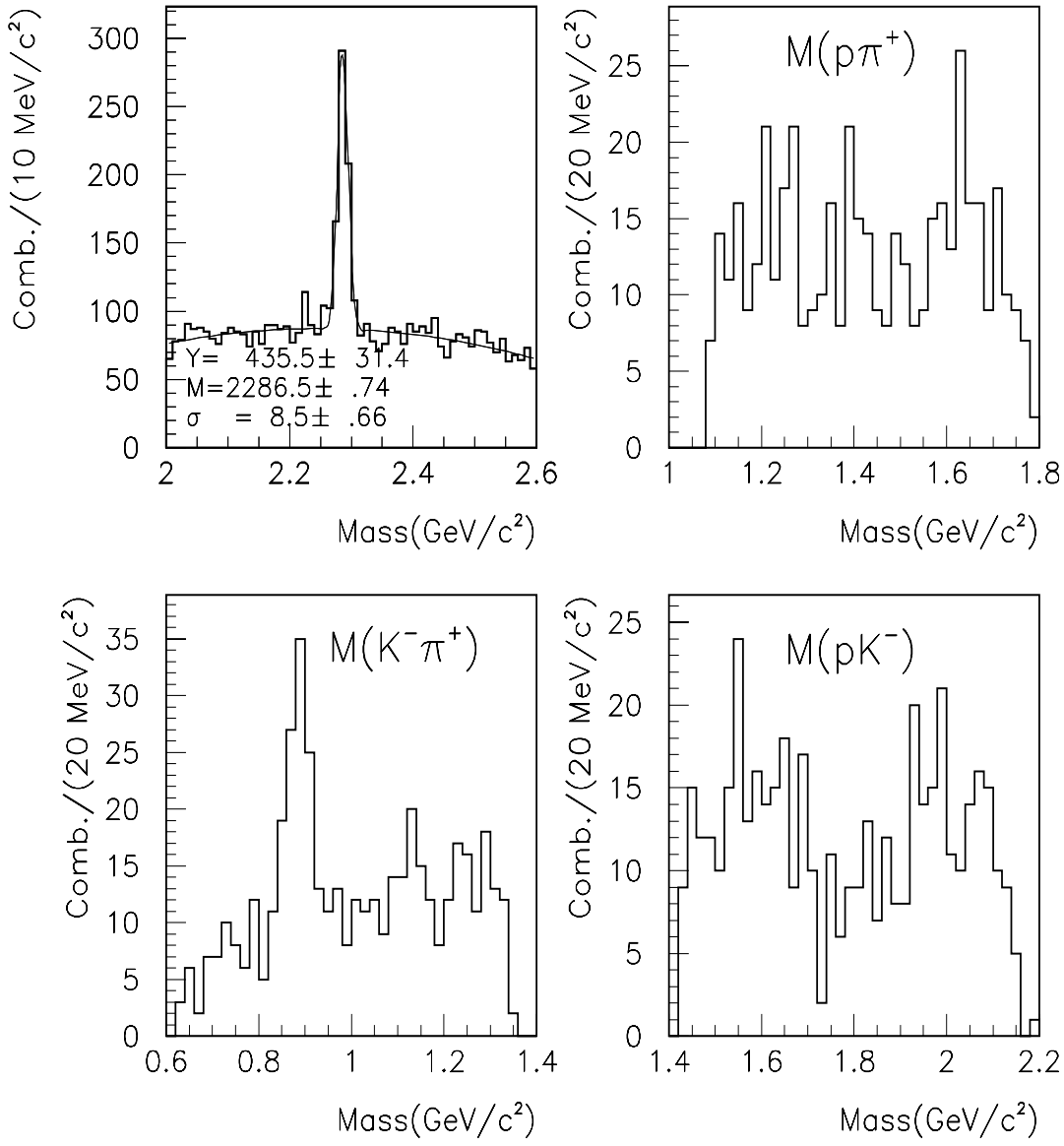

Figure 4.4. Invariant mass distributions of the $pK^-\pi^+$ channel and the corresponding $p\pi^+$, $K^-\pi^+$, and pK^- substates. The $\overline{K^{*}}^{0}(892)$ dominates.

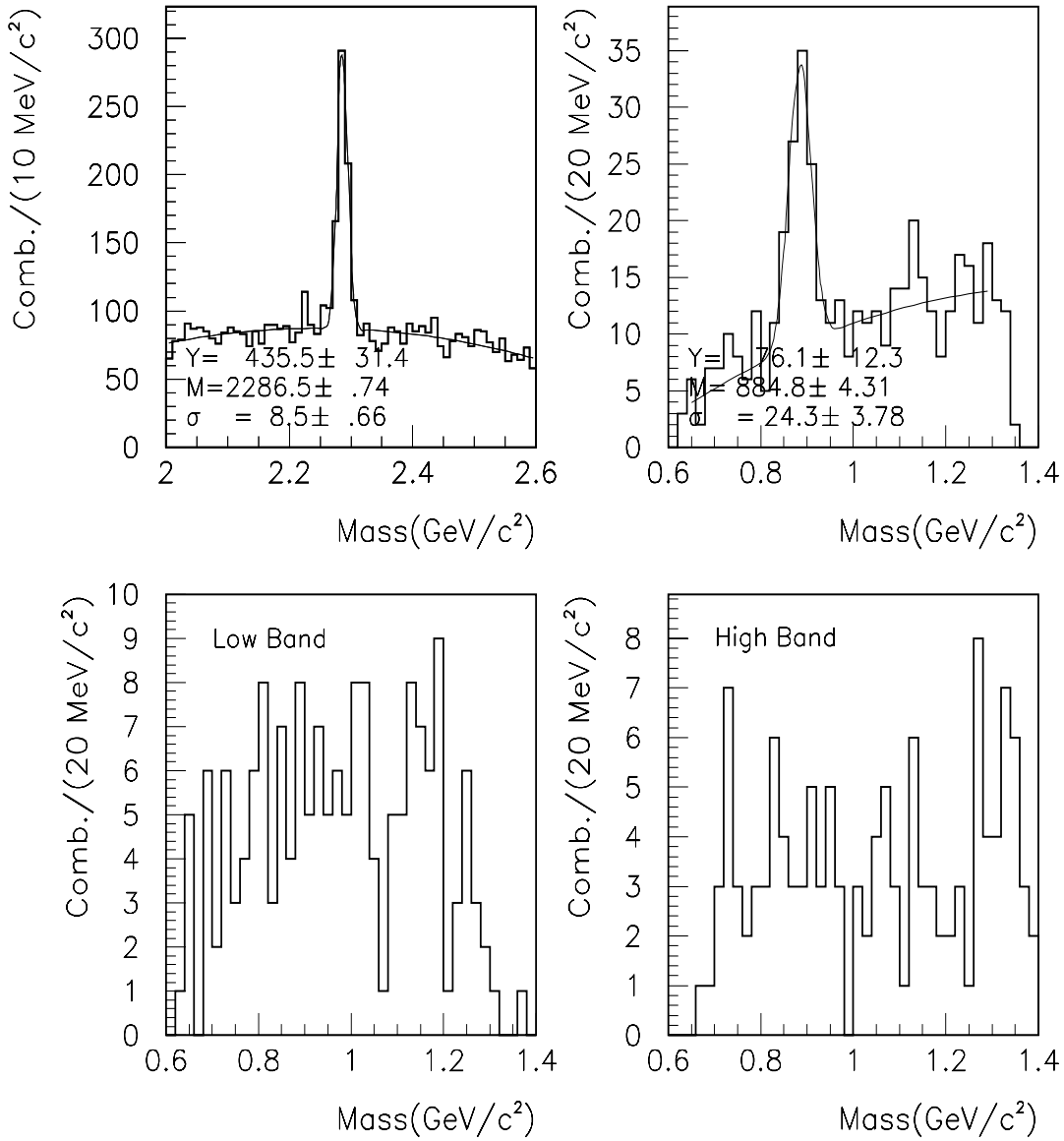

Figure 4.5. Invariant mass distributions of the $pK^-\pi^+$ channel and the corresponding $K^-\pi^+$ substate for the Λ_c^+ signal region, low sideband, and high sideband regions as described in the text.

4.3 *The* $\Lambda_c^+ \rightarrow \Lambda^0\pi^+\pi^-\pi^+$ *Sample*

One studies and develops the $\Lambda^0\pi^+\pi^-\pi^+$ state in the same way that one exposes the $pK^-\pi^+$ state, by using the candidate driven vertex method. The presence of the vee complicates things somewhat since it cannot contribute to the vertex construction due to its invisiblity in the spectrometer. The lambdas have a lifetime on the order of 10^{-10} seconds and may travel several meters through the detector before decaying to $p\pi^-$. Except for the SSD vees which constitute only 10% of the entire lambda data set, no microstrip hit information is available from the vee daughters to reconstruct SSD tracks which SDVERT requires to calculate vertex positions. For the 90% of vees which decay downstream of the microstrips, the momentum of the lambda determined from momenta of its constituent proton and pion tracks could conceivably be used in the $\Lambda^0\pi^+\pi^-\pi^+$ secondary vertex determination, but this is inadvisable. The proton and pion tracks only pass through the PWC stations, and the PWC position resolution, while good, does not compare to the excellent microstrip resolution needed for high quality precision vertexing. As for the SSD vees which do use the microstrip information to reconstruct the proton and pion tracks, the vees themselves still leave no observable hits and consequently produce no tracks which would directly lead to the secondary vertex. Therefore, the vertexing scheme does not use the lambda to determine the location of the decay vertex, but uses the three pion tracks instead.[1] The momentum of the lambda is utilized in seeding the primary vertex, however.

One then imposes the CLP, CLD, CL1, CL2 and Čerenkov cuts on the pion candidate tracks to isolate the signal. Lambda candidates were required to satisfy the conditions enumerated in Section 3.3.2, along with the additional criteria that the lambda mass be within ± 10 MeV/c^2 of the nominal lambda mass of 1115.63 MeV/c^2 ,

[1] The vee is assigned large positional errors so that the three pions determine the vertex location.

Table 4.2. Cuts used to obtain the $\Lambda_c^+ \rightarrow \Lambda^0\pi^+\pi^-\pi^+$ signals

Requirement	Requirement Value
Linking between the PWC and SSD Candidate Tracks	Yes
Mass cut on Λ^0 Candidate	1115.63 ± 10 MeV/c^2
Pion ID	ISTATP $\neq 1, 4, 8, 12$
L/σ_L	$> 3, ..., > 13$
Confidence Level of the Primary Vertex	> 1 %
Confidence Level of the Charm Vertex	> 1 %
CL1	< 0.8
CL2	< 0.05

and that the lambda candidate not be a type eight MICVEE. Table 4.2 summarizes the specific cuts which produced the $\Lambda_c^+ \rightarrow \Lambda^0\pi^+\pi^-\pi^+$ signal, and Figure 4.6 displays the signals in this channel for different values of L/σ_L . As with the $pK^-\pi^+$ final state, tightening the vertex cuts in tandem produces cleaner $\Lambda^0\pi^+\pi^-\pi^+$ signals as illustrated in Figure 4.7. One must be careful not to cut too tightly on CL1 because this is a four body final state. An increased likelihood exists that one of the daughter tracks is collinear with the seed track resulting in confusion with the primary and loss of signal. The E-687 $\Lambda_c^+ \rightarrow \Lambda^0\pi^+\pi^-\pi^+$ sample compares well to that of CLEO and surpasses those of the other experiments where statistics and quality are concerned.

4.4 Search for $\Xi_c^+ \rightarrow \Lambda^0 K^-\pi^+\pi^+$

Seeking the $\Xi_c^+ \rightarrow \Lambda^0 K^-\pi^+\pi^+$ decay affords one with a great opportunity to observe a rare channel, but also presents a difficult challenge. The Ξ_c^+ is not easy to find in the first place since it is not produced with great frequency, even compared

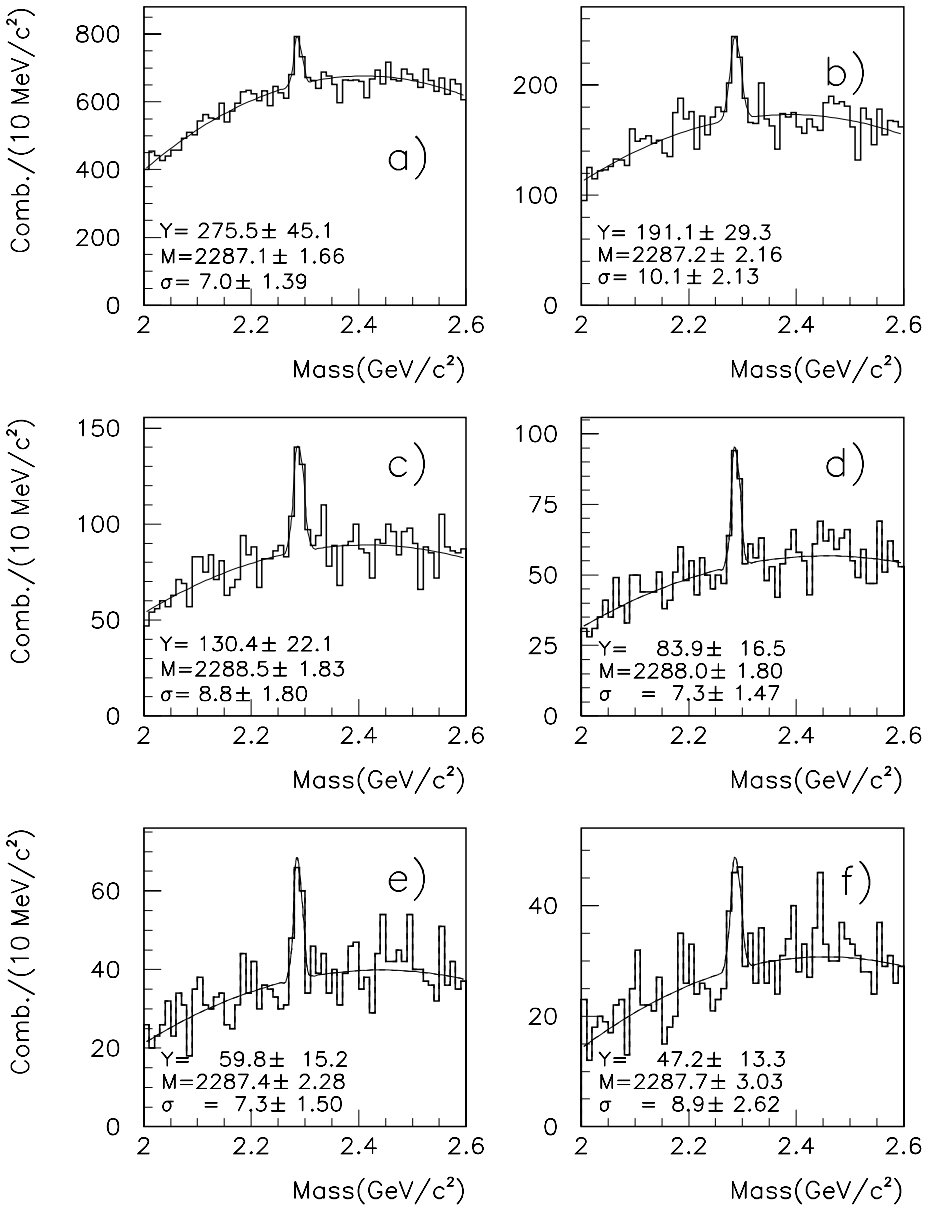

Figure 4.6. Invariant mass distributions of the $\Lambda^0\pi^+\pi^-\pi^+$ channel using the cuts described in the text and for various L/σ_L requirements: a) $L/\sigma_L > 3$, b) $L/\sigma_L > 5$, c) $L/\sigma_L > 7$, d) $L/\sigma_L > 9$, e) $L/\sigma_L > 11$, f) $L/\sigma_L > 13$.

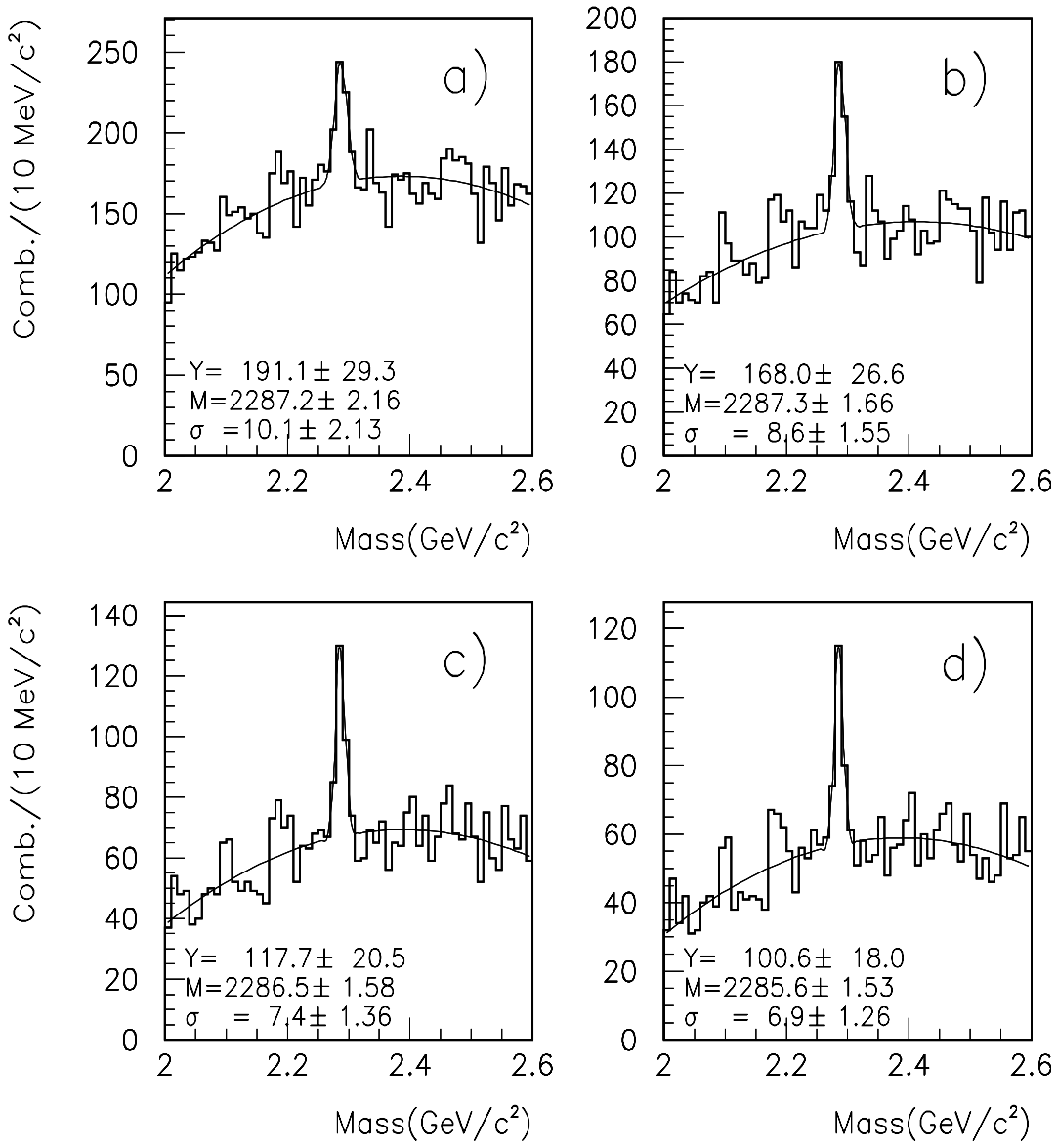

Figure 4.7. Invariant mass distributions of the $\Lambda^0\pi^+\pi^-\pi^+$ channel for various values of CLD, CL1, and CL2: a) CLD $>$ .01, CL1 $<$ .8, CL2 $<$ .05, b) CLD $>$ .05, CL1 $<$ .8, CL2 $<$ .05, c) CLD $>$ .05, CL1 $<$ .8, CL2 $<$ .001, and d) CLD $>$ .05, CL1 $<$ .6, CL2 $<$ .001.

Table 4.3. Cuts used on the $\Lambda^0 K^- \pi^+ \pi^+$ sample

Requirement	Requirement Value
Linking between the PWC and SSD Candidate Tracks	Yes
Mass cut on Λ^0 Candidate	1115.63 ± 10 MeV/c^2 (Clean Lambdas Used)
Kaon ID	KP7
Pion ID	ISTATP $\neq 1, 4, 8, 12$
L/σ_L	$> 2, ..., > 5$
Confidence Level of the Primary Vertex	> 5 %
Confidence Level of the Charm Vertex	> 5 %
CL1	Not Used
CL2	Not Used

to the Λ_c^+ . In addition to the small production cross section, many false $\Lambda^0 K^- \pi^+ \pi^+$ combinations can wash away the true (and limited) signal. Making stricter cuts on the lambda sample serves as a starting point to assist in suppressing the combinatoric background; one selects cleaner lambdas by excluding M1 vees which fail the fitting procedure described earlier in Section 3.1.3. This cleaner lambda sample (illustrated in Figure 4.8) was not used when reconstructing the $\Lambda_c^+ \rightarrow \Lambda^0 \pi^+ \pi^- \pi^+$ final state because it was not needed since the $\Lambda_c^+ \rightarrow \Lambda^0 \pi^+ \pi^- \pi^+$ signals were already evident. Table 4.3 lists the rest of the cuts which served to reveal a signal, and Figure 4.9 displays invariant mass plots of the $\Lambda^0 K^- \pi^+ \pi^+$ final state. A peak becomes visible at $L/\sigma_L > 3$ and its quality improves as the value of L/σ_L increases. The good statistical significance of the fitted peak (≈ 3 standard deviations at $L/\sigma_L > 4$, for example) suggests that the phenomenon may not arise from a statistical fluctuation. The only problem is that the mass of the fitted peak lies about 20 MeV/c^2 below the

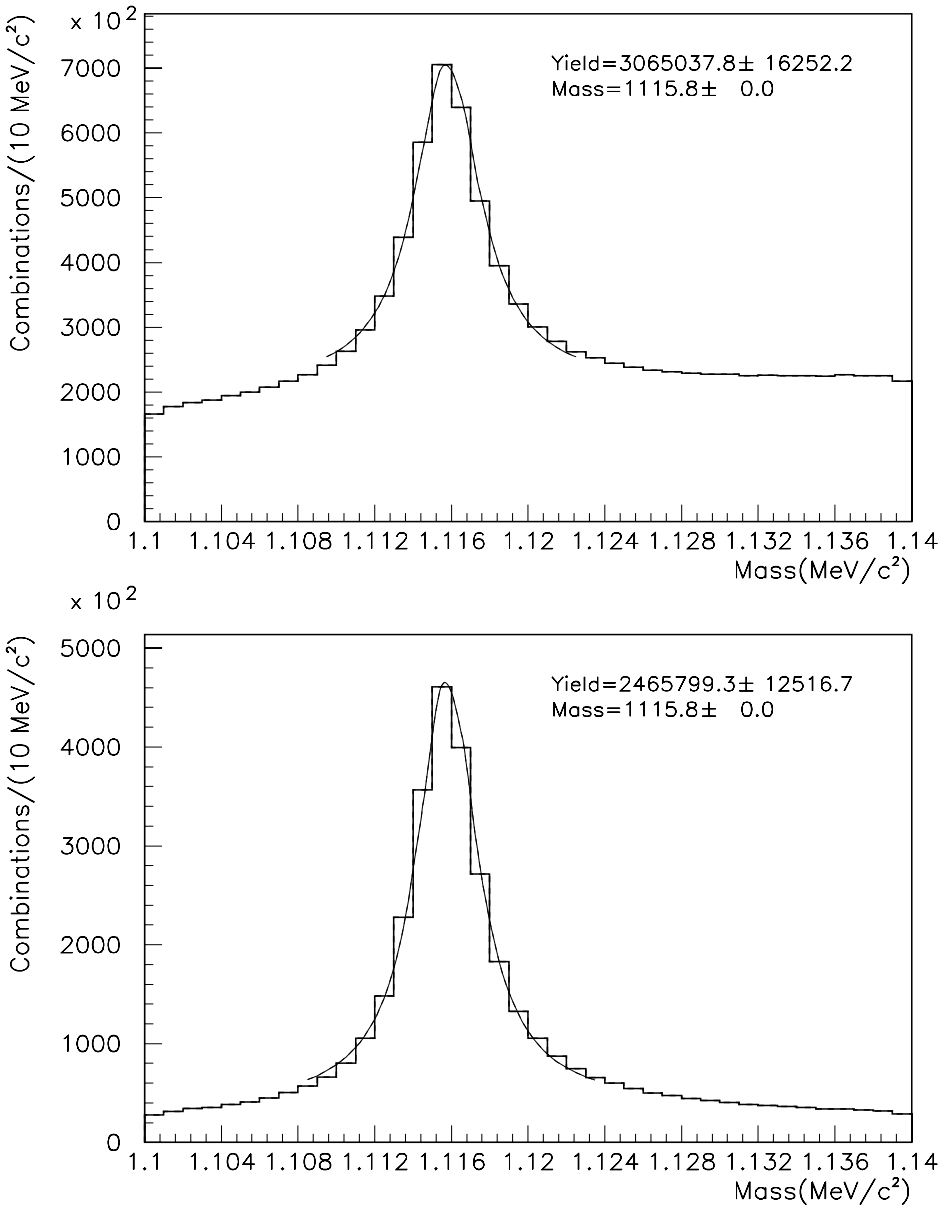

Figure 4.8. The exclusion of M1 region lambdas which fail the fitting procedure described in Section 3.1.3 improves the signal-to-background ratio.

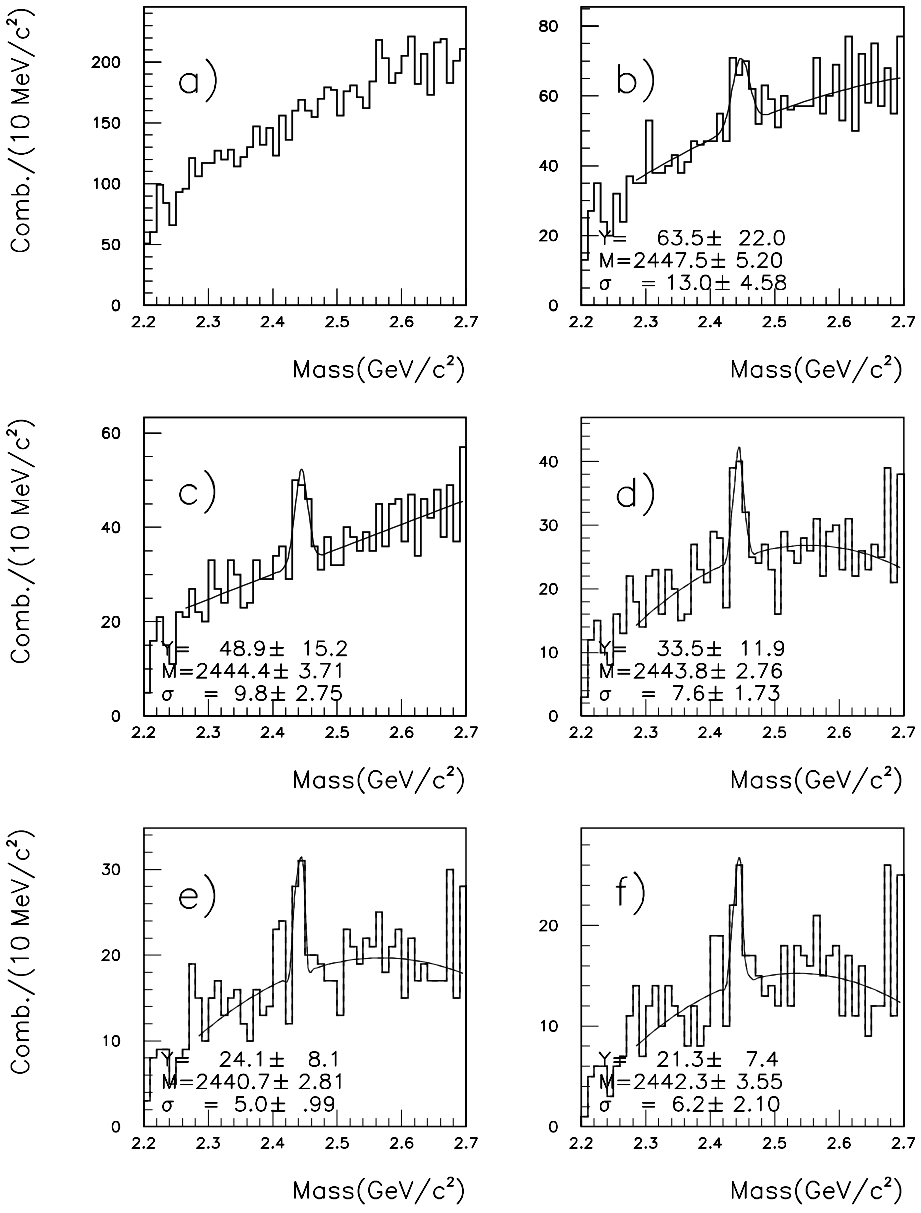

Figure 4.9. Invariant mass distributions of the $\Lambda^0 K^- \pi^+ \pi^+$ channel using the cuts described in the text and for various L/σ_L requirements: a) $L/\sigma_L > 2$, b) $L/\sigma_L > 3$, c) $L/\sigma_L > 3.5$, d) $L/\sigma_L > 4$, e) $L/\sigma_L > 4.5$, f) $L/\sigma_L > 5$.

currently accepted Ξ_c^+ mass of 2465.1 MeV/c^2 [PDG 94].

4.4.1 $\Lambda_c^+ \to \Lambda^0\pi^+\pi^-\pi^+$ *Contamination*

A possible explanation for this peak could be that it does not arise from a Ξ_c^+ decay, but from a reflection of the $\Lambda_c^+ \to \Lambda^0\pi^+\pi^-\pi^+$ channel. The term "reflection" refers to the situation where one or more of the particles in the final state suffers a misidentification by the Čerenkov system; in this case, it is possible that the kaon is really a pion. In order to determine if this particle has in fact been misidentified, one assigns this candidate kaon track the pion mass and creates an invariant mass plot. A peak in this misidentified $\Lambda^0\pi^-\pi^+\pi^+$ histogram might suggest $\Lambda^0\pi^-\pi^+\pi^+$ contamination of the $\Lambda^0K^-\pi^+\pi^+$ state. One then replots the $\Lambda^0K^-\pi^+\pi^+$ channel excluding the Λ_c^+ mass region from the $\Lambda^0\pi^-\pi^+\pi^+$ misidentification plot to determine how much, if any, signal is lost. One performs the same study on Monte Carlo samples in order to ascertain whether the signal loss in the data is compatible within errors with the signal loss in the Monte Carlo. If so, then the interpretation of the $\Lambda^0K^-\pi^+\pi^+$ peak as a $\Lambda^0\pi^-\pi^+\pi^+$ reflection would seem to be erroneous.

Figure 4.10 depicts the results of such a study, showing the $\Lambda^0K^-\pi^+\pi^+$ invariant mass for $L/\sigma_L > 4$, the $\Lambda^0\pi^-\pi^+\pi^+$ misidentification plot, and the effect of eliminating misidentified $\Lambda^0\pi^+\pi^-\pi^+$ combinations which fall into the Λ_c^+ signal region (2285 ± 15 MeV/c^2). One notes that no $\Lambda_c^+ \to \Lambda^0\pi^+\pi^-\pi^+$ misidentification peak emerges, and that the $\Lambda^0K^-\pi^+\pi^+$ signal falls by 19% when entries are removed from the Λ_c^+ signal region in the reflection plot. However, a Monte Carlo study demonstrates that if one assigns the kaon the pion mass, plots the resulting invariant mass, and excludes combinations which lie in the Λ_c^+ mass region (of course, these combinations do not come from a Λ_c^+ since the Monte Carlo generates only the $\Xi_c^+ \to \Lambda^0K^-\pi^+\pi^+$ channel),

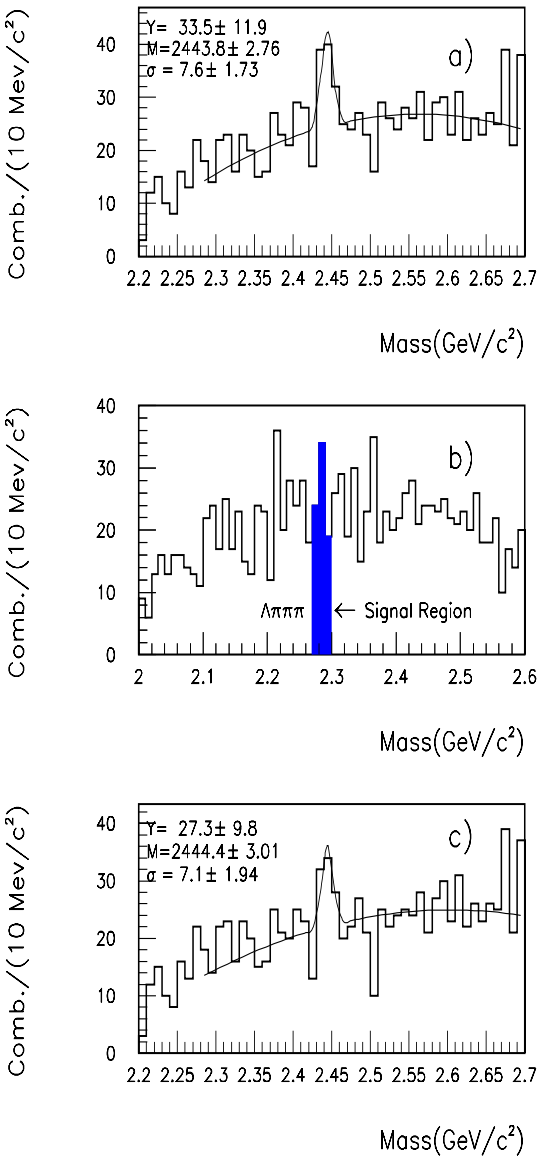

Figure 4.10. Invariant mass distributions of $(L/\sigma_L > 4)$: a) the $\Lambda^0 K^- \pi^+ \pi^+$ channel , b) $\Lambda^0 K^+ \pi^+ \pi^-$ plotted as misidentified $\Lambda^0 \pi^- \pi^+ \pi^+$, and c) the same state as a) except that the Λ_c^+ mass region in b) has been excluded.

the $\Xi_c^+ \rightarrow \Lambda^0 K^- \pi^+ \pi^+$ signal decreases by 15%, a reduction which is within the errors which arise from the fits to the data. Therefore, the interpretation of this $\Lambda^0 K^- \pi^+ \pi^+$ peak as a $\Lambda_c^+ \rightarrow \Lambda^0 \pi^+ \pi^- \pi^+$ reflection seems unlikely to be correct.

4.4.2 Wrong-Sign $\Lambda^0 K^+ \pi^+ \pi^-$ Study

Another way to test the degree to which the $\Lambda_c^+ \rightarrow \Lambda^0 \pi^+ \pi^- \pi^+$ state influences the $\Lambda^0 K^- \pi^+ \pi^+$ peak is to construct the wrong-sign $\Lambda^0 K^+ \pi^+ \pi^-$ invariant mass. Here, the "wrong-sign" nomenclature alludes to the fact that the Ξ_c^+ cannot decay into this final state due to strangeness conservation rules. If the $\Lambda_c^+ \rightarrow \Lambda^0 \pi^+ \pi^- \pi^+$ state is indeed responsible for the $\Lambda^0 K^- \pi^+ \pi^+$ peak due to a Čerenkov misidentification of the pion as a kaon, then the same misidentification might occur when viewing the $\Lambda^0 K^+ \pi^+ \pi^-$ state: what appears to be a K^+ would actually be a π^+, and a signal similar to that in the $\Lambda^0 K^- \pi^+ \pi^+$ channel should appear in the $\Lambda^0 K^+ \pi^+ \pi^-$ channel. Figure 4.11 exhibits the outcome of such a study, which seems to preclude the possibility of the $\Lambda^0 K^- \pi^+ \pi^+$ peak arising as the result of misidentified $\Lambda_c^+ \rightarrow \Lambda^0 \pi^+ \pi^- \pi^+$ since no peaks are evident in this wrong-sign channel. However, although this wrong-sign study and the previous reflection study seem to have ruled out any $\Lambda_c^+ \rightarrow \Lambda^0 \pi^+ \pi^- \pi^+$ misidentification, the $\Lambda^0 K^- \pi^+ \pi^+$ mass peak at 2444 MeV/c^2 does not agree with the currently accepted mass of the Ξ_c^+ .

4.4.3 $D_s^+ \rightarrow K_s^0 K^- \pi^+ \pi^+$, $D^+ \rightarrow K_s^0 K^- \pi^+ \pi^+$, and $D^+ \rightarrow K_s^0 \pi^- \pi^+ \pi^+$ Contaminations

Other possible misidentification candidates for the $\Xi_c^+ \rightarrow \Lambda^0 K^- \pi^+ \pi^+$ decay include the $K_s^0 K^- \pi^+ \pi^+$ final state from Cabibbo-favored D_s^+ decays and from Cabibbo-suppressed D^+ decays; and the $K_s^0 \pi^- \pi^+ \pi^+$ final state from Cabibbo-favored decays

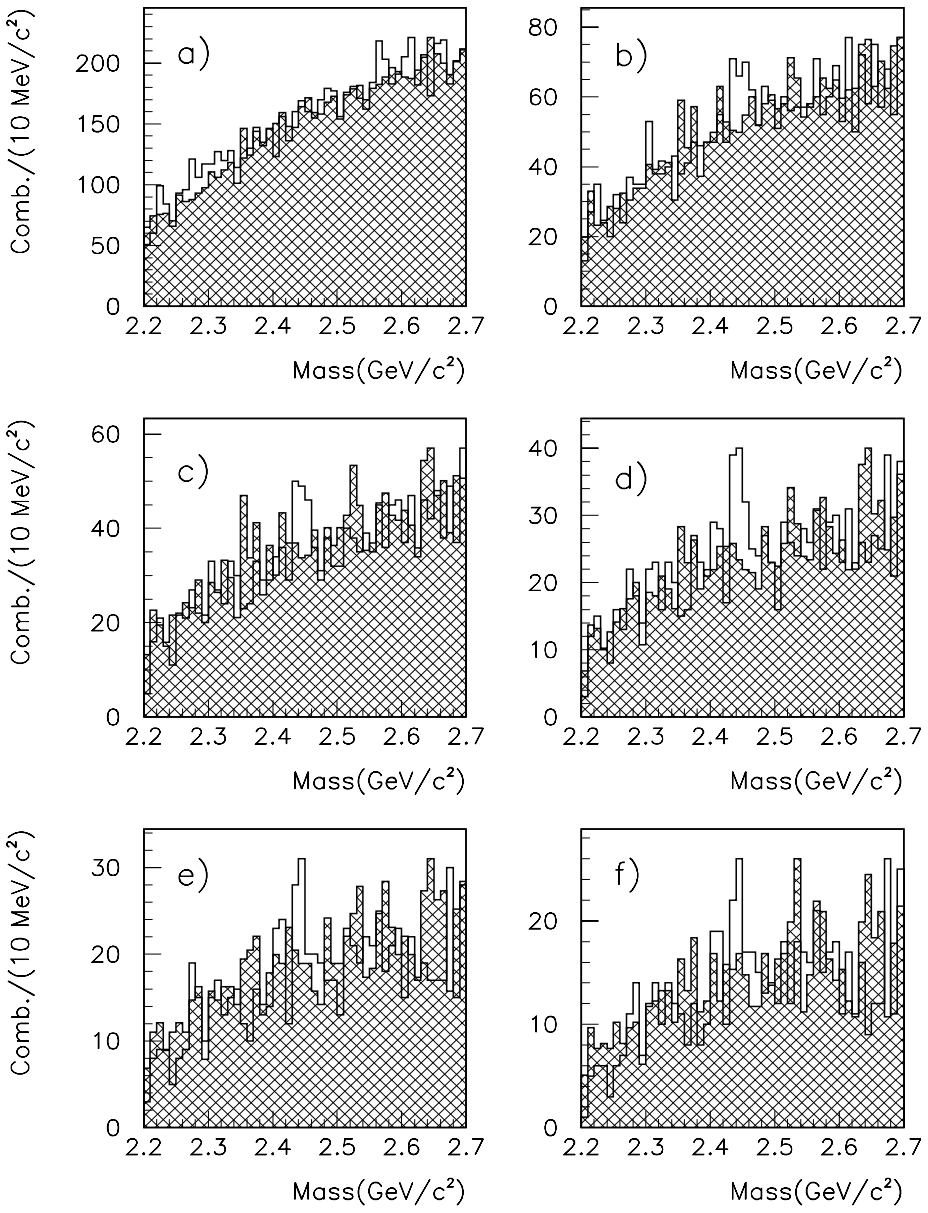

Figure 4.11. Invariant mass distributions of the wrong-sign $\Lambda^0 K^+\pi^+\pi^-$ channel (shaded) superimposed on the correct sign $\Lambda^0 K^-\pi^+\pi^+$ state for various values of the L/σ_L cut: a) $L/\sigma_L > 2$, b) $L/\sigma_L > 3$, c) $L/\sigma_L > 3.5$, b) $L/\sigma_L > 4$, b) $L/\sigma_L > 4.5$, b) $L/\sigma_L > 5$.

of the D^+.

It is possible that the Λ^0 candidates in the $\Lambda^0 K^- \pi^+ \pi^+$ combinations are misidentified K_s^0, therefore, one assigns the Λ^0 candidates the K_s^0 mass (0.497 MeV/c^2) and replots the invariant mass of the $\Lambda^0 K^- \pi^+ \pi^+$ sample according to the K_s^0 hypothesis. Figure 4.12 illustrates that no $K_s^0 K^- \pi^+ \pi^+$ reflection peaks are evident and that the exclusion of the D^+ and D_s^+ mass regions does not affect the peak in the $\Lambda^0 K^- \pi^+ \pi^+$ channel. The same is true for the $D^+ \rightarrow K_s^0 \pi^- \pi^+ \pi^+$ state. Although these D^+ and D_s^+ misidentification studies seem to have ruled out the possibilities of reflections from the relevant decay channels (as did the $\Lambda_c^+ \rightarrow \Lambda^0 \pi^+ \pi^- \pi^+$ misidentification study for Λ_c^+ contamination), the fact remains that the $\Lambda^0 K^- \pi^+ \pi^+$ mass peak lies 20 MeV/c^2 below the currently accepted mass of the Ξ_c^+ . One should therefore exercise extreme care in claiming this signal as evidence for the $\Xi_c^+ \rightarrow \Lambda^0 K^- \pi^+ \pi^+$ decay.

4.4.4 Influence of $\Xi_c^+ \rightarrow \Sigma^0 K^- \pi^+ \pi^+$

Another way to intepret the peculiarity of the low mass peak could be to advance the notion that we are observing the $\Xi_c^+ \rightarrow \Sigma^0 K^- \pi^+ \pi^+$ where the Σ^0 decays to a Λ^0 and an unseen γ. The mass of the $\Lambda^0 K^- \pi^+ \pi^+$ peak that one reconstructs would fall below the currently accepted Ξ_c^+ mass because the energy and momentum of the γ would be missing from the invariant mass calculation. Indeed, E400 interpreted the lower peak in its $\Lambda^0 K^- \pi^+ \pi^+$ mass spectrum according to this hypothesis [Cot 87]; this second peak was about 75 MeV/c^2 lower than the main peak at 2460 MeV/c^2 . Testing this theory on the E-687 data set involved generating a Monte Carlo sample of $\Xi_c^+ \rightarrow \Sigma^0 K^- \pi^+ \pi^+$ decays and plotting the corresponding invariant mass, as shown in Figure 4.13. One can see from the histogram that although a Gaussian peak exists, neither its mass of 2385 MeV/c^2 nor its width compares favorably with these features seen in the data. (Incidentally, the width of the peak at 2444 MeV/c^2 in the data

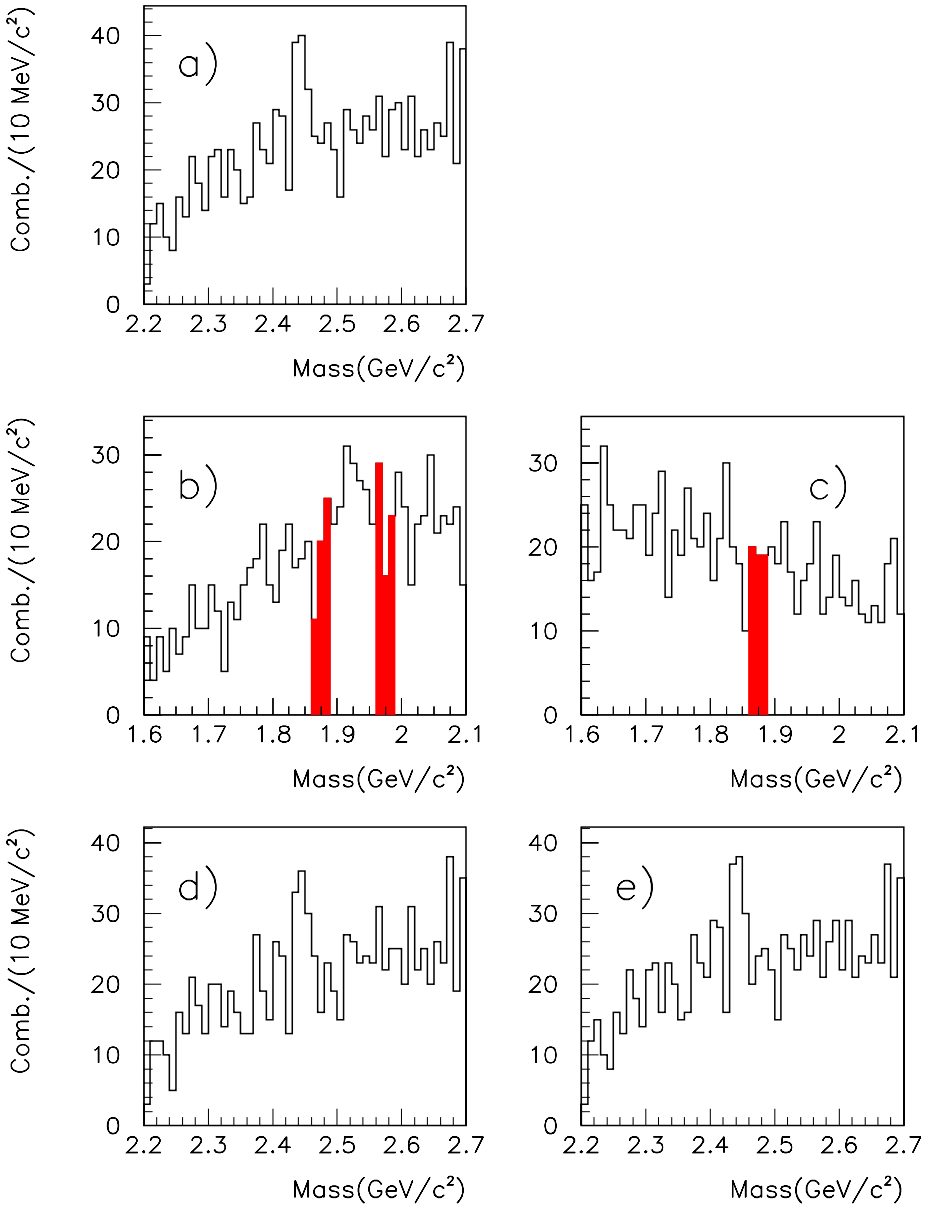

Figure 4.12. Invariant mass distributions of a) the $\Lambda^0 K^- \pi^+ \pi^+$ channel for $L/\sigma_L > 4$, b) the $K_s^0 K^- \pi^+ \pi^+$ reflection, c) the $K_s^0 \pi^- \pi^+ \pi^+$ reflection, d) the $\Lambda^0 K^- \pi^+ \pi^+$ channel excluding the D^+ and D_s^+ mass regions in b), and e) the $\Lambda^0 K^- \pi^+ \pi^+$ channel excluding the D^+ mass region in c).

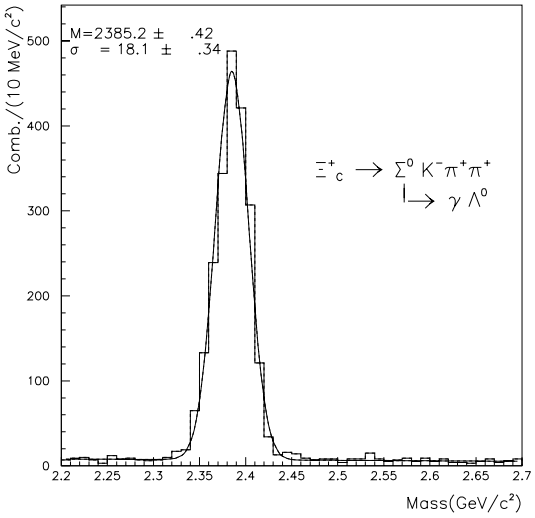

Figure 4.13. Monte Carlo invariant mass distribution of the $\Lambda^0 K^-\pi^+\pi^+$ channel, from a sample of $\Xi_c^+ \to \Sigma^0 K^-\pi^+\pi^+$ events. The Σ^0 decays into a Λ^0 and an unseen γ. The mass and width do not equate with those seen in the data.

agrees well with the width of the Monte Carlo $\Xi_c^+ \to \Lambda^0 K^-\pi^+\pi^+$ signal.) Therefore, the interpretation of the peak at 2444 MeV/c^2 as a $\Xi_c^+ \to \Sigma^0 K^-\pi^+\pi^+$ decay fails. At this point, it seems unlikely that this problem regarding the validity of the $\Lambda^0 K^-\pi^+\pi^+$ enhancement will be resolved.

4.5 The $\Xi_c^+ \to \Xi^-\pi^+\pi^+$ Sample

This decay channel provides one with a good opportunity to observe the Ξ_c^+ baryon for two reasons. First, the relatively small number of Ξ^- in the data sample helps to suppress the combinatoric background, especially when compared with charm baryon decays which contain a lambda as part of the final state. Second, since the spectrometer detects the type two cascades (recall that type two cascades decay after traveling through the microstrip system) as charged SSD tracks, one can exploit the excellent performance of the candidate driven vertexing algorithm involving charged-track-only final states. Table 4.4 lists the specific cuts used to extract the $\Xi^-\pi^+\pi^+$ signal; Fig-

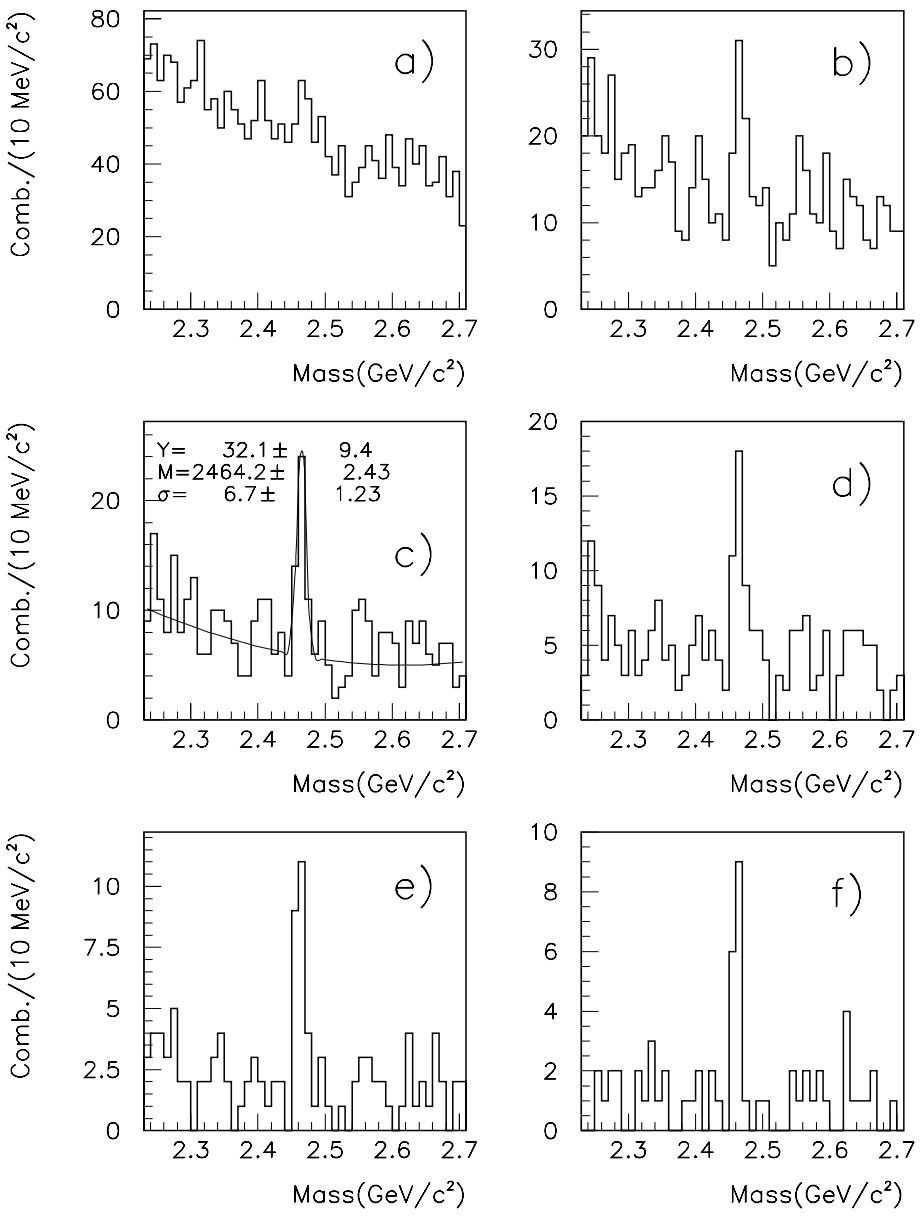

Figure 4.14. Invariant mass distributions of the $\Xi_c^+ \to \Xi^-\pi^+\pi^+$ decay channel for various values of the L/σ_L cut: a) $L/\sigma_L > 1$, b) $L/\sigma_L > 2$, c) $L/\sigma_L > 2.5$, d) $L/\sigma_L > 3$, e) $L/\sigma_L > 4$, f) $L/\sigma_L > 5$.

Table 4.4. Cuts used to obtain the $\Xi_c^+ \to \Xi^-\pi^+\pi^+$ signals

Requirement	Requirement Value
Linking between the PWC and SSD Candidate Tracks	Yes
Mass cut on Ξ^- Candidate	1321.32 ± 10 MeV/c^2 (type Two Only)
Pion ID	ISTATP $\neq 1, 4, 8, 12$
L/σ_L	$> 2, ..., > 5$
Confidence Level of the Primary Vertex	> 1 %
Confidence Level of the Charm Vertex	> 1 %
CL1	Not Used
CL2	Not Used

ure 4.14 displays the signals. The Gaussian fits to the peaks yield masses which agree quite well with the world average of 2465.1 MeV/c^2 [PDG 94].

Now that the task of exposing the desired signals has been accomplished, the measurements of the relative branching ratios can be performed.

CHAPTER 5

The Relative Branching Ratio Measurements

Clear evidence exists for the $\Lambda_c^+ \to \Lambda^0\pi^+\pi^-\pi^+$ decay as was shown in the previous chapter. Unfortunately, the $\Xi_c^+ \to \Lambda^0 K^-\pi^+\pi^+$ state presented what appears to be an unsolvable problem: its mass lies about 20 MeV/c^2 below the world average 2465.4 MeV/c^2 [PDG 94]. However, the mass of the Ξ_c^+ as determined from the reconstruction of the $\Xi_c^+ \to \Xi^-\pi^+\pi^+$ state agrees well with the world average. This, and the fact that the mass of the $\Lambda_c^+ \to \Lambda^0\pi^+\pi^-\pi^+$ state agrees well with the world average for the Λ_c^+ mass (2285 MeV/c^2 [PDG 94]) would seem to indicate that there is no appreciable systematic error involved in measuring the masses of the charm baryons. At this point it is unclear if this $\Xi_c^+ \to \Lambda^0 K^-\pi^+\pi^+$ peak arises due to a statistical fluctuation or if it exists as an undetermined reflection. The problems encountered in studying this state have led to its exclusion from further study, and the ensuing branching ratio analysis will be for the $\Lambda_c^+ \to \Lambda^0\pi^+\pi^-\pi^+$ and $\Lambda_c^+ \to pK^-\pi^+$ states only.

5.1 The Monte Carlo

The first step involved in a relative branching ratio measurement requires one to produce evidence for the signals of interest. The second step is to perform the Monte Carlo simulation of the states and to examine the resulting signals. Raw hit

information is generated and subjected to the identical reconstruction algorithm used on the actual data, and then to the identical analysis algorithm used for the particular state.

Since the charm baryon analysis discussed in this thesis does not involve electromagnetic calorimetry or the muon system (as is the case with the majority of the E-687 analyses) it utilizes the E-687 designed Monte Carlo simulation known as ROGUE, which opts for a reduced state of detector simulation [Lin 90]. Three steps constitute the structure and the execution of this Monte Carlo algorithm, the first being the CHAT file which specifies the particular state of interest by means of an interactive program. The CHAT file includes relevant parameters needed in the production and decay of the charm particles, including the masses and lifetimes of both the charm particles and the particles to which they decay. Event generation, the second step in the Monte Carlo algorithm, was performed according to the LUND model [Gar 92] which recently has replaced GENERIC as the E-687 standard; in part, it calculates an incident photon spectrum, interaction position, lifetime of the charm particle, and then assigns the final decay state as well as providing an anticharm particle for charm conservation. The remaining portion of the ROGUE structure generates the electronic hits in the detectors and reconstructs this raw hit information on an event-by-event basis. Effects of the master gate and the second level trigger are included in the program, and only those events which satisfy each of these have their reconstructed information written to tape.

5.2 The Methodology of Relative Branching Ratio Measurements

For a particle P decaying to states α_1 and α_2, one measures the relative decay rate according to the following formula:

$$\frac{B(P \to \alpha_1)}{B(P \to \alpha_2)} = \frac{Y^{\alpha_1}}{Y^{\alpha_2}} \cdot \frac{\epsilon^{\alpha_2}}{\epsilon^{\alpha_1}} \tag{5.1}$$

In this equation Y^{α_1} and Y^{α_2} represent the data yields for each of the two states, and ϵ^{α_1} and ϵ^{α_2} represent the corresponding Monte Carlo efficiencies. The term "efficiency" is defined as the yield of the Monte Carlo signal for a final state α_n (under the influence of the cuts which produced the corresponding data signal) divided by the number of generated Monte Carlo events for that particular state. Thus,

$$\epsilon^{\alpha_n} = \frac{Y_{MC}^{\alpha_n}}{\mathcal{G}^{\alpha_n}} \tag{5.2}$$

where $Y_{MC}^{\alpha_n}$ represents the Monte Carlo yield for state α_n and $\mathcal{G}^{\alpha_n}$ represents the generated number of Monte Carlo events for state α_n.

The statistical error associated with Equation 5.1 involves only the errors in the yields from the fits to both the data and the Monte Carlo signals, although the Monte Carlo error becomes negligible when large numbers of events are generated. In general for a function of n variables given by $F(x_1, x_2, \ldots, x_{n-1}, x_n)$ where each of the quantities possesses an associated measurement error $\delta(x_1)$, $\delta(x_2)$, $\ldots$, $\delta(x_{n-1})$, $\delta(x_n)$, and assuming that correlations are zero among variables, the total error in the

function can be expressed as:

$$\delta F = \sqrt{\sum_{i=1}^{n} \left(\frac{\partial F}{\partial x_i} \right)^2 (\delta x_i)^2} \tag{5.3}$$

One treats Equation 5.1 as a function of four variables (Y^{α_1}, Y^{α_2}, ϵ^{α_1}, and ϵ^{α_2}) and uses Equation 5.3 to produce the total statistical associated error in the measurement of the branching ratio.

Another source of experimental error in the measurement of the branching ratio includes systematic error originating from biases in the cuts which produce the signals. The relevant procedure and corresponding error estimation will be discussed later.

5.3 *Measurement of* $B(\Lambda_c^+ \rightarrow \Lambda^0\pi^+\pi^-\pi^+)/B(\Lambda_c^+ \rightarrow pK^-\pi^+)$

5.3.1 *The* $\Lambda_c^+ \rightarrow \Lambda^0\pi^+\pi^-\pi^+$ *and* $\Lambda_c^+ \rightarrow pK^-\pi^+$ *Čerenkov Cuts*

In order to preserve the high statistics for each of the decay modes, the analysis algorithms imposed minimal Čerenkov requirements on each of the states; most notable is the loose definition of the pion candidate tracks (ISTATP $\neq$ 1,4,8,12) since one desires to retain as much of the $\Lambda_c^+ \rightarrow \Lambda^0\pi^+\pi^-\pi^+$ signal as possible. However, the $\Lambda_c^+ \rightarrow pK^-\pi^+$ state affords one the opportunity to look at its various subcategories with respect to the Čerenkov identities of the proton and the kaon candidates, for different combinations exist which contribute to the total signal.

A look at such subcombinations reveals some to be more significant than others regarding statistical strength and quality, as Figure 5.1 indicates. First, the category which contains proton and kaon candidates each of ISTATP= 12 is primarily dominated by background and is prone to be misidentified $K^+K^-\pi^+$. Therefore we omit such combinations from the $\Lambda_c^+ \rightarrow pK^-\pi^+$ sample. Second, the ISTATP= 7

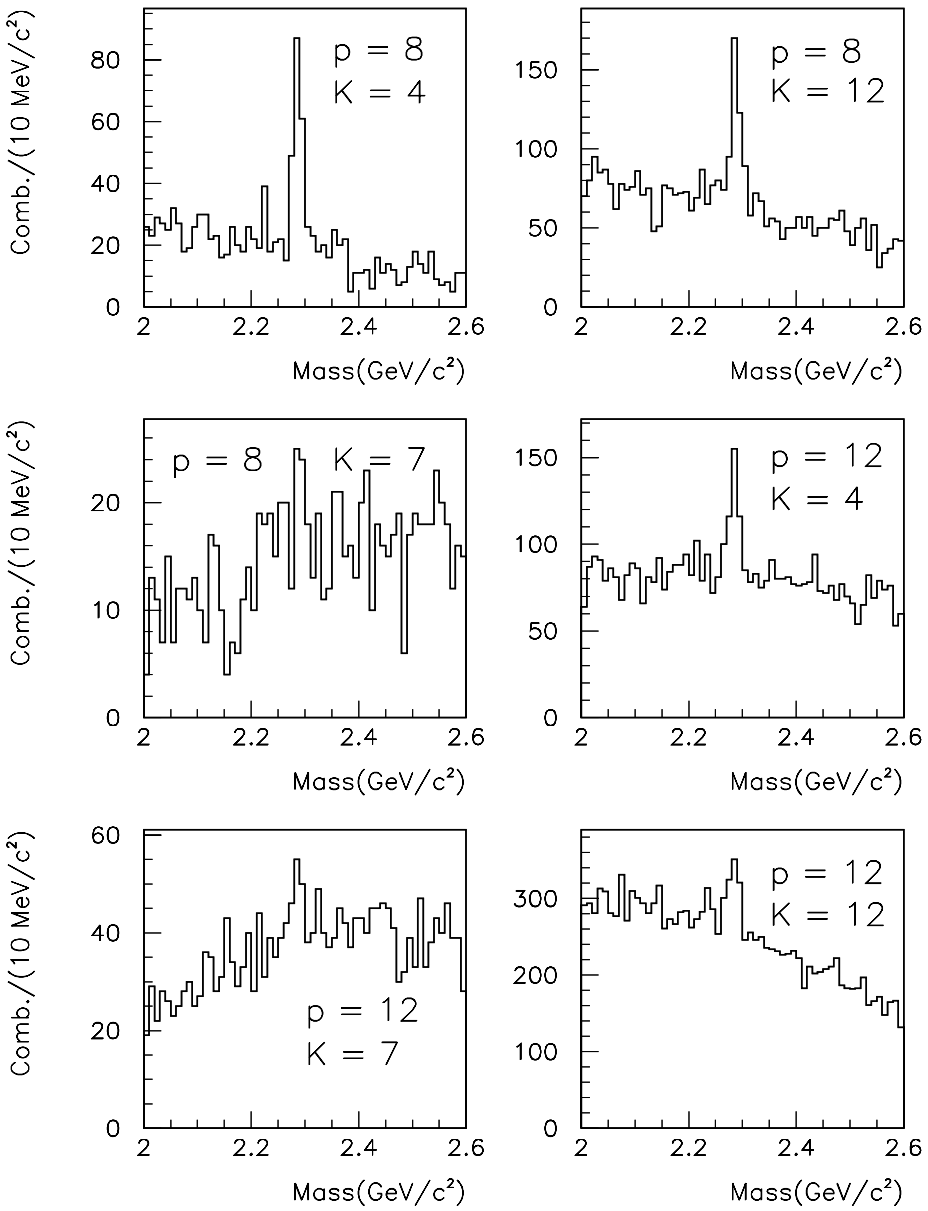

Figure 5.1. The $\Lambda_c^+ \to pK^-\pi^+$ signal for $L/\sigma_L > 5$ divided into subcategories according to the ISTATP values of the proton and the kaon.

class of kaons[1] augments the total signal little while principally producing a low-level background; therefore proton-kaon combinations containing kaons of ISTATP= 7 are excluded from the sample, also. The pion candidate in this state was required to have the same Čerenkov definition as the pion candidates in the $\Lambda_c^+ \rightarrow \Lambda^0\pi^+\pi^-\pi^+$ sample in order to maintain consistency. The effects that different Čerenkov combinations have on the branching ratio will be treated as a form of systematic error.

5.3.2 The $\Lambda_c^+ \rightarrow \Lambda^0\pi^+\pi^-\pi^+$ and $\Lambda_c^+ \rightarrow pK^-\pi^+$ Vertex Cuts CLD, CL1, and CL2

After an extensive systematic study, a specific set of vertex cuts was chosen for the two samples. This set of vertex cuts is: CLD$>$ .05, CL1$<$ .8, CL2$<$ .0001, and the value of L/σ_L which was chosen to perform the measurement is $L/\sigma_L > 5$.

5.3.3 The BR Measurement

Figure 5.2 displays the $\Lambda_c^+ \rightarrow \Lambda^0\pi^+\pi^-\pi^+$ and $\Lambda_c^+ \rightarrow pK^-\pi^+$ signals for the set of cuts previously described; the statistical significance of each respective yield is high, and when these yields are inserted into Equation 5.1 the value of the branching ratio[2] is determined to be 0.95 ± 0.17, where the statistical error associated with the fits was obtained from Equation 5.3. (This value for the branching ratio measurement will be modified slightly (see Section 5.5) when we calculate the efficiencies in bins of momentum.) The respective yields and corresponding Monte Carlo efficiencies are displayed in Table 5.1. The numbers of Monte Carlo generated events were 800K for the $\Lambda_c^+ \rightarrow \Lambda^0\pi^+\pi^-\pi^+$ sample and 400K for the $\Lambda_c^+ \rightarrow pK^-\pi^+$ sample; event generation was performed according to the LUND model and incorporated effects

[1] These kaon candidates are subject to the requirement that their momentum be greater than 60 GeV/c .

[2] This value has been corrected for the $\Lambda^0 \rightarrow p\pi^-$ branching fraction of 64%.

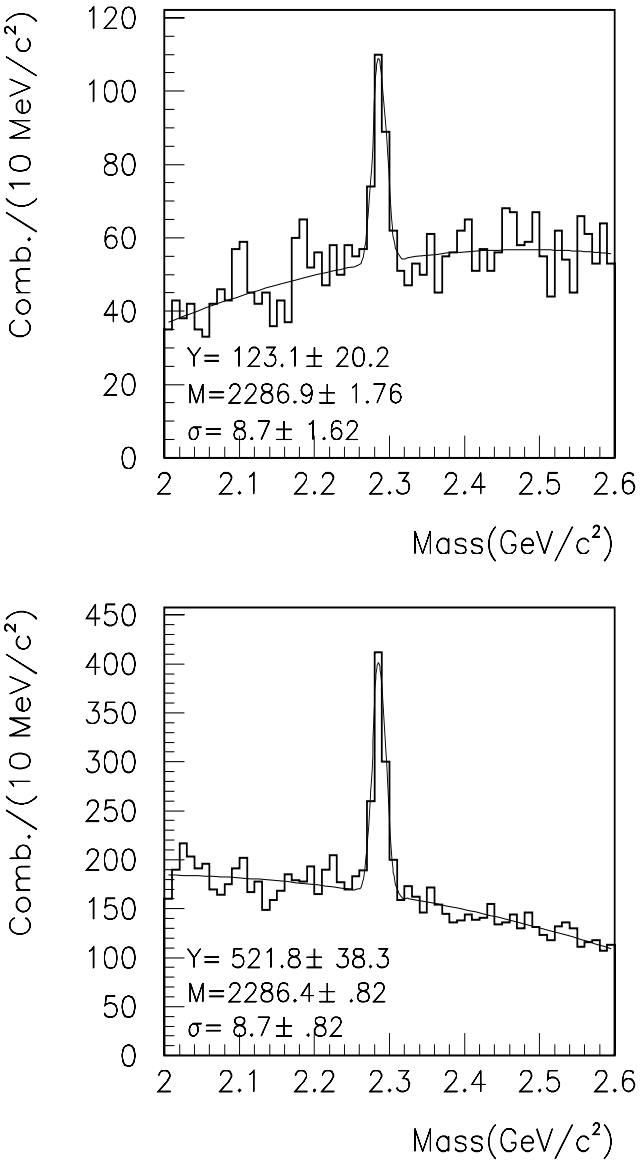

Figure 5.2. Mass distributions of the $\Lambda_c^+ \to \Lambda^0\pi^+\pi^-\pi^+$ and $\Lambda_c^+ \to pK^-\pi^+$ channels for the following cuts: $L/\sigma_L > 5$, CLD $> .05$, CL1 $< .8$, CL2 $< .0001$.

Table 5.1. Yields and efficiencies

Final State	$\Lambda_c^+ \to \Lambda^0\pi^+\pi^-\pi^+$	$\Lambda_c^+ \to pK^-\pi^+$
Data Yield	123 ± 20	522 ± 38
Efficiency(%)	0.5565 ± 0.0100	1.440 ± 0.0200

due to multiple coulomb scattering, hadronic absorption in the target, and track loss due to PWC noise[Cul 94].

The significance of this measurement compares well with that obtained by CLEO, and the measurement itself agrees within errors with the values from each of the other four experiments (see Table 1.1) as well as with the world average [PDG 94]. One notes that the BR is closer to the values from the two fixed target experiments (NA32, E691) and is larger than the values from the collider experiments CLEO and ARGUS.

5.3.4 Systematic Studies

At this point it is important to examine two things. The first is the behavior of the data and Monte Carlo yields under the influence of a variation in the following cuts:

- L/σ_L ;
- CLD ;
- CL1 ;
- CL2 ;
- and the Čerenkov particle identification.

The second is the behavior of the branching ratio under a similar variation. The cuts one chooses for the measurement must be chosen carefully, in regions where the trends in the behavior of the Monte Carlo yields are modeled well with respect to the data. Figure 5.3 illustrates that the $\Lambda_c^+ \to \Lambda^0\pi^+\pi^-\pi^+$ and $\Lambda_c^+ \to pK^-\pi^+$ signals display the proper lifetime behavior with increasing L/σ_L , and that the branching ratio remains flat as one would expect (the Λ_c^+ lifetime of $0.215 \pm 0.016 \pm 0.008$ ps as measured by E-687 [Fra 93c] was used to generate the Monte Carlo samples). Figure 5.4 and Figure 5.5 both display good agreement when the data yields for each of the final states are shown vis-a-vis the corresponding Monte Carlo yields for changing vertex cuts. The branching ratio also remains relatively level as these cuts change, as shown in Figure 5.6.

The effects of different Čerenkov cuts on each of the samples were examined in the following manner. First, the ISTATP codes of the pions in the $\Lambda_c^+ \to \Lambda^0\pi^+\pi^-\pi^+$ and $\Lambda_c^+ \to pK^-\pi^+$ samples were held constant while the ISTATP values of the proton and the kaon in the $\Lambda_c^+ \to pK^-\pi^+$ sample were varied. Second, the ISTATP codes of the pions in both samples were varied while the values of the proton and kaon in the $\Lambda_c^+ \to pK^-\pi^+$ sample were held constant.

The values of the resulting branching ratios shown in Figure 5.7 remain constant within the statistical errors.

5.3.5 Estimation of the Systematic Error in $B(\Lambda_c^+ \to \Lambda^0\pi^+\pi^-\pi^+)/B(\Lambda_c^+ \to pK^-\pi^+)$

Now that a systematic study of the branching ratio has been performed, one assigns a systematic error to the measurement which heretofore involved only the statistical error. One may estimate a systematic error by measuring the desired quantity several times under different sets of conditions and noting how much the measurement deviates. The total systematic error has been determined by summing

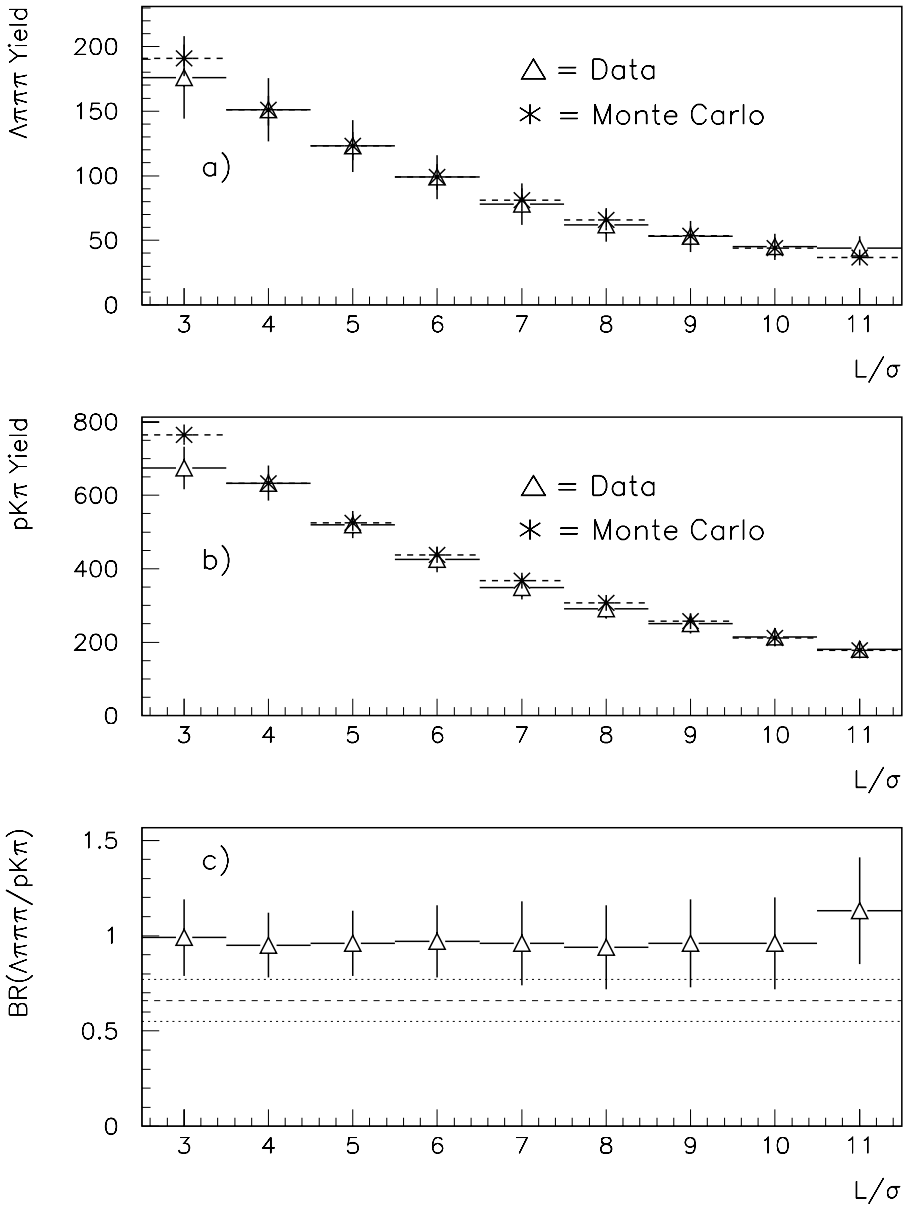

Figure 5.3. Data vs. Monte Carlo yields for each of the decay channels when L/σ_L is varied (normalized to data): a) $\Lambda_c^+ \to \Lambda^0\pi^+\pi^-\pi^+$, and b) $\Lambda_c^+ \to pK^-\pi^+$. Part c) shows the corresponding variation in the branching ratio with L/σ_L . Dotted lines indicate the world average for this branching ratio with error bars.

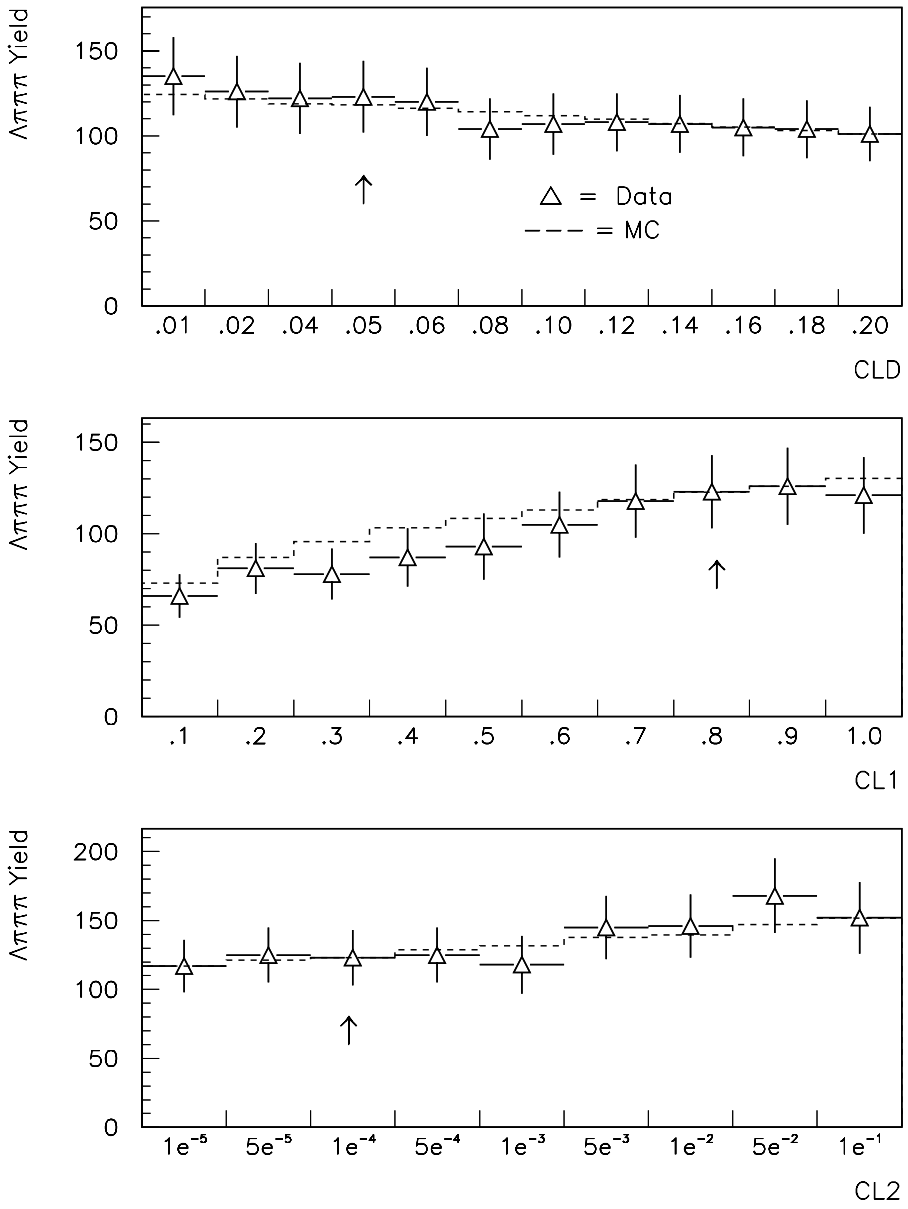

Figure 5.4. $\Lambda_c^+ \to \Lambda^0\pi^+\pi^-\pi^+$ Data vs. Monte Carlo yields as functions of the CLD, CL1, and CL2 cuts (normalized to data). Arrows indicate the selected values of the cuts used for the branching ratio calculation.

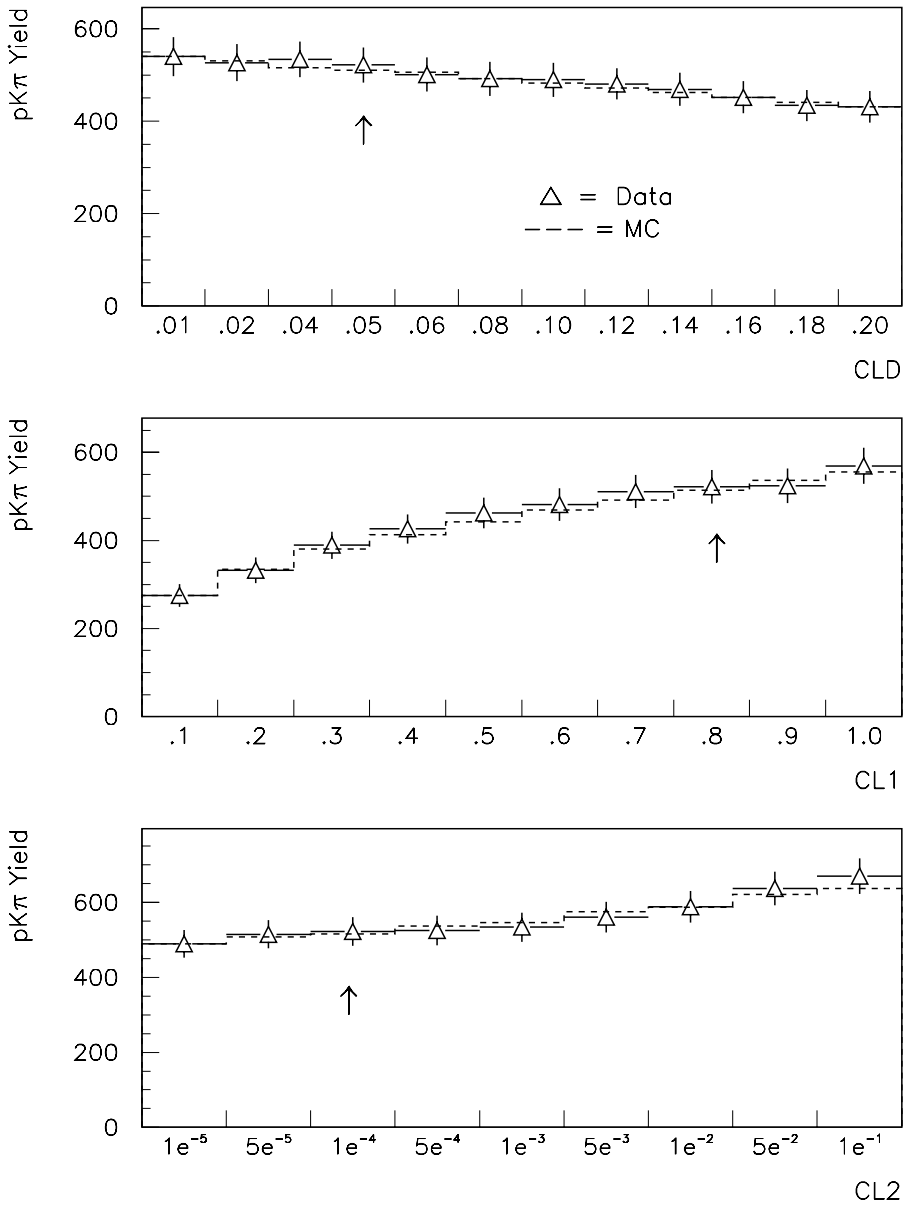

Figure 5.5. $\Lambda_c^+ \to pK^-\pi^+$ Data vs. Monte Carlo yields as functions of the CLD, CL1, and CL2 cuts (normalized to data). Arrows indicate the selected values of the cuts used for the branching ratio calculation.

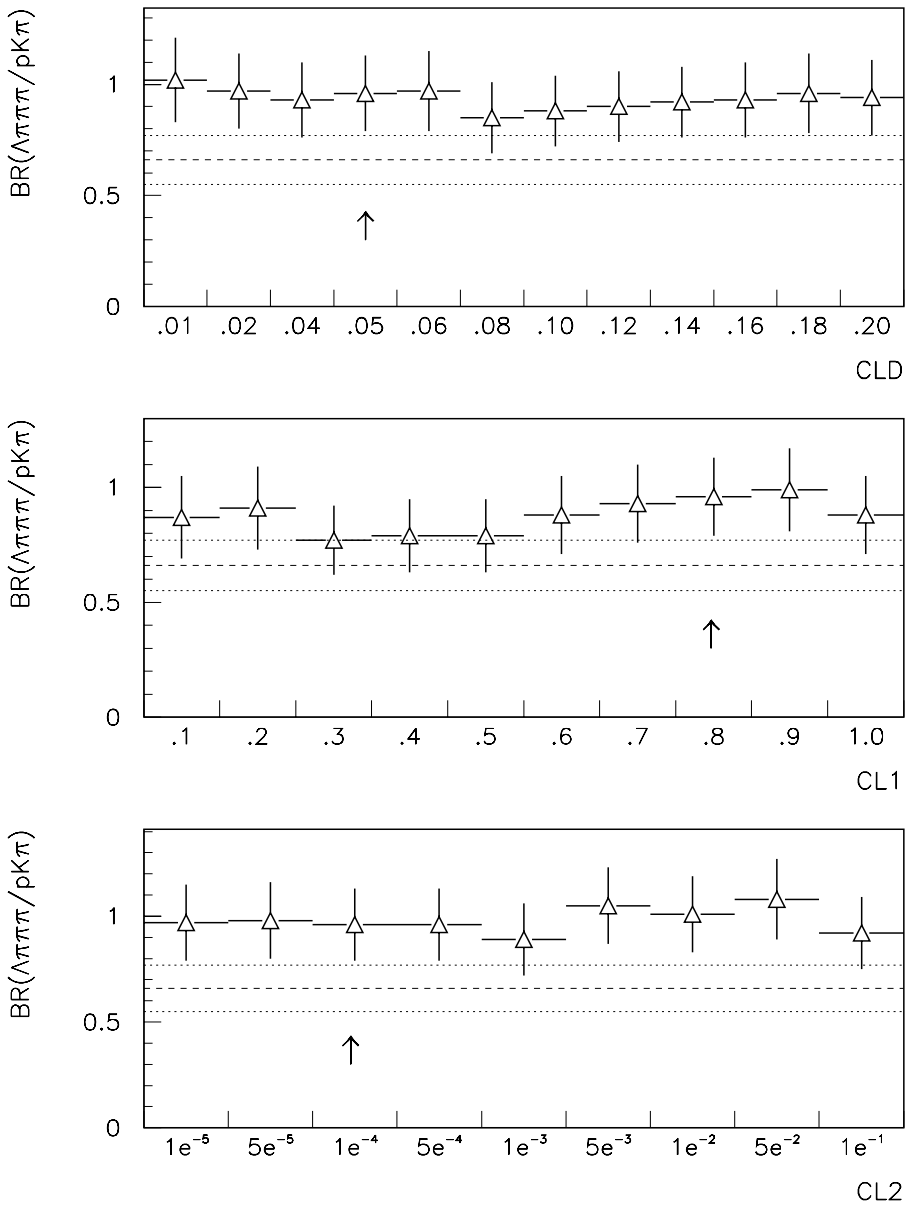

Figure 5.6. $B(\Lambda_c^+ \to \Lambda^0\pi^+\pi^-\pi^+)/B(\Lambda_c^+ \to pK^-\pi^+)$ as functions of the CLD, CL1, and CL2 cuts. Arrows indicate the selected values of the cuts used for the branching ratio calculation.

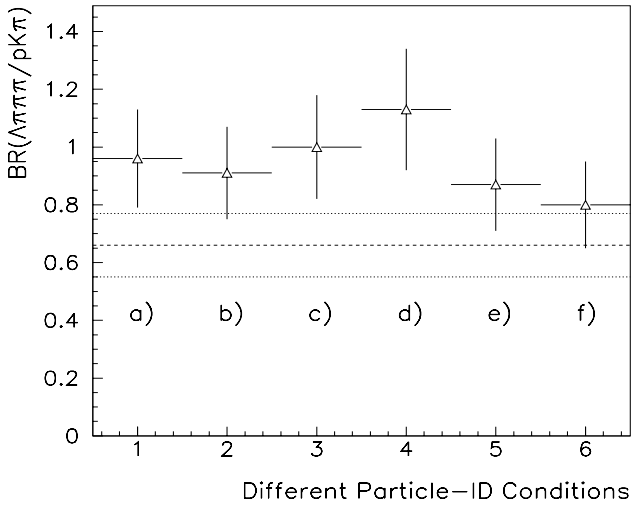

Figure 5.7. The branching ratio as a function of different Čerenkov cuts. Parts b) through d) have standard pion ISTATP$\neq$1,4,8,12 and vary that of the proton and kaon, while parts e) and f) have the standard proton/kaon ISTATP (see Section 5.3.1) and vary that of the pion: a) Standard Čerenkov cuts; b) p= 8 or 12, K= KP7; c) p= 8 or 12, K= KP7, p and K not both equal to 12; d) p= 8, K= KP7; e) one $\Lambda_c^+ \to \Lambda^0\pi^+\pi^-\pi^+$ pion= 2 or 3, $\Lambda_c^+ \to pK^-\pi^+$ pion= 2 or 3; f) two $\Lambda_c^+ \to \Lambda^0\pi^+\pi^-\pi^+$ pions= 2 or 3, $\Lambda_c^+ \to pK^-\pi^+$ pion=2 or 3.

the individual systematic errors in quadrature and by taking the square root of the sum; each individual systematic error originates from the specific cut involved. In this case the principal cuts used in the measurement were the L/σ_L , CLD, CL1, CL2, and Čerenkov cuts.

By looking at the relevant figures (Figure 5.3, Figure 5.6, and Figure 5.7) one chooses an appropriate upper bound and a lower bound on the systematic error for each of the cuts, sums in quadrature the upper-bound errors and the lower-bound errors separately, takes the respective square roots, and obtains two distinct total systematic errors: an upper limit and a lower limit. The formula used to compute this error is expressed as follows:

$$\sigma_{\pm} = \sqrt{(\sigma_{\pm}^{L/\sigma_L})^2 + (\sigma_{\pm}^{CLD})^2 + (\sigma_{\pm}^{CL1})^2 + (\sigma_{\pm}^{CL2})^2 + (\sigma_{\pm}^{\check{C}erenkov})^2} \qquad (5.4)$$

The $\pm$ designation indicates the upper-bound or lower-bound component of the systematic error. From Figure 5.3, Figure 5.6, Figure 5.7 and Equation 5.4 the total upper-bound and lower-bound errors (for a central value of 0.95) are calculated to be

$$\sigma_+ \; = \; + \, 0.13 \quad \sigma_- \; = \; - \, 0.15 \quad . \qquad (5.5)$$

Table 5.2 lists the upper-bound and lower-bound errors for each of the cuts.

5.4 Other Systematic Checks

In addition to examining the systematics of the L/σ_L cut, the vertex cuts, and the Čerenkov cuts, other facets of the analysis should also be checked for consistency. These include a misidentification-reflection study of the $\Lambda_c^+ \rightarrow pK^-\pi^+$ and $\Lambda_c^+ \rightarrow \Lambda^0\pi^+\pi^-\pi^+$ channels, a separation of the data sets into their 1990 and 1991

Table 5.2. Respective values of σ_+ and σ_- for the L/σ_L , CLD, CL1, CL2, and Čerenkov identification cuts.

Cut	σ_+	σ_-
L/σ_L	+.04	-.01
CLD	+.02	-.07
CL1	+.04	-.08
CL2	+.10	-.06
Čerenkov	+.05	-.08
Total	+.13	-.15

components, a separation of the data sets into their particle and antiparticle components, and an examination of the branching ratio according to the vee type of the lambda particle in the $\Lambda_c^+ \rightarrow \Lambda^0\pi^+\pi^-\pi^+$ state. Since each of these procedures reduces the signals into smaller samples, the associated errors increase. Therefore, these studies will not be used to increase the estimate of the systematic error already obtained but will instead serve as consistency checks.

5.4.1 Reflection Studies

Since the $\Lambda_c^+ \rightarrow \Lambda^0\pi^+\pi^-\pi^+$ and $\Lambda_c^+ \rightarrow pK^-\pi^+$ samples might contain contamination from the $D^+ \rightarrow K_s^0\pi^+\pi^-\pi^+$; $D^+ \rightarrow K^+K^-\pi^+$, and $D_s^+ \rightarrow K^+K^-\pi^+$ decays, respectively, it is important to check each state for its associated reflection and discern the effects on the branching ratio.

The $\Lambda_c^+ \rightarrow pK^-\pi^+$ channel may involve a pronounced effect because the proton candidate in the $pK^-\pi^+$ combination may be K/P ambiguous. When forming the $pK^-\pi^+$ invariant mass, the algorithm *assigns* the proton candidate track the proton mass. Since this track might be a kaon, it is important to assign the proton candidate track the kaon mass and replot the $pK^-\pi^+$ signal events as $K^+K^-\pi^+$ combinations. The $pK^-\pi^+$ signal region was defined as the area within $\pm 2\sigma$ of the fitted Λ_c^+ mass.

To examine how spurious $pK^-\pi^+$ signal entries due to misidentified $K^+K^-\pi^+$ might affect the branching ratio, events which were located in the D^+ and D_s^+ mass regions (1.869 and 1.969 GeV, respectively) were excluded from the $\Lambda_c^+ \rightarrow pK^-\pi^+$ invariant mass plot. A similar procedure was used for the $\Lambda_c^+ \rightarrow \Lambda^0\pi^+\pi^-\pi^+$ channel: the lambda was plotted as a K_s^0 and this K_s^0 mass region was excluded from consideration when forming the $\Lambda_c^+ \rightarrow \Lambda^0\pi^+\pi^-\pi^+$ invariant mass. Figure 5.8 shows the extent to which excluding these mass regions affects the respective $\Lambda_c^+ \rightarrow \Lambda^0\pi^+\pi^-\pi^+$ and $\Lambda_c^+ \rightarrow pK^-\pi^+$ signals and reveals that the resulting branching ratios are affected little.

5.4.2 1990-1991 and Particle-Antiparticle Studies

Figure 5.9 illustrates the $\Lambda_c^+ \rightarrow \Lambda^0\pi^+\pi^-\pi^+$ and $\Lambda_c^+ \rightarrow pK^-\pi^+$ signals when they are split into their 1990 and 1991 data sets. Since doing so causes a loss in statistics by a factor of two, it was decided to fix the peak widths to Monte Carlo values. Figure 5.10 shows the particle and antiparticle portions of the respective states, again with fixed peak widths, while Figure 5.11 shows the corresponding branching ratio measurements for the whole data set and for the 1990, 1991, particle, and antiparticle components. All measurements are compatible within the statistical errors.

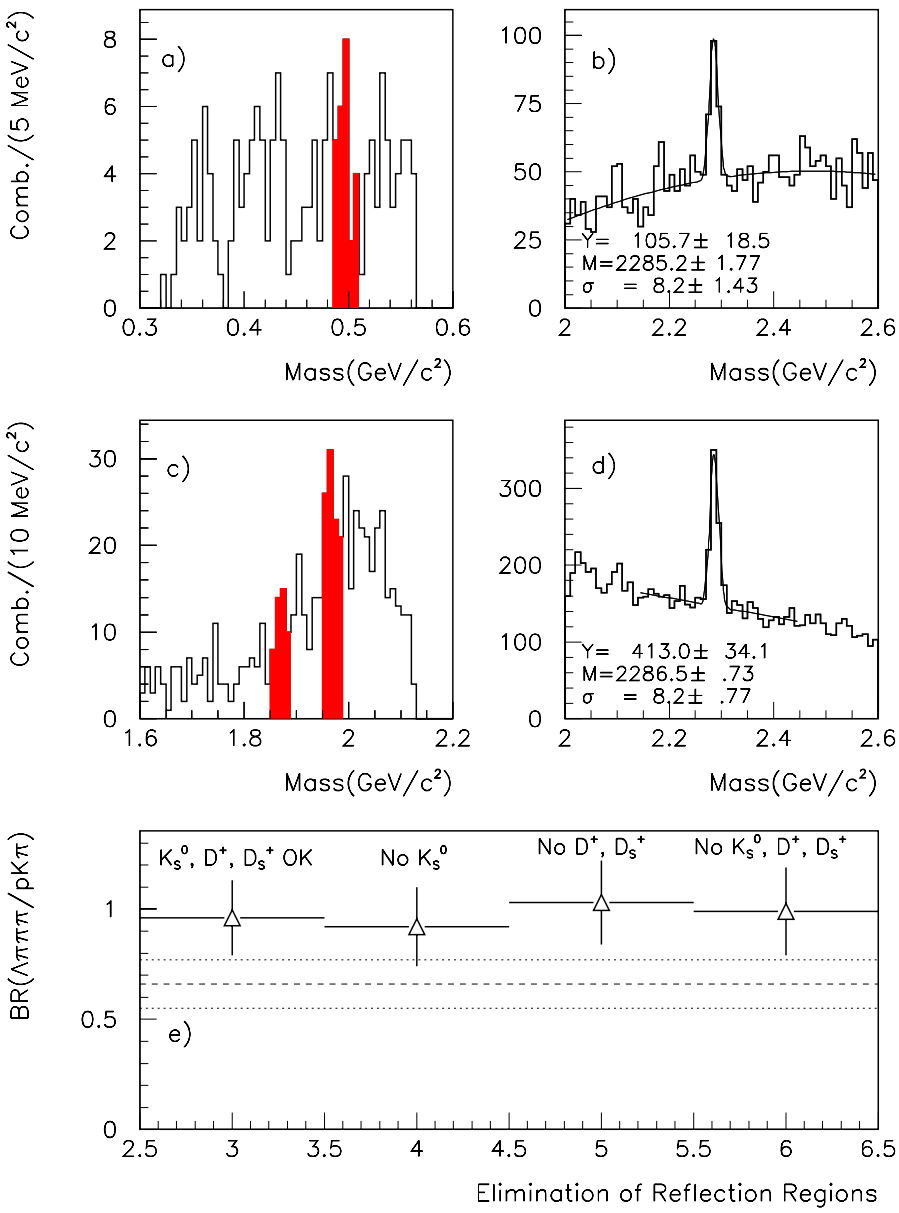

Figure 5.8. The $\Lambda_c^+ \to \Lambda^0\pi^+\pi^-\pi^+$ and $\Lambda_c^+ \to pK^-\pi^+$ channels plotted when the respective misidentified K_S^0; $D^+ \to K^+K^-\pi^+$, and $D_s^+ \to K^+K^-\pi^+$ mass regions are excluded: a) signal region lambdas plotted as K_S^0, b) the $\Lambda_c^+ \to \Lambda^0\pi^+\pi^-\pi^+$ signal when the misidentified K_s^0 mass region is excluded, c) signal region $\Lambda_c^+ \to pK^-\pi^+$ plotted as $K^+K^-\pi^+$, d) the $\Lambda_c^+ \to pK^-\pi^+$ signal when the misidentified $D^+ \to K^+K^-\pi^+$ and $D_s^+ \to K^+K^-\pi^+$ mass regions are excluded, and e) the effects on the branching ratio of excluding the K_s^0; $D^+ \to K^+K^-\pi^+$, and $D_s^+ \to K^+K^-\pi^+$ reflection regions.

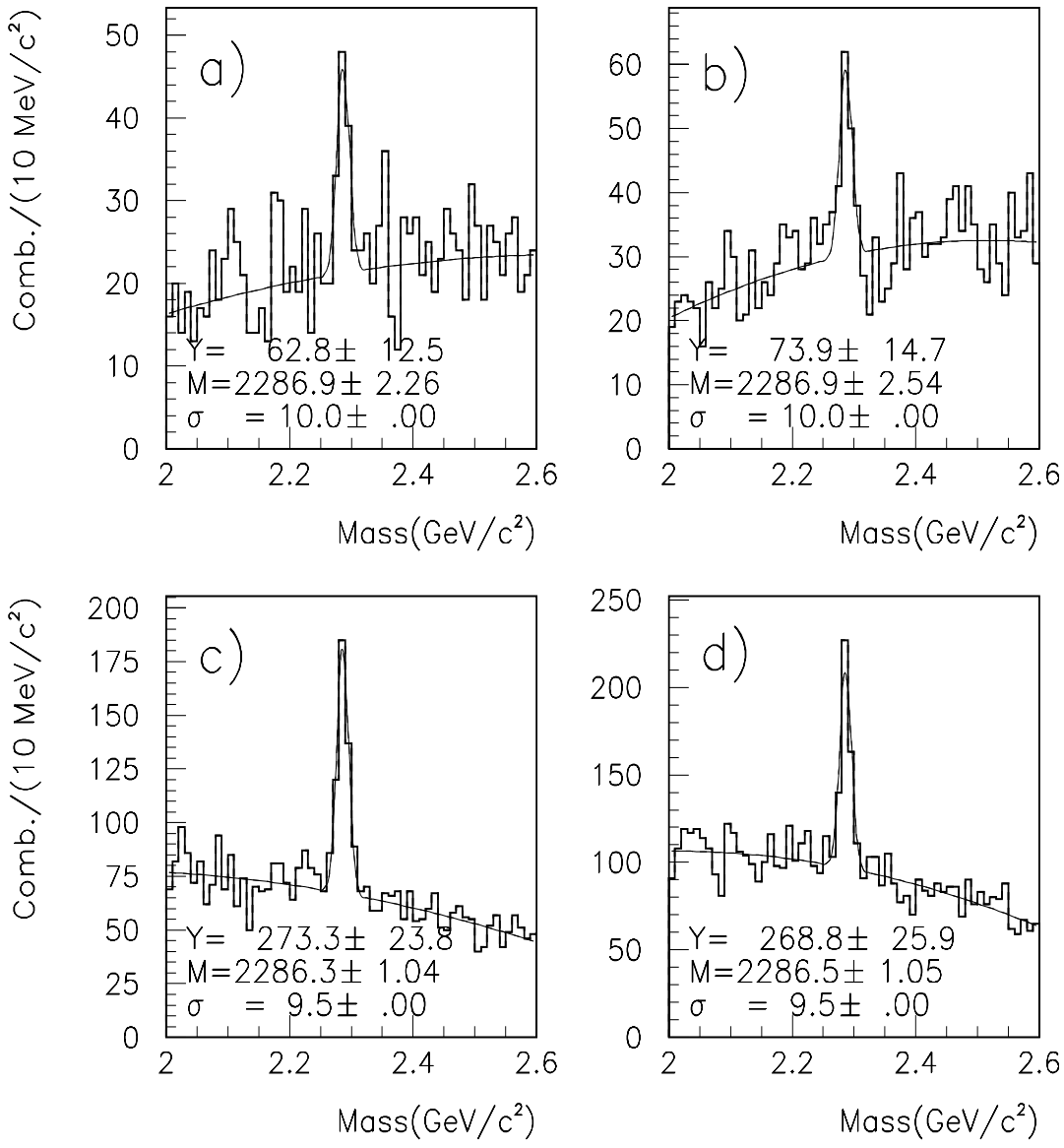

Figure 5.9. 1990-1991 Distinction: a) 1990 $\Lambda_c^+ \rightarrow \Lambda^0\pi^+\pi^-\pi^+$, b) 1991 $\Lambda_c^+ \rightarrow \Lambda^0\pi^+\pi^-\pi^+$, c) 1990 $\Lambda_c^+ \rightarrow pK^-\pi^+$, and d) 1991 $\Lambda_c^+ \rightarrow pK^-\pi^+$.

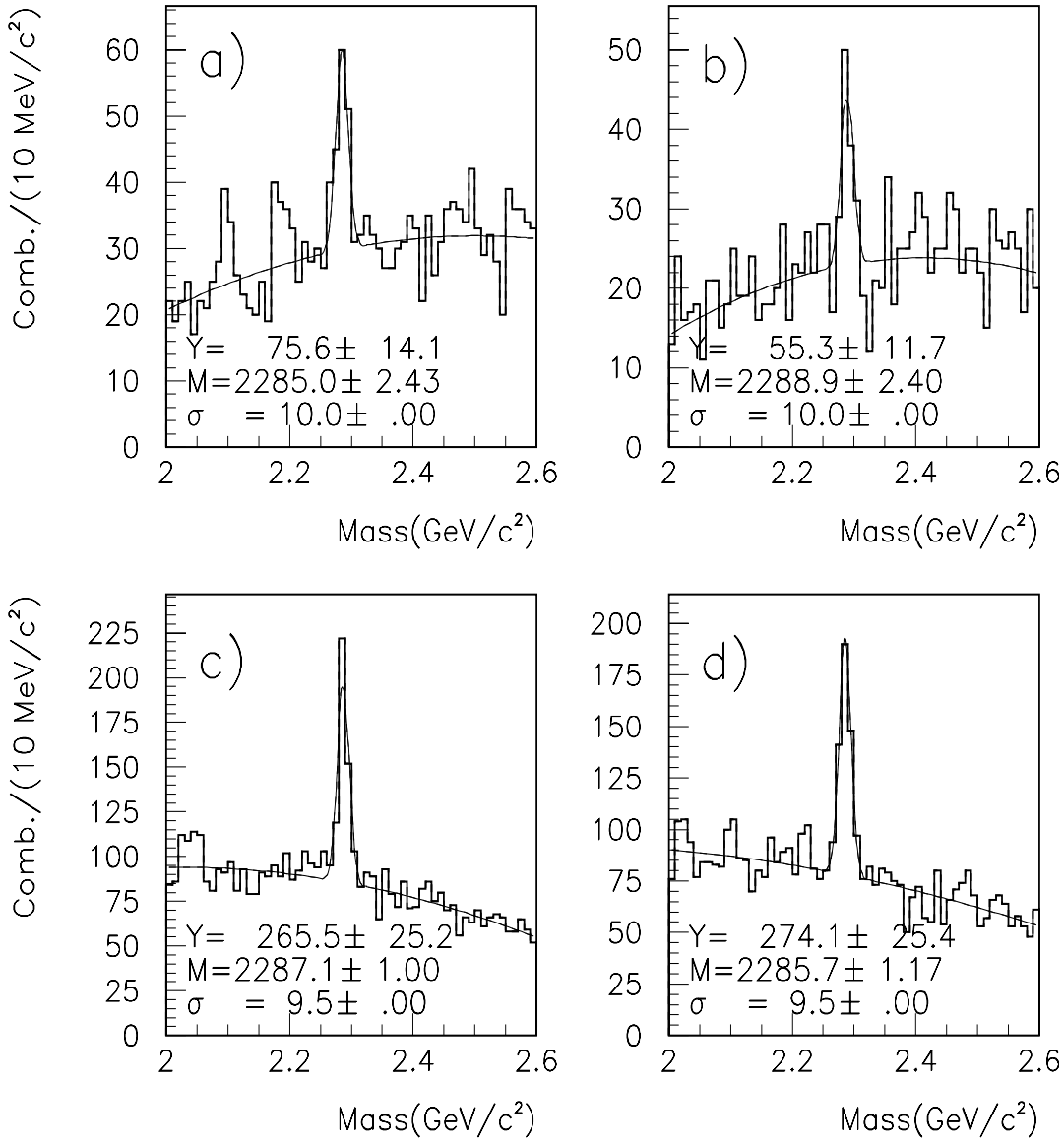

Figure 5.10. Particle-antiparticle distinction: a) particle $\Lambda_c^+ \to \Lambda^0\pi^+\pi^-\pi^+$, b) antiparticle $\overline{\Lambda_c^+} \to \overline{\Lambda^0}\pi^-\pi^+\pi^-$, c) particle $\Lambda_c^+ \to pK^-\pi^+$, and d) antiparticle $\overline{\Lambda_c^+} \to \overline{p}K^+\pi^-$.

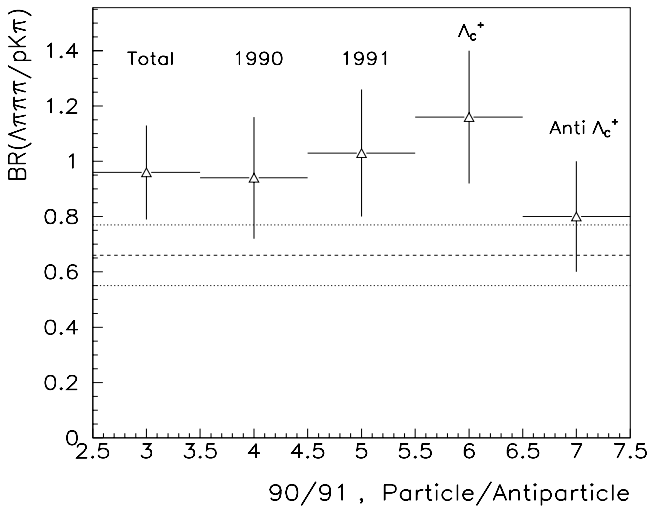

Figure 5.11. The branching ratio divided into the 1990, 1991, particle, and antiparticle components.

5.4.3 Branching Ratio by Vee Type of the Λ^0

Since seven different categories of lambdas exist which are specified by where they decay in the spectrometer, a systematic check was made of the branching ratio for each of the vee categories. Because some of the categories account for little signal (and since the $\Lambda_c^+ \to \Lambda^0\pi^+\pi^-\pi^+$ statistics are already a factor of four low compared to the $\Lambda_c^+ \to pK^-\pi^+$ statistics) such an examination will probably not prove definitively if there are problems in this respect, but can at least indicate whether the branching ratio remains constant within errors according to the Λ^0 vee type.

Figure 5.12 displays the $\Lambda_c^+ \to \Lambda^0\pi^+\pi^-\pi^+$ signal when it is split into its seven constituents, and Figure 5.13 illustrates that the branching ratio does in fact behave reasonably for each of the vee types, although it does seem that the value in the Track-Stub category is a bit high.[3] Although certain vee types present better signals

[3]The efficiency for each vee type was obtained from the overall $\Lambda_c^+ \to \Lambda^0\pi^+\pi^-\pi^+$ Monte Carlo sample.

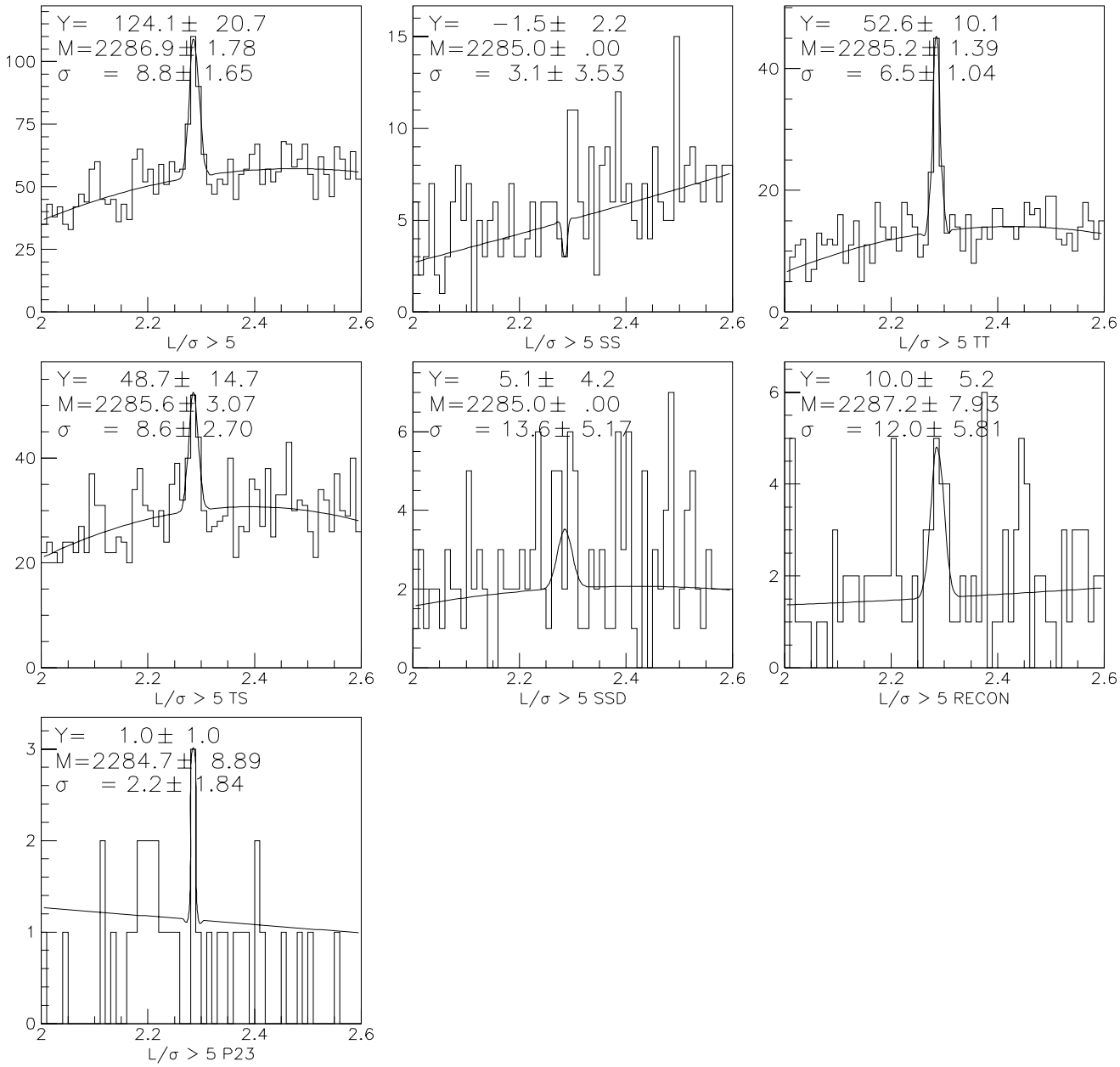

Figure 5.12. The $\Lambda_c^+ \to \Lambda^0\pi^+\pi^-\pi^+$ signal divided into its seven components according to vee type.

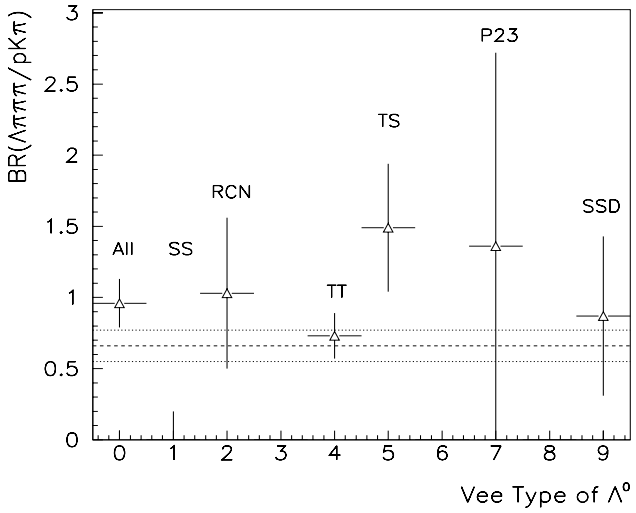

Figure 5.13. The branching ratio according to the vee type of the lambda in the $\Lambda_c^+ \to \Lambda^0\pi^+\pi^-\pi^+$ signal.

and branching ratio behavior than others, all of the lambdas are retained in order to minimize bias in the measurement.

5.5 Momentum Studies

The final step in the analysis is to examine the momentum distributions of the events in the signal regions for both data and Monte Carlo. Since charm baryons exhibit more background than charm mesons, this task is more difficult than it would be for D^+ or D_s^+ decays. This is an important part of a branching ratio analysis because up to this point it has been assumed that the data and Monte Carlo momentum distributions are the same. One must check this and correct for any discrepancies that might be present. Figure 5.14 displays the background-subtracted $\Lambda_c^+ \to \Lambda^0\pi^+\pi^-\pi^+$ and $\Lambda_c^+ \to pK^-\pi^+$ momentum distributions. The $\Lambda_c^+ \to \Lambda^0\pi^+\pi^-\pi^+$ data momentum spectrum is shifted approximately one bin with respect to the Monte Carlo, and there is less agreement at the high end of the spectra;

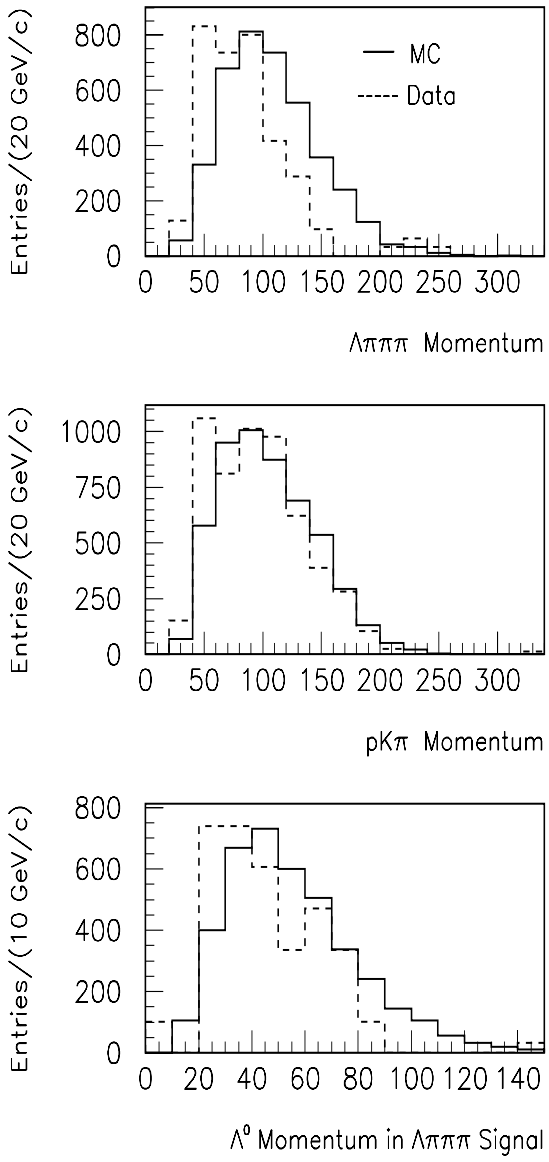

Figure 5.14. Data (background-subtracted) vs. MC momentum distributions for $\Lambda_c^+ \rightarrow \Lambda^0\pi^+\pi^-\pi^+$ signal (top), $\Lambda_c^+ \rightarrow pK^-\pi^+$ signal (middle), and Λ^0 in the $\Lambda_c^+ \rightarrow \Lambda^0\pi^+\pi^-\pi^+$ signal (bottom). Plots are peak normalized to Monte Carlo in a way which facilitates qualitative comparisons of shapes.

the $\Lambda_c^+ \rightarrow pK^-\pi^+$ spectra match better. The signal regions were defined as the fitted masses $\pm 2\sigma$, while the upper and lower sidebands each encompassed half this width. Entries from the upper and lower sidebands were added to form the total backgrounds which were then subtracted from the signal regions when constructing the momentum spectra plots. Also shown in Figure 5.14 is the Λ^0 momentum spectrum for data and Monte Carlo. Plotted is the lambda momentum for lambdas which are a part of the $\Lambda^0\pi^+\pi^-\pi^+$ signal after subtracting sideband regions in the same manner as was previously described. The results look similar to the $\Lambda_c^+ \rightarrow \Lambda^0\pi^+\pi^-\pi^+$ momentum spectra: the momentum of the lambdas (data) is shifted low compared to that of the Monte Carlo lambdas, and not many data lambdas are present in the high momentum region above 90 GeV/c .

5.5.1 Momentum-Dependent Efficiency Calculations

So far, global Monte Carlo efficiencies have been used in calculating the branching ratio $B(\Lambda_c^+ \rightarrow \Lambda^0\pi^+\pi^-\pi^+)/B(\Lambda_c^+ \rightarrow pK^-\pi^+)$, meaning that one obtains an efficiency for a certain set of cuts by dividing the number of Monte Carlo events in the signal by the total number of generated Monte Carlo events. Such an evaluation assumes that the generated charm baryon momentum distribution agrees well with that present in the data. One can check this by calculating the branching ratio by using *momentum-dependent efficiency curves*, a method which entails dividing the Monte Carlo generated momentum spectrum by the Monte Carlo reconstructed signal momentum spectrum, bin by bin. One then weights each entry in the respective invariant mass plot (data) by the inverse of the corresponding efficiency for the momentum of the particular combination, thereby producing efficiency-corrected histograms. The branching ratio is then the ratio of these two fitted signals.

The efficiency for a momentum bin i is given by

$$\epsilon_i = \frac{Y_i}{\mathcal{G}_i} \tag{5.6}$$

where Y_i corresponds to the yield of reconstructed Monte Carlo signal events in the momentum bin i (under the influence of the specific set of cuts used on the particular sample), and where $\mathcal{G}_i$ represents the number of generated Monte Carlo events in that momentum bin i. The weight for the momentum bin i is then simply

$$w_i = \frac{1}{\epsilon_i} \quad . \tag{5.7}$$

Figure 5.15 displays the generated Monte Carlo and reconstructed Monte Carlo momentum distributions for each of the states, along with the momentum-dependent efficiency curves. When applying these curves to the data, the momentum regions were restricted to the range 50-120 GeV/c since this was where most of the $\Lambda_c^+ \rightarrow \Lambda^0\pi^+\pi^-\pi^+$ signal existed. Figure 5.16 shows the efficiency-corrected mass plots; dividing the yields and correcting for the $\Lambda^0 \rightarrow p\pi^-$ branching fraction gives for the momentum-dependent efficiency-corrected branching ratio:

$$1.16 \ \pm \ 0.27 \ {}^{+\ 0.16}_{-\ 0.18} \quad . \tag{5.8}$$

This value agrees within errors with the value of $0.95 \pm 0.17(\textit{statistical})$ in which nothing was done regarding momentum cuts or corrections, and with the value of $0.98 \pm 0.19(\textit{statistical})$ which involved unweighted data only in the momentum range

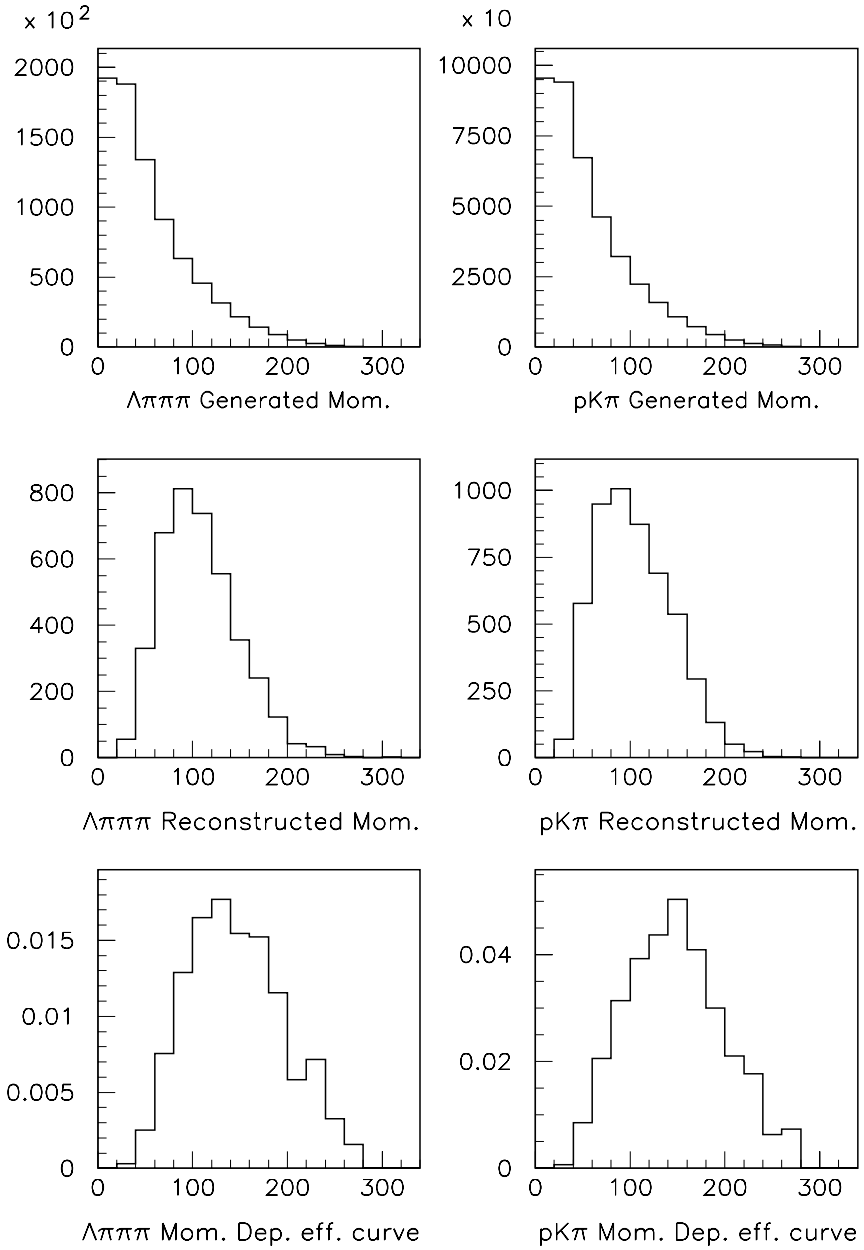

Figure 5.15. The $\Lambda_c^+ \rightarrow \Lambda^0\pi^+\pi^-\pi^+$ (left) and $\Lambda_c^+ \rightarrow pK^-\pi^+$ (right) Monte Carlo generated and reconstructed momentum distributions. The efficiency curves are obtained by dividing the reconstructed momentum spectrum by the generated momentum spectrum bin by bin.

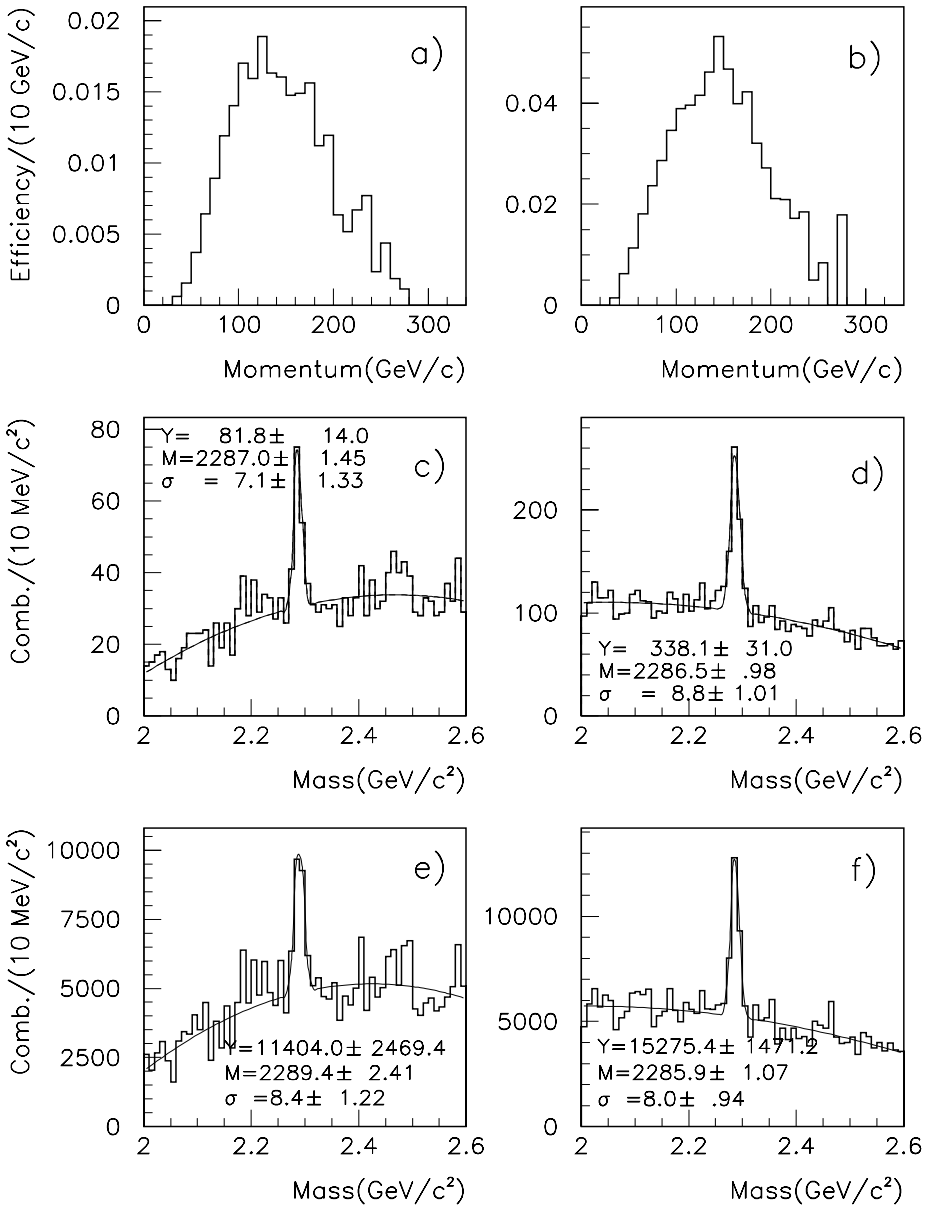

Figure 5.16. Effects of weighting the data with momentum-dependent efficiency curves: a) $\Lambda_c^+ \to \Lambda^0\pi^+\pi^-\pi^+$ efficiency as a function of momentum, b) $\Lambda_c^+ \to pK^-\pi^+$ efficiency as a function of momentum, c) unweighted $\Lambda_c^+ \to \Lambda^0\pi^+\pi^-\pi^+$ mass distribution in the range $50 < p < 120$ (GeV/c), d) unweighted $\Lambda_c^+ \to pK^-\pi^+$ mass distribution in the range $50 < p < 120$, e) weighted $\Lambda_c^+ \to \Lambda^0\pi^+\pi^-\pi^+$ mass distribution in the range $50 < p < 120$, f) weighted $\Lambda_c^+ \to pK^-\pi^+$ mass distribution in the range $50 < p < 120$ GeV/c .

50 to 120 GeV/c . The systematic errors were calculated by obtaining the relative errors for each of the error terms associated with the uncorrected BR measurement, and by multiplying the new value of the branching ratio by these respective percentages. In this specified momentum range of 50-120 GeV/c , no additional split-sample systematic error is present if the data are split into regions of low and high momentum corresponding to regions of 50-85 GeV/c and 85-120 GeV/c , respectively.

The statistical error associated with each efficiency-corrected mass plot was determined by assigning error bars on a bin-by-bin basis to the mass plots. These error bars are not simply the $\sqrt{N_j'}$ (here we designate N_j' as the number of entries in a mass bin j in the weighted mass plots); rather, they involve the errors in the unweighted histogram bins as well as the errors in the weights used to produce the efficiency-corrected plots. The number of events in each efficiency-corrected mass bin j is given by the following expression:

$$N_j' = \sum_{i=1}^{n} N_{ji} w_i \tag{5.9}$$

where the j subscript signifies a *mass* bin and the i subscript refers to a *momentum* bin. The N_j' are the numbers of entries in each of the j efficiency-corrected mass bins; the N_{ji} are the numbers of entries in an unweighted mass bin j which populate a specific momentum bin i (of width 10 GeV; there are seven such bins over a momentum range of 50-120 GeV); and the w_i are the weighting factors which are the inverses of the efficiencies for the i momentum bins as given in Equation 5.7.

Since $N_j' = \sum_{i=1}^{n} N_{ji} w_i$ is a function of two variables; i.e., $N_j' = N_j'(N_{ji}, w_i)$, the

error in the number of entries in a weighted mass bin j is expressed as

$$\delta N'_j = \sqrt{\left(\frac{\partial N'_j}{\partial N_{ji}}\right)^2 (\delta N_{ji})^2 + \left(\frac{\partial N'_j}{\partial w_i}\right)^2 (\delta w_i)^2} \tag{5.10}$$

which, when the derivative operations are performed, becomes

$$\delta N'_j = \sqrt{\sum_{i=1}^{7} \left(w_i^2 \cdot N_{ji} \; + \; N_{ji}^2 \cdot (\delta w_i)^2 \right)} \quad . \tag{5.11}$$

(Recall that $\delta N_{ji} = \sqrt{N_{ji}}$, which accounts for the N_{ji} associated with the first term under the radical.) It is these errors which populate the bins in the efficiency-corrected invariant mass plots and which are responsible for the statistical errors in the fits shown in Figure 5.16.

Since the $\Lambda_c^+ \rightarrow \Lambda^0\pi^+\pi^-\pi^+$ and $\Lambda_c^+ \rightarrow pK^-\pi^+$ efficiencies are functions of momentum, the measurement given in Equation 5.8 is taken to be the final result.

5.6 *Measurement of* $B(\Lambda_c^+ \rightarrow p\overline{K^{*0}}(892))/B(\Lambda_c^+ \rightarrow pK^-\pi^+)$

Finally, we calculate the rate of the $\Lambda_c^+ \rightarrow p\overline{K^{*0}}(892)$ decay relative to that of the $\Lambda_c^+ \rightarrow pK^-\pi^+$ mode. The relevant signals were shown in Chapter 4 and are redisplayed in Figure 5.17 for convenience. The Čerenkov cuts used on the $pK^-\pi^+$ sample were the same as those listed in Table 4.1, but the vertex cuts were tightened somewhat: CLD>0.1, CL2<0.0001.

Since the Monte Carlo efficiencies for each of the two decay modes is nearly identical, we take the ratio of the fitted number of events in the $K^-\pi^+$ mass peak and the

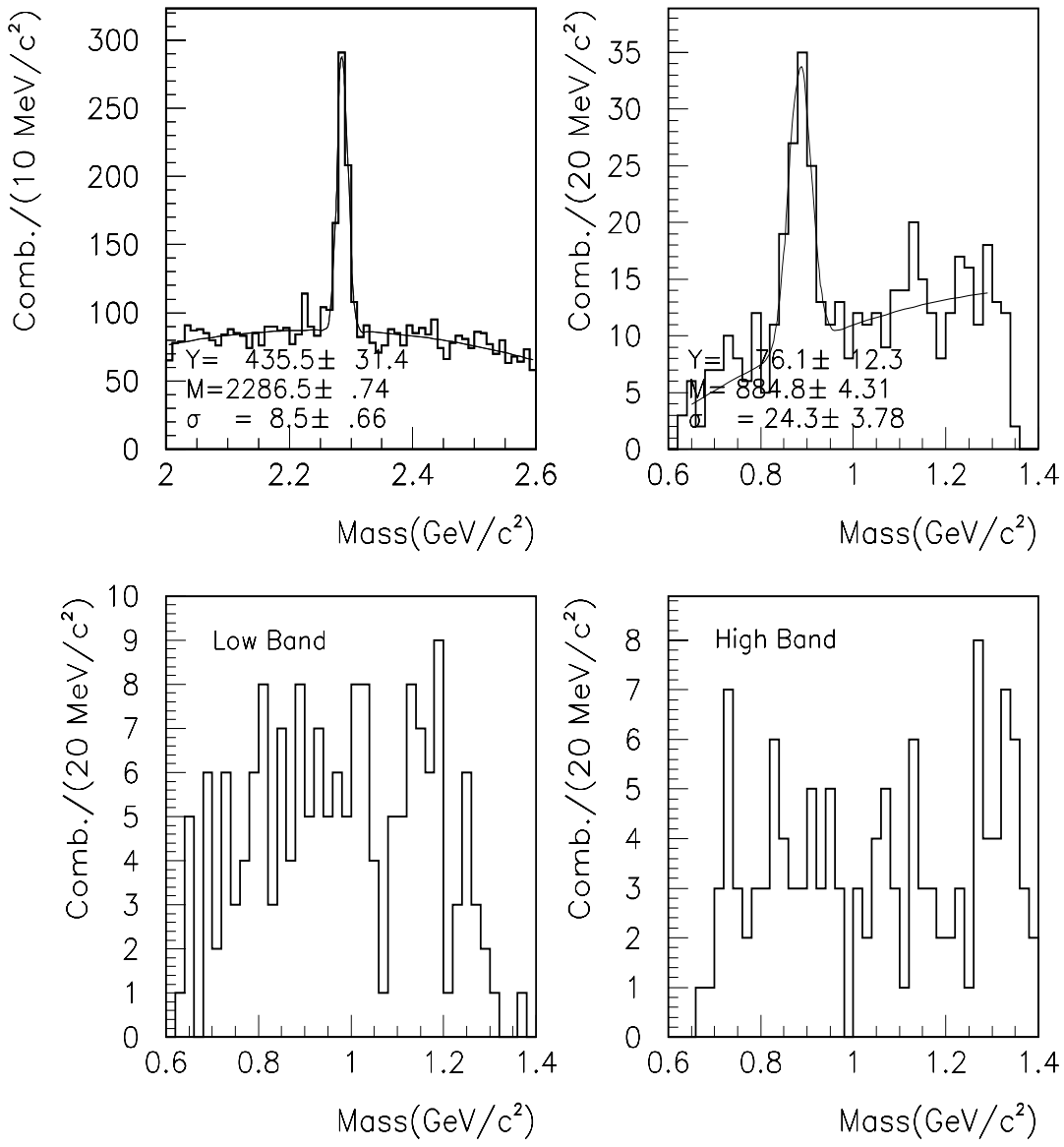

Figure 5.17. Invariant mass distributions of the $pK^-\pi^+$ channel and the corresponding $K^-\pi^+$ substate for the Λ_c^+ signal region, low sideband, and high sideband regions.

number of events in the $pK^-\pi^+$ mass peak[4]. This ratio is then divided by 0.667 which takes into account the unseen $\overline{K^{*0}}(892) \rightarrow \overline{K^0}\pi^0$ decay mode. The relative branching ratio $B(\Lambda_c^+ \rightarrow p\overline{K^{*0}}(892))/B(\Lambda_c^+ \rightarrow pK^-\pi^+)$ is determined to be $0.39 \pm 0.07 \pm 0.07$, where the systematic error (the second error term) was estimated by varying the mass cut in the $pK^-\pi^+$ signal region from one to three standard deviations around the fitted Λ_c^+ mass of 2286.5 MeV/c^2 .

This measurement agrees well with the world average of $0.36\ ^{+0.06}_{-0.07}$ [PDG 94], the great majority of which is due to the NA32 measurement of $0.35\ ^{+0.06}_{-0.07} \pm 0.03$ which was based on 39 $\overline{K^{*0}}(892)$ events [Boz 93].

[4]Since the mass cut used on the $pK^-\pi^+$ sample which produced the $\overline{K^{*0}}(892)$ peak was 2286.5 MeV $\pm$ (one standard deviation), the $pK^-\pi^+$ yield is also scaled by 68%.

CHAPTER 6

Conclusion

This final chapter reviews the highlights of the E-687 experiment and summarizes the measurements performed in this dissertation. The results are compared to other measurements of the relative branching ratios $B(\Lambda_c^+ \to \Lambda^0\pi^+\pi^-\pi^+)/B(\Lambda_c^+ \to pK^-\pi^+)$ and $B(\Lambda_c^+ \to p\overline{K^{*0}}(892))/B(\Lambda_c^+ \to pK^-\pi^+)$; and to other measured masses of the Ξ_c^+ . The thesis concludes with some final thoughts on these measurements and their implications.

The E-687 experiment succeeded two fixed-target high-energy photoproduction precursors: E-691, and the 1998 run of E-687. Its success (as evidenced by the abundance of publications) owes to an extremely dedicated and talented group of experimenters, especially regarding the detector design, the high-quality vertex algorithms, and the various analyses. The second run of the experiment occurred intermittently from January 1990 to January 1992, and used a high-energy bremsstrahlung photon beam of average tagged momentum $\approx$ 200 GeV/c which impinged upon a beryllium target. The run accumulated $\approx 5 \times 10^8$ hadronic triggers and reconstructed $\approx 10^5$ charm decays.

6.1 Search for the $\Xi_c^+ \to \Lambda^0 K^-\pi^+\pi^+$ Decay

We do not claim as evidence for this state the material presented in Chapter

4. While it appears that a signal may be present in the data, its mass does not agree with the currently accepted mass of the Ξ_c^+ . The most likely possibility of a reflection due to misidentified $\Lambda_c^+ \to \Lambda^0\pi^+\pi^-\pi^+$ contamination seems to have been ruled out by both excluding false $\Lambda_c^+ \to \Lambda^0\pi^+\pi^-\pi^+$ entries and by examining the wrong-sign $\Lambda^0 K^+\pi^-\pi^-$ channel. Reflections involving misidentified K_s^0 also seem to have been ruled out. There is no way to predict how many $\Xi_c^+ \to \Lambda^0 K^-\pi^+\pi^+$ events might be observed with respect to $\Xi_c^+ \to \Xi^-\pi^+\pi^+$ events, for the respective quark diagrams only indicate that both decays are Cabibbo-favored and cannot provide any useful predictions. Therefore, we do not know if, given our statistics in the $\Xi_c^+ \to \Xi^-\pi^+\pi^+$ mode, the $\Xi_c^+ \to \Lambda^0 K^-\pi^+\pi^+$ mode should even be visible.

6.2 The $B(\Lambda_c^+ \to \Lambda^0\pi^+\pi^-\pi^+)/B(\Lambda_c^+ \to pK^-\pi^+)$ Branching Ratio Measurement

We report evidence for the Cabibbo-favored decay $\Lambda_c^+ \to \Lambda^0\pi^+\pi^-\pi^+$ and measure its decay rate relative to that of the $\Lambda_c^+ \to pK^-\pi^+$ mode:

$$\frac{B(\Lambda_c^+ \to \Lambda^0\pi^+\pi^-\pi^+)}{B(\Lambda_c^+ \to pK^-\pi^+)} = 1.16 \pm 0.27 \,{}^{+\,0.16}_{-\,0.18} \quad . \tag{6.1}$$

The measurement was based on 123 ± 20 $\Lambda_c^+ \to \Lambda^0\pi^+\pi^-\pi^+$ events and 522 ± 38 $\Lambda_c^+ \to pK^-\pi^+$ events. This result is not consistent with the world average of 0.66 ± 0.11 which involves only four previous measurements and which is dominated by the CLEO value, but it is consistent with the fixed target measurements from E-691 and NA32 (see Figure 6.1).

While the $\Lambda_c^+ \to \Lambda^0\pi^+\pi^-\pi^+$ yield is less than that of CLEO, it should be noted that E-687 does observe yields of similar size which depend on the cuts involved (see

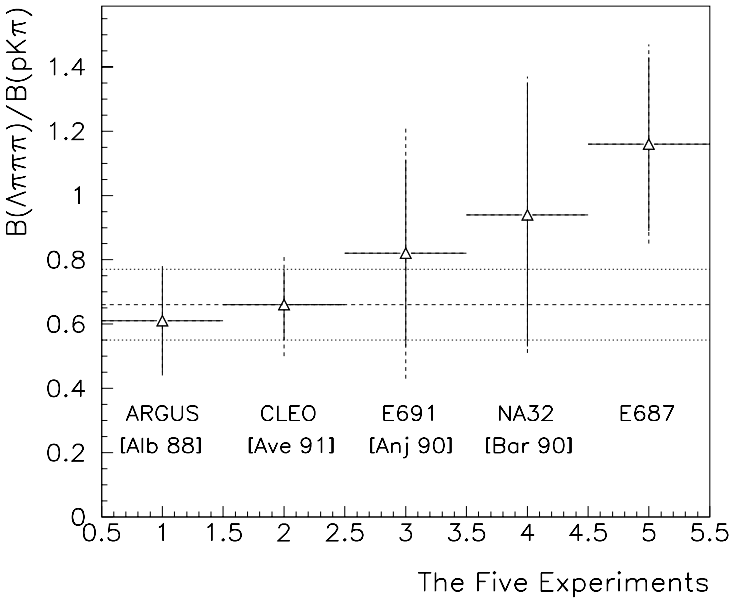

Figure 6.1. The $B(\Lambda_c^+ \to \Lambda^0\pi^+\pi^-\pi^+)/B(\Lambda_c^+ \to pK^-\pi^+)$ measurements from each of the five experiments. The horizontal dotted lines display the current world average with error bars.

Chapter 4). However, when performing this decay-rate measurement we impose cuts not on the basis of maximizing yields but on the basis of detailed systematic studies. The statistical significance of this measurement is comparable to that obtained by CLEO and will therefore affect the world average.

6.3 *Measurement of* $B(\Lambda_c^+ \to p\overline{K^{*0}}(892))/B(\Lambda_c^+ \to pK^-\pi^+)$

We report evidence of $\Lambda_c^+ \to p\overline{K^{*0}}(892)$, a decay which may involve a W-exchange mechanism, and we measure its decay rate relative to that of the $\Lambda_c^+ \to pK^-\pi^+$ mode:

$$\frac{B(\Lambda_c^+ \to p\overline{K^{*0}}(892))}{B(\Lambda_c^+ \to pK^-\pi^+)} = 0.39 \pm 0.07 \pm 0.07 \quad . \tag{6.2}$$

The measurement was based on 76 ± 12 $K^-\pi^+$ events and 436 ± 31 $pK^-\pi^+$ events, and has been corrected for the unseen $\overline{K^{*0}}(892) \to \overline{K^0}\pi^0$ decay mode. The value of the measurement agrees well with the current world average of $0.36\ ^{+0.06}_{-0.07}$ [PDG 94]. We find virtually no evidence for other possible W-exchange contributions to the $pK^-\pi^+$ final state from $\Lambda_c^+ \to \Delta^{++}(1232)K^-$ or $\Lambda_c^+ \to \Lambda^*(1520)\pi^+$.

BIBLIOGRAPHY

[Alb 88] H. Albrecht, *et al.*, "Observation of the charmed baryon Λ_c^+ in e^+e^- annihilation at 10.55 GeV" (ARGUS), *Phys. Lett.* **B 207** 109 (1988).

[Anj 90] J. Anjos, *et al.*, "Study of the decays of the Λ_c^+ " (E-691), *Phys. Rev.* **D 41** 801 (1990).

[Ave 91] P. Avery, *et al.*, "Inclusive Production of the charmed baryon Λ_c^+ from e^+e^- annihilations at $\sqrt{s}$=10.55 GeV" (CLEO), *Phys. Rev.* **D 43** 3599 (1991).

[Bar 90] S. Barlag, *et al.*, "Measurement of Various Decay Modes of Charmed Particles D^0, D^+, D_s^+ and Λ_c^+ " (NA32), *Zeitschrift für Physik* **C 48** 29 (1990).

[Bel 86] G. Bellini *et al.*, "The Microstrip Vertex Detector for the E-687 Experiment at the Tevatron", Nucl. Instr. and Meth. in Phys. Res. A252, (1986) 366.

[Bel 92] G. Bellini *et al.*, "A Silicon Active Target for Charm Particle Identification", Nucl. Instr. and Meth. in Phys. Res. A320, (1992) 439.

[Bia 83] S.F. Biagi, *et al.*, "Observation of a Narrow State at 2.46 GeV/c^2 - A Candidate for the Charmed Strange Baryon A^+", *Phys. Lett.* **122B**, 455 (1983).

[Big 95] I. Bigi, personal communication.

[Boz 93] A. Bozek, *et al.*, "A study of Λ_c^+ decays into $pK^-\pi^+$, $pK^-\pi^+\pi^0$, and $pK^-\pi^+\pi^0\pi^0$ ", *Phys. Lett.* **312B**, 247 (1993).

[Cab 64] N. Cabibbo, *Phys. Rev. Lett.* **10**, 531 (1963).

[Cot 87] P. Coteus, *et al.*, "Production of the Charmed Strange Baryon Ξ_c^+ by Neutrons", *Phys. Rev. Lett.* **59**, 1530 (1987).

[Cul 91] R.L. Culbertson,"Vertexing in the 90's", E-687 internal memo (June 1991).

[Cul 94] R.L. Culbertson, "*Post hoc* No More? ROGUE MCS and PWC Noise Improvements", E-687 Internal Memo (March 1994).

[Dal 92] C. Dallapiccola, "Ξ^-/Ω^- Skim", E-687 Internal Memo (June 1992).

[Fra 92] P.L. Frabetti *et al.*, "Description and Performance of the Fermilab E-687 Spectrometer", Nucl. Instr. and Meth. in Phys. Res. A320 (1992) 519-547.

[Fra 93a] P.L. Frabetti *et al.*, "Measurement of the Mass and Lifetime of the Ξ_c^+ ", *Phys. Rev. Lett.* **70**, 1381 (1993).

[Fra 93b] P.L. Frabetti *et al.*, "A Wide Band Photon Beam at the Fermilab Tevatron to study Heavy Flavours", Nucl. Instr. and Meth. in Phys. Res. A329 (1993) 62.

[Fra 93c] P.L. Frabetti *et al.*, "A Measurement of the Λ_c^+ Lifetime", *Phys. Rev. Lett.* **70**, 1755 (1993).

[Gar 92] R. Gardner,"E-687 Lund Implentation in Rogue", E-687 Internal Memo (February 1992).

[Gel 64] M. Gell-Mann, *Phys. Lett.* **8**, 214 (1964).

[Gla 70] S. Glashow, J. Iliopoulos, and L. Maiani, *Phys. Rev.* **D2**, 1285 (1970).

[Gro 73] D. Gross and F. Wilczek, *Phys. Rev. Lett.* **30**, 1343 (1973).

[Inz 86] P. Inzani *et al.*, "A Fast ADC System for Silicon Microstrip Readout", IEEE Transactions on Nuclear Science, Vol. NS-33, N.1, pg. 911 (Feb. 1986).

[Kas 88] P. Kasper, *et al.*, "Wide Band to Double Band", Upgrade, Fermilab, TM-1552.

[Kek 92] V. D. Kekelidze, "First Observation of Decay Asymmetry and some Decay Modes of Ξ_c^+ produced by Neutrons at Serpukhov Acclerator", *Proceedings of the XXVI International Conference on High Energy Physics* **1**, 1066 (1992).

[Kob 73] M. Kobayashi and T. Maskawa, *Prog. Theor. Phys.* **49**, 652 (1973).

[Lin 90] K. Lingel, Ph.D. Thesis, University of Illinois (1990).

[Mor 88] L. Moroni and D. Pedrini, "All you always wanted to know about Microrico but were afraid to ask", E-687 internal memo (Nov. 1988).

[Mou 92] R. Mountain, "Photon and Hadron Inteactions in the Scintillating Fiber Target" Ph.D. Thesis, University of Notre Dame (1992).

[Pet 90] D. Petravick, *et al.*, "The PAN-DA Data Acquisition System", Fermilab preprint, FERMILAB-Conf-89/136.

[PDG 94] Particle Data Group, Review of Particle Properties, *Phys. Rev.* **D 50**, Part 1 (1994).

[Ste 87] Sten Hansen, Fermilab Physics Department, drawing numbers 3687-EC-240543, 3687-EC-240544.

[Wil 89] J. Wilson, J. Wiss, "Generalized Vee Fitting", E-687 internal note (1989).

[Wis 88a] J. Wiss, "The Logic Cerenkov Algorithm", E-687 internal note (1988).

[Wis 88b] J. Wiss,"Analytic Calculations Related to Micro Linking", E-687 internal memo (August 1988).